

2004

Ultrasonic signal detection and recognition using dynamic wavelet fingerprints

Jidong Hou

College of William & Mary - Arts & Sciences

Follow this and additional works at: <https://scholarworks.wm.edu/etd>



Part of the [Materials Science and Engineering Commons](#)

Recommended Citation

Hou, Jidong, "Ultrasonic signal detection and recognition using dynamic wavelet fingerprints" (2004). *Dissertations, Theses, and Masters Projects*. Paper 1539623437.
<https://dx.doi.org/doi:10.21220/s2-qg0z-n088>

This Dissertation is brought to you for free and open access by the Theses, Dissertations, & Master Projects at W&M ScholarWorks. It has been accepted for inclusion in Dissertations, Theses, and Masters Projects by an authorized administrator of W&M ScholarWorks. For more information, please contact scholarworks@wm.edu.

**ULTRASONIC SIGNAL DETECTION AND RECOGNITION
USING DYNAMIC WAVELET FINGERPRINTS**

A Dissertation

Presented to

The Faculty of the Department of Applied Science

The College of William and Mary in Virginia

In Partial Fulfillment

Of the Requirements for the Degree of

Doctor of Philosophy

By

Jidong Hou

2004

APPROVAL SHEET

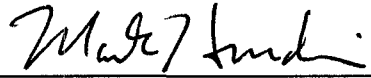
This dissertation is submitted in partial fulfillment of
the requirements for the degree of

Doctor of Philosophy

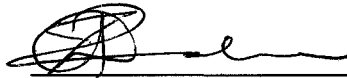


Jidong Hou

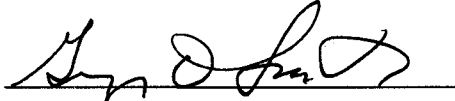
Approved by the Committee, April 2004



Dr. Mark K. Hinders, Chair
Associate Professor of Applied Science



Dr. Zia-ur Rahman
Research Associate Professor of Applied Science



Dr. Gregory D. Smith
Assistant Professor of Applied Science



Dr. Eugene R. Tracy
Chancellor Professor of Physics

**ULTRASONIC SIGNAL DETECTION AND RECOGNITION
USING DYNAMIC WAVELET FINGERPRINTS**

Copyright

by

Jidong Hou

2004

To my family.

TABLE OF CONTENTS

| | Page |
|--|------|
| Acknowledgements | vi |
| List of Tables | vii |
| List of Figures | viii |
| Abstract | xiv |
| Chapter I. Introduction | 2 |
| Chapter II. Fundamentals of Wavelets | 10 |
| Chapter III. The Dynamic Wavelet Fingerprint Technique | 28 |
| Chapter IV. Ultrasonic Periodontal Probing | 47 |
| Chapter V. Multi-Mode Lamb Wave Tomography | 72 |
| Chapter VI. Ultrasonic Inspection of Thin Multilayers | 106 |
| Chapter VII. Conclusions and Future Work | 132 |
| Appendix A. | 139 |
| Appendix B. | 144 |
| Appendix C. | 158 |
| Appendix D. | 161 |
| Bibliography | 170 |
| Vita | 179 |

ACKNOWLEDGEMENTS

I wish to express my deep appreciation to Professor Mark K Hinders, under whose guidance this investigation was conducted, for his guidance, encouragement and support.

I am also indebted to Dr. Rahman, Dr. Smith and Dr. Tracy for their careful reading and criticism of the manuscript.

I am very grateful to the valuable support of Dr. Jim McKeon, Dr. Dennis Krausman, Ms. Tricia Olson and other colleagues at SONIX, Inc.

I would like to thank Jonathan Stevens for his assistance on instrument development and Kevin Leonard for his support on data collection.

Many thanks to my parents, my wife and son for their endless love.

LIST OF TABLES

| Table | | Page |
|-------|--|------|
| 3.1 | Moment Invariants Of A Dynamic Wavelet Fingerprint | 35 |
| 3.2 | Moment Invariants Of Dynamic Wavelet Fingerprint Of Different Pulses | 39 |
| 3.3 | Materials Properties Of Samples | 40 |
| 4.1 | Bland-Altman Evaluation Of Ultrasonic Probing Results (May18) | 70 |
| 4.2 | Bland-Altman Evaluation Of Ultrasonic Probing Results (August 18) | 71 |
| 5.1 | Multi-Modes Traveltime Measurement Based On The DWFP Technique | 88 |
| 6.1 | DWFPs Corresponding To The Two Simulated Echoes | 115 |
| 6.3 | Detection Ratio Of Five Random Spaced Echoes Representing Different SNR Levels | 122 |

LIST OF FIGURES

| Figure | | Page |
|--------|---|------|
| 1.1 | Typical fingerprints. Left to right, top to bottom: plain arch, loop, pocket loop and double loop (whorl). | 2 |
| 1.2 | Ultrasonic inspection modes. (a) Pulse-Echo mode. Each interface or discontinuity results in a corresponding echo in the received waveform. (b) Through-Transmission mode. The received waveform is the transmitted ultrasonic pulse. | 6 |
| 1.3 | Pulse echo/through transmission setup (Courtesy of Sonix, Inc.) | 6 |
| 1.4 | Gating of ultrasonic signal. The red and green data gates are placed at different locations to detect reflections of interest. (Courtesy of Sonix, Inc.) | 7 |
| 2.1 | (a) Two sinusoids corrupted by two perturbations, and (b) the power spectrum. | 11 |
| 2.2 | Time-frequency resolution of the Short-Time Fourier Transform (STFT) and the Wavelet Transform (WT). (a) For the STFT and (b) For the WT. Note the uniform cells (single resolution) for STFT become variable (multi-resolution) for WT, where wide time intervals are used for low frequency and short time intervals are used for high frequency. | 15 |
| 2.3 | Spectrogram of signal shown in Figure 2.2 with different window width. (a) window width = 256. (b) window width = 2. | 16 |
| 2.4 | Continuous wavelet transform of the signal described by (2.2). The two sharp bursts were detected at small scales, and the two sinusoids components were resolved at corresponding scales. | 19 |
| 2.5 | The dyadic sampling grid in the time scale plane. | 21 |
| 2.6 | Discrete wavelet transform using subband coding scheme. (a) Subband coding scheme. The original signal $x(n)$ pass through two complementary filters $h(k)$ and $g(k)$ followed by down-sampling and emerges as two sequences cA and cD . To reconstruct the original | 25 |

signal, the two sequences cA and cD go through up-sampling and filtering followed by summation. (b) Filter bank tree of the discrete wavelet transform. The DWT coefficients are produced with filtering followed by down-sampling.

| | | |
|-----|---|----|
| 3.1 | Wavelet fingerprints generation. (a) Ultrasound pulse; (b) 3-D view of the wavelet coefficients and its contour; (c) slice projection; (d) the dynamic wavelet fingerprint (b). | 33 |
| 3.2 | Five pulses with different central frequencies and their dynamic wavelet fingerprints: (a) the pulses; (b) the daubechies wavelet of order 1; (c) the daubechies wavelet of order 10; (d) the morlet wavelet; (e) the mexican hat wavelet. | 36 |
| 3.3 | Three pulses of 2.25 MHz center frequency with different durations and their dynamic wavelet fingerprints: (a) the pulses; (b) the daubechies wavelet of order 1; (c) the daubechies wavelet of order 10; (d) the morlet wavelet; (e) the mexican hat wavelet. | 37 |
| 3.4 | System setup for materials sorting. | 41 |
| 3.5 | Echoes from different material surface and their dynamic wavelet fingerprints. (a) echoes; (b) daubechies wavelet of order 1; (c) mexican hat wavelet; (d) the sixth derivative of gaussian wavelet. | 42 |
| 3.6 | Artificial neural network used to sort materials. | 43 |
| 3.7 | Artificial neural network training: performance as a function of training epochs (goal = 1×10^{-4}). | 44 |
| 4.1 | Traditional manual periodontal probing. (a) Gingivitis. (b) Severe Periodontitis. | 48 |
| 4.2 | The ultrasonic periodontal probing system. (a) overview of the system; (b) the ultrasonic probe handpiece. | 53 |
| 4.3 | Schematic of ultrasonic periodontal probing. | 54 |
| 4.4 | Illustration of signal processing for ultrasonic periodontal probing. (a) Original A-scan signal, (b) SAP peaks marked by the small circles, (c) The inclination index curve. The third significant peak (at about $8 \mu\text{sec}$) corresponds to the estimated location of the bottom of the periodontal pocket. | 55 |
| 4.5 | Flowchart of the algorithm used to process ultrasound signal to detect the bottom of the periodontal pocket. | 56 |

| | | |
|------|--|----|
| 4.6 | Typical DWFP sequence of an A-scan signal (time sequence: from left to right, from top to bottom). | 59 |
| 4.7 | Two-dimensional FFT images of three typical DWFP patterns. (a) Right inclined DWFP and its two-dimensional FFT image (b) Up-right DWFP and its two-dimensional FFT image (c) Left inclined DWFP and its two-dimensional FFT image (d) Two regions (shaded quadrants and un-shaded quadrants) used to calculate the inclination index of the two-dimensional FFT image. | 60 |
| 4.8 | Phantom probing using the ultrasonic probe. | 62 |
| 4.9 | Phantom probing signal and corresponding processing results. (a) Original A-scan signal, (b) SAP peaks (c) the inclination index curve. The third broad peak corresponds to the reflection from the bottom of the hole. | 63 |
| 4.10 | Ratio of agreement of ultrasonic probing vs. manual probing. (a) May 18, 2001 (b) August 17, 2001. Note that results for patient #1 in (a) and patient #14 in (b) are unavailable due to personal absence in corresponding clinical visit. | 65 |
| 4.11 | Difference against mean for periodontal probing depth of Patient #2, May 18. | 66 |
| 5.1 | Lamb waves traveling in the Y direction in a traction free isotropic plate of thickness $2d$. | 74 |
| 5.2 | Phase velocity dispersion curves in Aluminum plates for the first three symmetric and antisymmetric modes. Phase velocity is plotted versus the product of frequency f (MHz) and plate thickness $2d$ (mm). | 76 |
| 5.3 | Group velocity dispersion curves in Aluminum plates for the first two symmetric and antisymmetric modes. Group velocity is plotted versus the product of frequency f (MHz) and plate thickness $2d$ (mm). | 78 |
| 5.4 | Double crosshole scanning system. | 79 |
| 5.5 | Explanation of the ART algorithm for the double crosshole geometry. a -distance between transducers; pixels (m, n) are indexed as shown; ray enumeration order (i, j) is different from different projections. | 81 |
| 5.6 | Demonstration of the arrival sequence of three Lamb wave modes. (a) Two arbitrary rays. (b) The arrival sequence of the three modes remains unchanged, although there may be interferences indicated by the black | 87 |

arrow in between.

- 5.7 Illustration of the DWFP based algorithm to measure the arrival times of the multiple Lamb wave modes. (a) Original waveform. (b) Scale-averaged wavelet power (SAP). (c) Envelope of the SAP. Detected peaks are indicated by small circles. (d) DWFP patterns at the first five peak locations. The number on top of each pattern is the area of the white region in the pattern. Note the second pattern has significant smaller white area. 89
- 5.8 Experimentally estimated arrival times of the first three modes in a defect-free aluminum plate. (a) A1 mode. (b) A0 mode. (c) S2 mode. 93
- 5.9 Theoretical arrival times of the first three modes in a defect-free aluminum plate. (a) A1 mode. $v = 3500 \text{ m/s}$. (b) A0 mode. $v = 3100 \text{ m/s}$. (c) S0 mode. $v = 2000 \text{ m/s}$. 94
- 5.10 Experimentally estimated arrival times of the first three modes in an aluminum plate with a 2.2 –inch flat bottom hole in the center. (a) A1 mode. (b) A0 mode. (c) S0 mode. 96
- 5.11 Experimentally estimated arrival times of the first three modes in an aluminum plate with a 2-inch dished out flat bottom circle with max 60% thickness loss. (a) A1 mode. (b) A0 mode. (c) S0 mode. 97
- 5.12 Experimentally estimated arrival times of the first three modes in an aluminum plate with a 1”x2” rectangular thinned region with rounded corners. (a) A1 mode. (b) A0 mode. (c) S0 mode. 98
- 5.13 Plate #15 – SIRT reconstruction of defect free aluminum plate. Image size: 200 x 200 mm. (a) A1 mode. (b) A0 mode. (c) S0 mode. (d) Cartoon of the plate. 100
- 5.14 Plate #1 - SIRT reconstruction of a flat bottom hole 2.2-inch diameter, 50% thickness loss. Image size: 200 x 200 mm. (a) A1 mode. (b) A0 mode. (c) S0 mode. (d) Cartoon of the plate. 101
- 5.15 Plate #5 - SIRT reconstruction a 2-inch dished out flat bottom circle with max 60% thickness loss. Image size: 200 x 200 mm. (a) A1 mode. (b) A0 mode. (c) S0 mode. (d) Cartoon of the plate. 102
- 5.16 Plate #6- SIRT reconstruction a rectangular thinned region 1”x2” with rounded corners. Image size: 200 x 200 mm. (a) A1 mode. (b) A0 mode. (c) S0 mode. (d) Cartoon of the plate. 103

| | | |
|------|--|-----|
| 6.1 | Typical stacked chip scale packages. Multiple dies are stacked in one package. | 106 |
| 6.2 | Two echoes corrupted by uniform noise. The first echo is at 177 ns , the second echo is at 297 ns , $\tau = 120\text{ ns}$, SNR = 0 dB. | 113 |
| 6.3 | The DWFP sequence of the signal in Figure 6.2. The number on the top of each DWFP is the time where the DWFP is generated. Note the two patterns at 177 ns and 297 ns , each has a well developed circle inside. The wavelet used: Mexican hat. Scale range: 8:32. | 114 |
| 6.4 | Flowchart of the DWFP-based echo detection algorithm. | 116 |
| 6.5 | (a) Simulated five-echo signal with periodic spacing of 80 ns . (b) The circularity curve. The circles on the x-axis indicate the actual locations of the echoes. Note that each echo has a significant peak associated with it, even for the weakest one (SNR = 0 dB). | 119 |
| 6.6 | (a) Simulated five-echo signal with random spacing. (b) The circularity curve. The circles on the x-axis indicate the actual locations of the echoes. Note that each echo has a significant peak associated with it, even for the weakest one (SNR = 0 dB). | 120 |
| 6.7 | Detection ratios of equally spaced echoes. For each spacing case, there are five echoes representing different SNR levels to be detected. The precision of the detection is $\pm 5\text{ ns}$. | 122 |
| 6.8 | Cross-section schematic of a plastic encapsulated IC package. | 124 |
| 6.9 | UHR-2001 [®] Scanning Acoustic Microscope. (Courtesy of Sonix, Inc.) | 125 |
| 6.10 | Ultrasonic image giving a top view of the internal structure of a plastic encapsulated IC package. The blue box indicates the region where the ultrasonic waveforms were collected. | 126 |
| 6.11 | (a) A ultrasonic waveform collected on the plastic encapsulated IC package. (b) The circularity curve of the same waveform. The significant peaks indicate the locations of suspect interfaces. | 127 |
| 6.12 | The DWFP sequence of the waveform in Figure 6.11(a). Note some patterns have well developed circle inside. The wavelet used: Mexican hat. Scale range: 6:20. | 128 |
| 6.13 | (a) The B-Mode image generated with the proposed echo detection algorithm. Suspect interface can be seen as white lines in the image. (b) The standard B-Scan image generated with a commercial scanning | 130 |

acoustic microscope.

ABSTRACT

A novel ultrasonic signal detection and characterization technique is presented in this dissertation. The basic tool is a simplified time-frequency (scale) projection which is called a dynamic wavelet fingerprint. Taking advantage of the matched filter and adaptive time-frequency analysis properties of the wavelet transform, the dynamic wavelet fingerprint technique is a coupled approach of detection and recognition. Different from traditional value-based approaches, the dynamic wavelet fingerprint based technique is pattern or knowledge based. It is intuitive and self-explanatory, which enables the direct observation of the variation of non-stationary ultrasonic signals, even in complex environments. Due to this transparent property, efficient detection and characterization algorithms can be customized to address specific problems. Furthermore, artificial intelligence or expert systems can be built on it.

Several practical ultrasonic applications were used to evaluate the feasibility and performance of this new idea. The echoes from the surface of five different plates were characterized by the dynamic wavelet fingerprint. After learning, 100% correct identification ratio was achieved.

The second application was ultrasonic periodontal probing. The dynamic wavelet fingerprint technique was used to expose the hidden trend of the complex waveforms. Based on the experiment results of a simplified phantom, the regular variation of the inclination of the dynamic wavelet fingerprints was related to reflection regions of interest. The depth of the periodontal pocket was then estimated by finding the third significant peak in the inclination curves. Taking the manual probing data as "gold standard", a 40 % agreement ratio was achieved with a tolerance limit of ± 1 mm. However, statistically, lack of agreement was found in terms of the "limits of agreement" of Bland and Altman.

The third application was multi-mode Lamb wave tomography. The dynamic wavelet fingerprint technique was used to detect and characterize each suspect through-transmitted mode. The area of the dynamic wavelet fingerprint was then used as the feature to identify false modes caused by noise and other interference. The overall quality of the estimated arrival times was acceptable in terms of smooth distributions and variation pattern corresponding to specific defects. The tomographic images generated with the estimated arrival times were also fine enough to indicate different defects in aluminum plates.

The last application was ultrasonic thin multi-layers inspection. The dynamic wavelet fingerprint was generated at each sample point to achieve maximum time resolution. Based on observation of the simulated signals, a distinctive dynamic wavelet fingerprint was found to differentiate actual echoes from noise. High precision and robustness was demonstrated by processing simulated ultrasonic signals. When applied to practical data obtained from a plastic encapsulated IC package, multiple interfaces in the package were successfully detected.

**ULTRASONIC SIGNAL DETECTION AND RECOGNITION
USING DYNAMIC WAVELET FINGERPRINTS**

CHAPTER I

INTRODUCTION

Since its establishment in 1924, the Identification Division of the FBI has accumulated more than 30 million sets of fingerprints from criminal arrests [1], with 40,000 sets of fingerprints arriving daily that are divided into three groups: 5,000 new prints to be archived; 15,000 repeat prints (recidivists) to be compared with archived records and 20,000 security clearances to check and return to other agencies. To make identification and classification decisions, trained experts are called upon to study the “minutiae” in the fingerprints, such as the ridge endings and bifurcations formed since a person is born.

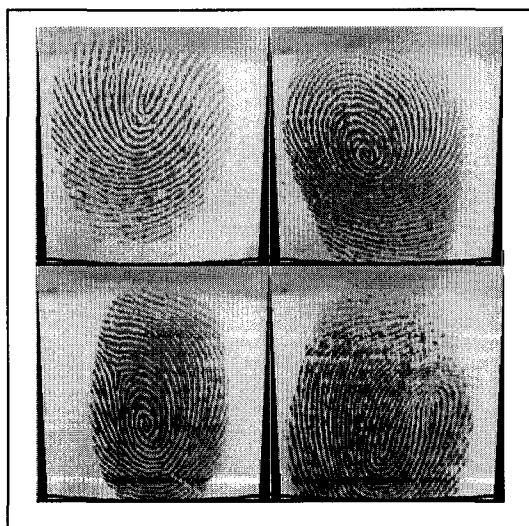


Figure 1.1 Typical fingerprints. Left to right, top to bottom: plain arch, loop, pocket loop and double loop (whorl).

These fingerprints used to be on cards in Washington and the document cabinets occupied a whole floor in the FBI building. To save the resources used for archiving and to improve transferring and processing efficiency, these fingerprints are now being digitized and compressed. Initially, the JPEG standard was considered to be the most promising candidate. However, at high compression ratios of 15:1 and 20:1, ridges that are separated in the true fingerprints were found to merge, which is unacceptable for identification purposes. It turned out that the wavelet/scalar quantization (WSQ) algorithm was superior [1]. The ten megabytes of data per card can be compressed by 15:1 without the information loss of the JPEG. Convinced by the quality of the compressed image, the FBI has now built the wavelet-based fingerprint archive system.

There are several interesting points in this story. The first point, fingerprints. The public takes it for granted today that identity can be positively established through fingerprints, but the accurate and widespread use of fingerprinting has only been around for about a century [2-4]. In 1901, the Henry System – which is the basis of all modern ten-finger identification systems – was devised by Sir Edward Richard Henry, then Inspector-General of Police in Bengal, India, and later Commissioner of London's Metropolitan Police. In 1902, the first fingerprinting system in the United States was installed by Dr. Henry P. DeForest for the New York Civil Service. In 1924, an Act of Congress established the Identification Division of the FBI. In 1946, the 100th million fingerprint card was received by the FBI. In 1967, the FBI initiated research and development on computerized scanning equipment for fingerprinting. In 1989, the Identification Division Automated System (IDAS) was implemented. Starting in January 2004, most foreign passengers who enter the United States are required to be

fingerprinted by the Homeland Security Department. When the Identification Division was established, few envisioned the high degree of efficiency and success of the fingerprint technique. The power of a fingerprint for identification comes from its uniqueness and consistency throughout a person's lifetime. Although a fingerprint is just a two-dimensional pattern, it contains such distinctive and concentrated information so that even twins can be differentiated successfully.

The second point, wavelets. With the name of "mathematical microscope"[5], wavelet analysis is a powerful tool to analyze local or transient variations. The origin of wavelet analysis can also be traced back to the beginning of the twentieth century. The Littlewood-Paley technique and Calderón-Zygmund theory in harmonic analysis and digital filter bank theory in signal processing can be considered as forerunners to wavelet analysis. In its present form, wavelet theory attracted attention in the 1980s through the work of several researchers from various disciplines – Strömberg, Morlet, Grossmann, Meyer, Battle, Lemarié, Coifman, Daubechies, Mallat, Chui – to name a few. Different types of wavelets have been used as tools to solve problems in signal analysis, image analysis, medical diagnostics, boundary value problems, geophysical signal processing, statistical analysis, pattern recognition, and many others.

The third point, processing of huge volumes of data. With the advances in science and the development of electronic and computer technology, huge volumes of fingerprint data are acquired and archived daily in digital format. To make effective use of this information, it is always necessary to develop efficient algorithms. Potential solutions may be inspired by biological systems, e.g., the human brain. Everyday, the brain

receives lots of information from sensors – eyes, ears, nose, skin and tongue – and it processes all of this information in real-time. It is thus reasonable to develop a system with artificial intelligence to process huge volumes of data.

Similar stories can be found (or written) for ultrasound applications. Both in medical diagnosis and non-destructive evaluation, the ultimate goal of ultrasonic inspection is to identify abnormalities – the “suspected criminals” – from numerous data. Generally there are two modes to perform ultrasonic testing. The first is the pulse-echo mode illustrated in Figure 1.2 (a). In this mode, a single transducer launches an ultrasonic pulse (transient signal) into the sample. Whenever the ultrasound pulse encounters a discontinuity or interface, part of the ultrasound energy is reflected back and picked up by the same transducer. The rest of the energy goes through the interface and continues to propagate in the medium. The second approach is through-transmission mode, which is illustrated in Figure 1.2 (b). In this mode, a second transducer is used to receive the transmitted ultrasound signal. A typical pulse echo/through transmission transducer setup is shown in Figure 1.3.

In both modes, the characteristics of the received waveforms provide information on the nature of the medium. Generally we would like to know *when* or *where* an event of suspect nature occurs, which leads to a detection problem. In addition, we would also like to know *what* event has occurred, which leads to a characterization or recognition problem.

The simplest detection method is gating (see Figure 1.4) where the peak amplitude of a segment of signal isolated by a pre-defined gate is compared with a

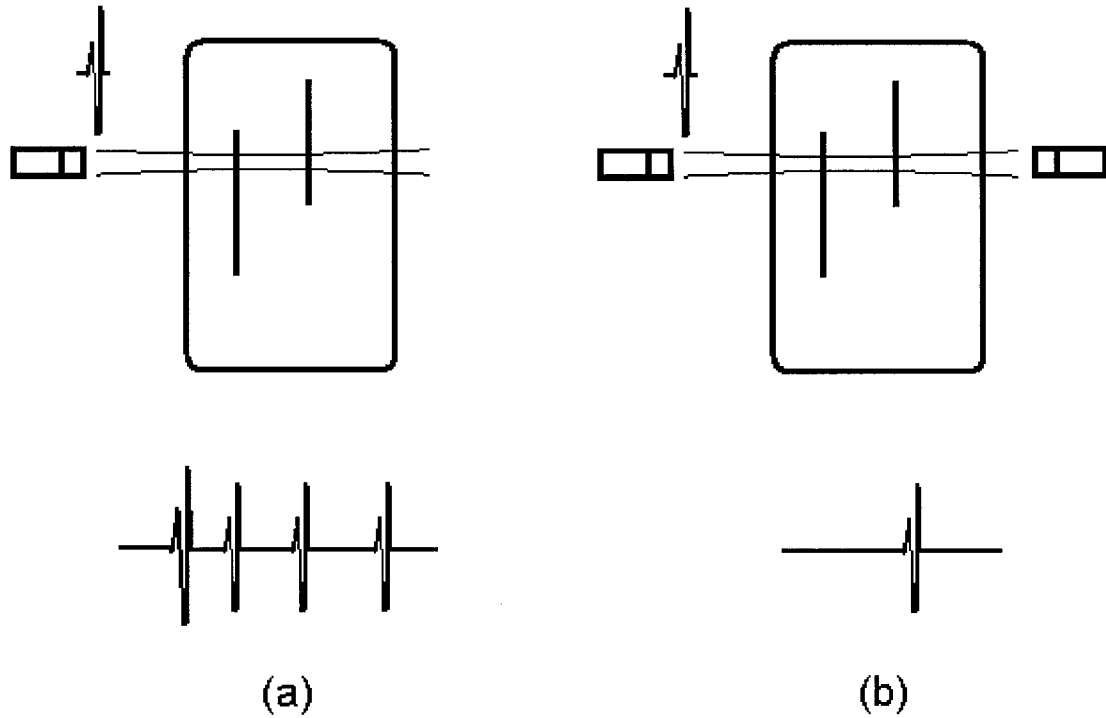


Figure 1.2 Ultrasonic inspection modes. (a) Pulse-Echo mode. Each interface or discontinuity results in a corresponding echo in the received waveform. (b) Through-Transmission mode. The received waveform is the transmitted ultrasonic pulse.

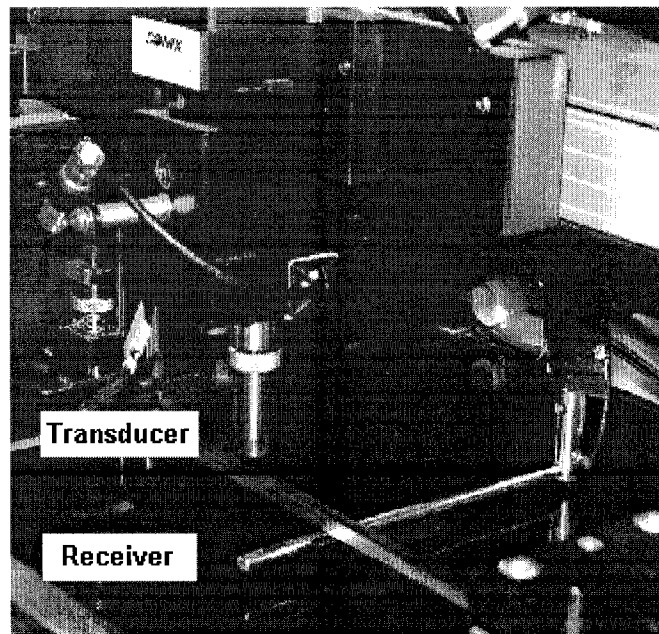


Figure 1.3 Pulse echo/through transmission setup (Courtesy of Sonix, Inc.)

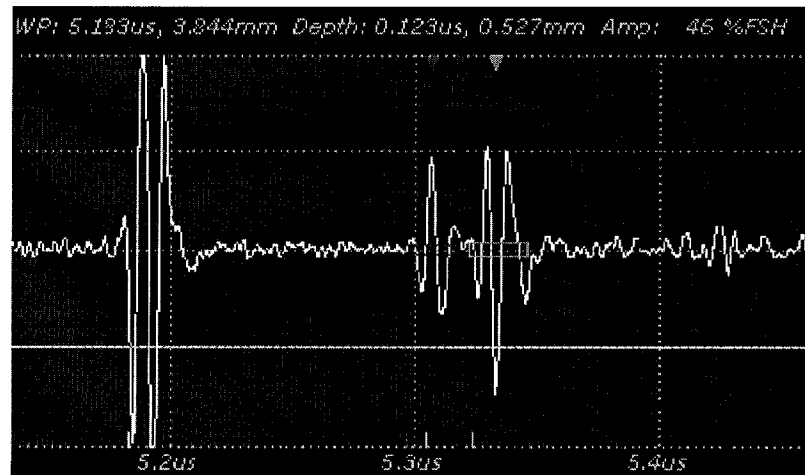


Figure 1.4 Gating of ultrasonic signal. The red and green data gates are placed at different locations to detect reflections of interest. (Courtesy of Sonix, Inc.)

predefined threshold. If the peak amplitude is larger than that threshold, the signal is considered to be significant enough to indicate a suspected discontinuity (defect).

Although simple and fast, due to the often arbitrary preset threshold and width setting of the gate, this technique is quite sensitive to noise and may not work for the most complex waveforms.

A more robust detection technique is the cross-correlation, which is defined [4] as

$$C_{xy}(\tau) = \lim_{T \rightarrow \infty} (1/T) \int_0^T x(t)y(t + \tau)dt$$

where $x(t)$ and $y(t)$ are arbitrary waveforms. In discrete form, we have [7]

$$C_{xy}(\tau) = \frac{1}{N} \sum_{k=1}^N x(t_k)y(t_k - \tau).$$

The cross-correlation coefficient reaches its maximum at particular values of τ where the signal $y(t)$ most similar to the known template signal is detected. The theory underlying the cross-correlation method is based on the assumption that the ultrasonic signals are stationary. But the non-stationary nature of these signals is often obvious and results from variations of the medium, nonlinear modulation, etc.[8] As will be discussed in detail in the next chapter, time-frequency analysis techniques are a more suitable tool to detect non-stationary transient signals.

Even when we can easily detect the transient signals, it is often of great interest to then characterize and distinguish between them. For example, in nondestructive evaluation of materials, we need to know if a reflection signal comes from a good bonding interface or from a delamination, or we need to know the size, shape and orientation of a discontinuity. In medical diagnostic ultrasound applications, it is the “Holy Grail” of reliable and automatic differentiation of normal and cancerous tissue [9].

A widely used characterization technique is spectral analysis. The traditional Fourier-based methods are ideally suited to analyze narrow band signals and generate features (spectral amplitudes) for detection and discrimination [10]. Again, for broadband transient signals it is necessary to apply more advanced time-frequency analysis techniques.

In summary, due to the complex physics of ultrasound propagation, the waveforms obtained are generally too complex to be analyzed by un-trained eyes. Instead, expert knowledge needs to be integrated into signal processing algorithms that are smart enough to deal with complex situations. Moreover, it is beyond a person’s

capability to deal with huge amount of waveforms collected daily. Thus, automatic processing systems are required.

This dissertation presents a *pattern-based* approach to build artificial intelligence into automatic signal processing algorithms. The idea is to use “fingerprints” to characterize and distinguish different ultrasonic transients. The tool to form these “fingerprints” is the wavelet transform. Unlike the FBI case where the wavelet transform is used to analyze and compress fingerprints, here the wavelet transform is used to generate a “dynamic wavelet fingerprint” which is then used to characterize and recognize ultrasonic signals.

This dissertation is organized as follows:

In Chapter II, the basic theory, algorithm and applications of wavelets are presented. In Chapter III, the dynamic wavelet fingerprint (DWFP) technique is introduced. A materials sorting application is used to demonstrate a working scenario where artificial intelligence based on the dynamic wavelet fingerprint is embedded into software. Chapter IV describes the development of a DWFP based algorithm to highlight the variation in ultrasonic periodontal probing signals and enable automatic measurement of periodontal pocket depth. Chapter V presents an application of the DWFP technique to extracting arrival times of multiple Lamb wave modes so that improved tomography images can be reconstructed. Chapter VI discusses the potential of the DWFP technique to automatically detect closely spaced transient signals, which is a critical problem for ultrasonic multi-layer structure inspection. The dissertation concludes with a summary of the work completed and recommendations for future work in Chapter VII.

CHAPTER II

FUNDAMENTALS OF WAVELETS

2.1 Time-frequency analysis

In many ultrasonic applications the signals of interest are non-stationary, i.e., the spectrum of the signal changes with time. On the other hand, the ultrasonic signal is usually a broadband pulse modulated at the center frequency of the transducer with limited time duration and frequency bandwidth. It has been proven that the time-frequency representation is a useful tool for simultaneous characterization of signals in time and frequency, in particular for detecting and charactering dispersive effects and flaw echoes in highly scattering materials. Since the transient signal is decomposed both in the time domain and frequency domain, the added complexity of describing the originally one-dimensional time signal as a two-dimensional representation results in a redundancy which can be advantageously utilized to improve interpretation of the experimental data [11]. This is similar to musical notation, for example, which tells the player which notes (= frequency information) to play at any given moment [5].

Given a signal $f(t)$, the standard Fourier transform,

$$\tilde{f}(\omega) = \frac{1}{\sqrt{2\pi}} \int_{-\infty}^{\infty} f(t)e^{-i\omega t} dt \quad (2.1)$$

becomes inadequate when one is interested in the local frequency content of a signal. In other words, the Fourier spectrum does not provide any time-domain information about the signal. To demonstrate this point, consider the signal

$$f(t) = \sin 2\pi\nu_1 t + \sin 2\pi\nu_2 t + \alpha[\delta(t - t_1) + \delta(t - t_2)] \quad (2.2)$$

which consists of two sinusoids of $\nu_1 = 200\text{Hz}$ and $\nu_2 = 400\text{Hz}$ and two delta functions occurring at $t_1 = 200\text{ms}$ and $t_2 = 205\text{ms}$, with $\alpha = 6$. The signal and its power spectrum are shown in Figure 2.1(a) and (b) respectively. It can be seen that Fourier

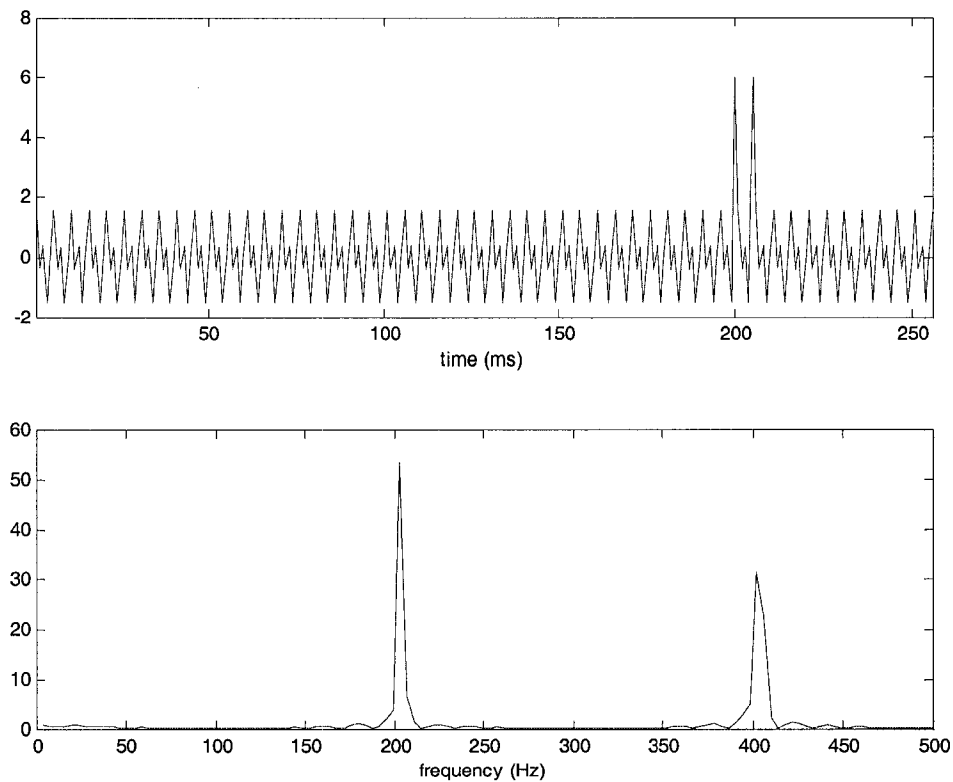


Figure 2.1 (a) Two sinusoids corrupted by two perturbations, and (b) the power spectrum.

transform successfully detected the two sinusoids components in terms of the sharp peaks near $\nu_1 = 200 \text{ Hz}$ and $\nu_2 = 400 \text{ Hz}$. As for the two abrupt pulses, however, there is no way to point out their locations [12]. The problem is due to the global property of Fourier transform, i.e., any abrupt change in time in a signal $f(t)$ is spread out over the whole frequency axis in its Fourier transform $\tilde{f}(\omega)$ [13]. In other words, in transforming to the frequency domain, time information is lost.

To overcome this drawback, a local analysis is needed to introduce time dependency into the Fourier analysis. This can be achieved by first windowing the signal $f(t)$ so as to cut out only a well-localized slice of $f(t)$, and then taking its Fourier transform [5]. This is the short-time Fourier transform (STFT). Formally, it is defined as

$$G_\phi f(b, \xi) = \int_{-\infty}^{\infty} f(t) \overline{\phi_{b, \xi}(t)} dt \quad (2.3)$$

where

$$\phi_{b, \xi}(t) = \phi(t - b) e^{j\xi t}. \quad (2.4)$$

and $\overline{\phi_{b, \xi}(t)}$ is the complex conjugate of $\phi_{b, \xi}(t)$. The window function $\phi(t)$ is allowed to be complex and satisfies the condition

$$\widehat{\phi}(0) = \int_{-\infty}^{\infty} \phi(t) dt \neq 0.$$

In other words, $\widehat{\phi}(\omega)$ behaves as a low-pass filter.

There are two important parameters for a windowing function: its center and width; the latter is usually twice the radius. For a general window function $\phi(t)$, its center t^* is defined as

$$t^* = \frac{1}{\|\phi\|^2} \int_{-\infty}^{\infty} t |\phi(t)|^2 dt \quad (2.5)$$

and the root-mean-square (RMS) radius Δ_ϕ is defined as

$$\Delta_\phi = \frac{1}{\|\phi\|} \left[\int_{-\infty}^{\infty} (t - t^*)^2 |\phi(t)|^2 dt \right]^{1/2} \quad (2.6)$$

The function $\phi(t)$ described above with finite Δ_ϕ is called a time window. Similarly, a frequency window $\hat{\phi}(\omega)$ with center ω^* and the RMS radius $\Delta_{\hat{\phi}}$ can be defined as

$$\omega^* = \frac{1}{\|\hat{\phi}\|^2} \int_{-\infty}^{\infty} \omega |\hat{\phi}(\omega)|^2 d\omega \quad (2.7)$$

$$\Delta_{\hat{\phi}} = \frac{1}{\|\hat{\phi}\|} \left[\int_{-\infty}^{\infty} (\omega - \omega^*)^2 |\hat{\phi}(\omega)|^2 d\omega \right]^{1/2} \quad (2.8)$$

As indicated by (2.3), the STFT maps the one-dimensional signal into a two dimensional function in the time-frequency plane (b, ξ) . For a given window function $\phi(t)$, the time and frequency resolution is controlled by the RMS radius Δ_ϕ and $\Delta_{\hat{\phi}}$ respectively, i.e., two pulses can be differentiated only if they are more than $2\Delta_\phi$ apart and two sinusoids will be discriminated only if they are more than $2\Delta_{\hat{\phi}}$ apart.

Unfortunately, it is impossible to achieve arbitrarily small resolution in time and frequency simultaneously, because the product $\Delta_\phi \Delta_{\hat{\phi}}$ is bounded by the uncertainty principle given by

$$\Delta_{\phi}\Delta_{\hat{\phi}} \geq \frac{1}{2} \quad (2.9)$$

where the equality holds only when $\phi(t)$ is of the Gaussian type.

More important is that once a window function has been chosen for the STFT, then the time-frequency resolution is fixed over the entire time-frequency plane (since the same window is applied at all frequencies). This is shown in Figure 2.2(a). This means that we need to decide on a suitable time window in advance and to trade time resolution for frequency resolution, or *vice versa* [13]. As shown in Figure 2.3(a), when a large window is used, the two sinusoids (Figure 2.1) are identified successfully. However, it is impossible to locate the two delta functions. In Figure 2.3(b) a small window is used, the two delta functions are resolved successfully with reduced resolution of the two sinusoids. It is obvious that such “rigid” solutions may lack efficiency. Instead, more flexible or adaptive solutions are more reasonable.

To overcome the resolution limitation of the STFT, one can imagine letting the resolution Δ_{ϕ} and $\Delta_{\hat{\phi}}$ vary in the time-frequency plane in order to obtain a multi-resolution analysis. In other words, we must have a window function whose Δ_{ϕ} increases while resolving the low frequency contents, and decreases while resolving the high frequency contents of a signal. This objective leads one to the development of wavelets analysis.

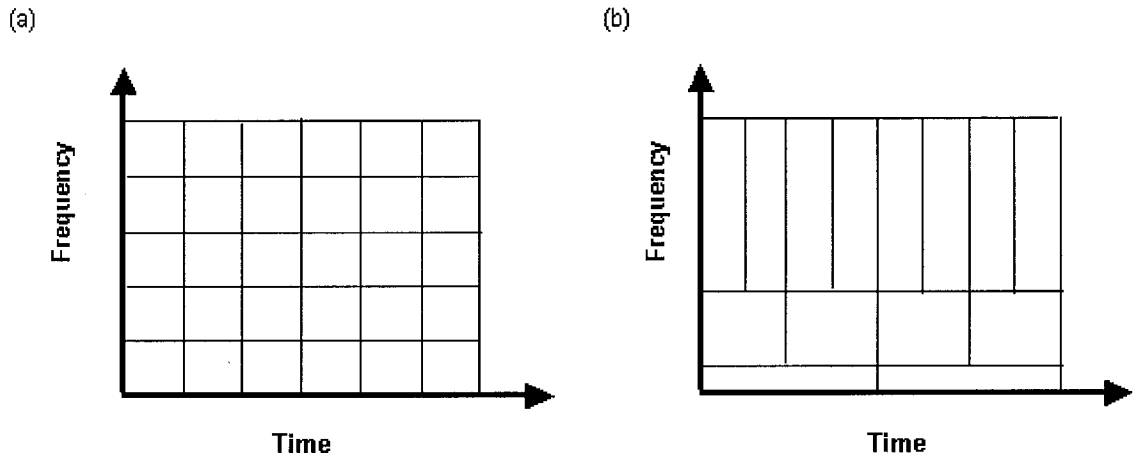


Figure 2.2 Time-frequency resolution of the Short-Time Fourier Transform (STFT) and the Wavelet Transform (WT). (a) For the STFT and (b) For the WT. Note the uniform cells (single resolution) for STFT become variable (multi-resolution) for WT, where wide time intervals are used for low frequency and short time intervals are used for high frequency.

2.2 The Continuous Wavelet Transform

For a square integrable function $f(t) \in L^2(\mathcal{R})$, i.e., $\int f^2(t) dt < \infty$, its continuous wavelet transform is defined as

$$W_{\psi} f(a, \tau) = \int_{-\infty}^{\infty} f(t) \overline{\psi_{a,\tau}(t)} dt \quad (2.10)$$

where $\psi_{a,\tau}(t)$ is the wavelet corresponding to continuous scale a and translation τ of the mother wavelet $\psi(t)$, i.e.,

$$\psi_{a,\tau}(t) = \frac{1}{\sqrt{a}} \psi\left(\frac{t-\tau}{a}\right), \quad a > 0. \quad (2.11)$$

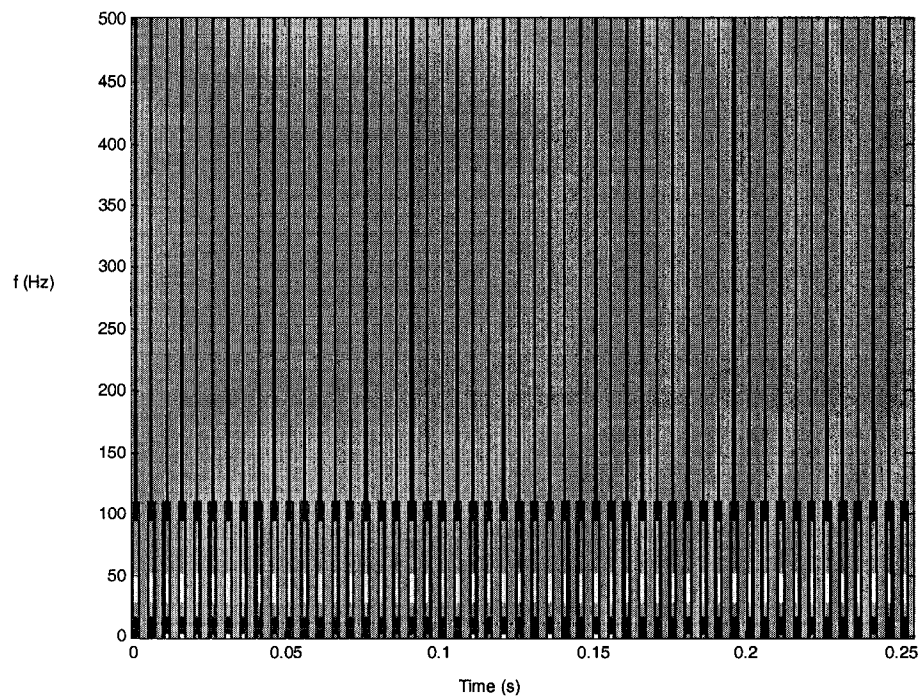
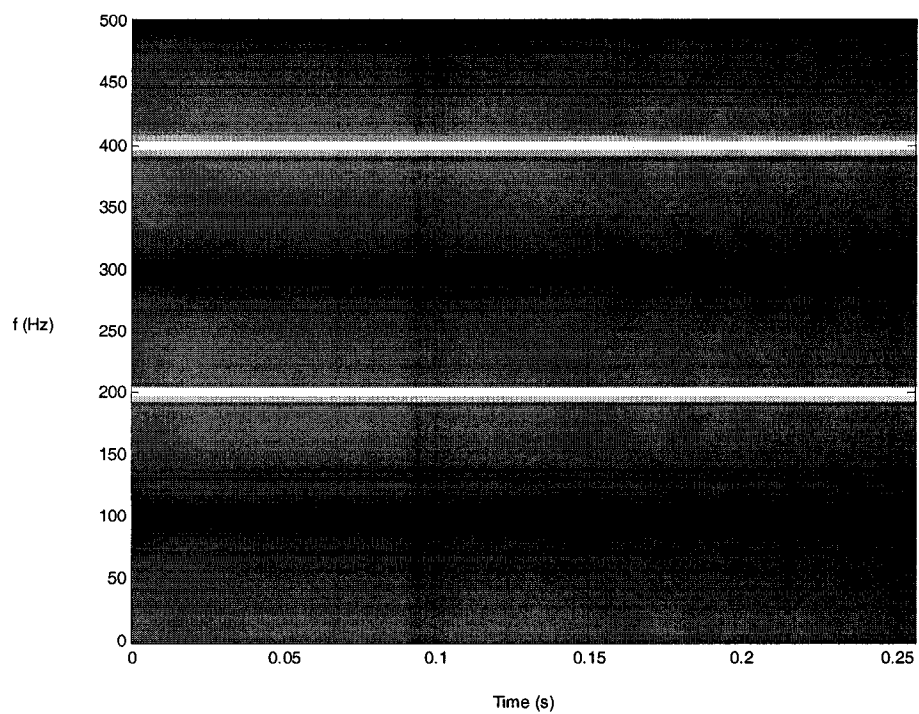


Figure 2.3 Spectrogram of signal shown in Figure 2.1 with different window width. (a) window width = 256. (b) window width = 2.

The normalization factor $a^{-1/2}$ is included so that $\|\psi_{a,\tau}\| = \|\psi\|$ [12].

In order to reconstruct the original function from its continuous wavelet transform, the mother wavelet has to satisfy the admissibility condition:

$$C_\psi = \int_{-\infty}^{\infty} \frac{|\hat{\psi}(\omega)|^2}{|\omega|} d\omega < \infty \quad (2.12)$$

This restricts the class of functions that can be wavelets. In particular, it implies that all wavelets must have

$$\hat{\psi}(0) = \int_{-\infty}^{\infty} \psi(t) dt = 0. \quad (2.13)$$

We conclude that all wavelets must oscillate, giving them the nature of small waves and hence the name *wavelets*.

On the time axis, the definition for the center t^* and the radius Δ_ψ remain the same as those for STFT. On the frequency axis, if only positive frequencies are considered, the center ω^* and the radius $\Delta_{\hat{\psi}}$ of the wavelet window $\psi(t)$ can be calculated as:

$$\omega^* = \frac{\int_0^{\infty} \omega |\hat{\psi}(\omega)|^2 d\omega}{\int_0^{\infty} |\hat{\psi}(\omega)|^2 d\omega} \quad (2.14)$$

$$\Delta_{\hat{\psi}} = \left[\frac{\int_0^{\infty} (\omega - \omega^*)^2 |\hat{\psi}(\omega)|^2 d\omega}{\int_0^{\infty} |\hat{\psi}(\omega)|^2 d\omega} \right]^{1/2} \quad (2.15)$$

Accordingly, the wavelet $\psi_{a,\tau}(t)$ has a time-frequency window given by:

$$\left[at^* + \tau - a\Delta_\psi, at^* + \tau + a\Delta_\psi \right] \times \left[\frac{1}{a}(\omega^* - \Delta_{\tilde{\psi}}), \frac{1}{a}(\omega^* + \Delta_{\tilde{\psi}}) \right]. \quad (2.16)$$

The uncertainty principle still holds for the wavelet transform in that the time frequency widow product = $2a\Delta_\psi \times \frac{2}{a}\Delta_{\tilde{\psi}} = 4\Delta_\psi\Delta_{\tilde{\psi}} = const$. However, instead of fixing at the same resolution, the shape of the resolution cell changes adaptively, i.e., for higher frequency, the time window is small (small scale), while for lower frequency, the time window becomes large (large scale). Such flexible and adaptive advantages are demonstrated in Figure 2.4 by analyzing the signal described in (2.2). It can be seen that good resolution in both the time and frequency axes are achieved simultaneously in only one computation. The two sharp bursts were detected at small scales (high frequency); and the two sinusoids components were resolved at corresponding scales, i.e., 200 Hz at $a \approx 1.2$ and 400 Hz at $a \approx 2.4$.

In general, we can connect scale to frequency by using the following relationship [14,15]:

$$F_a = \frac{\Delta \cdot F_c}{a} \quad (2.17)$$

where F_a is the pseudo-frequency in Hz corresponding to the scale a , F_c is the center frequency of a wavelet in Hz and Δ is the sampling rate. Accordingly, at 1000 Hz sampling rate, for the sixth derivative of Gaussian wavelet used in Figure 2.4, we have $F_{1.2} = 416.6$ Hz and $F_{2.4} = 208.3$ Hz.

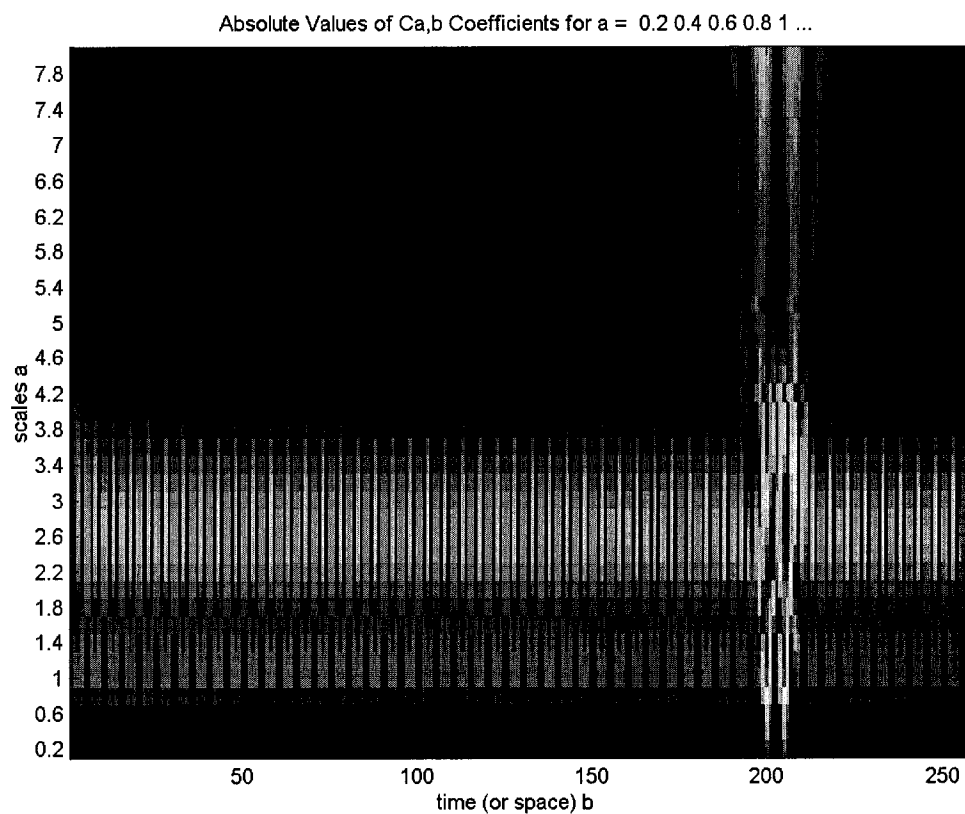


Figure 2.4 Continuous wavelet transform of the signal described by (2.2). The two sharp bursts were detected at small scales, and the two sinusoids components were resolved at corresponding scales.

2.3 The Discrete Wavelet Transform

The continuous wavelet transform is a natural tool for time-frequency signal analysis. However, since it is a redundant representation of the original one-dimensional signal, a direct evaluation of the integral in (2.10) can be a heavy computational load in problem solving. Also, there are practical situations such as data reduction and filtering that require a non-redundant wavelet transform. This is achieved by parameter discretization, i.e., instead of computing the wavelet transform for all continuous scale a and translation τ values, only a finite number of discrete values are used to perform the calculation. For example, we may choose $a = a_0^m$, $b = nb_0 a_0^m$, where m, n are integers, and $a_0 > 1, b_0 > 0$. Accordingly, the wavelets at those discrete nodes are:

$$\psi_{m,n}(t) = a_0^{-m/2} \psi\left(\frac{t - nb_0 a_0^m}{a_0^m}\right) = a_0^{-m/2} \psi(a_0^{-m} t - nb_0) \quad (2.18)$$

The feasibility condition for such discrete transforms was evaluated with the theory of frames [5]. Basically, in order to completely characterize a function $f(t)$ by the discrete wavelet coefficients $\langle f(t), \psi_{m,n}(t) \rangle$ (the inner product of the signal and the wavelet), the wavelets $\psi_{m,n}(t)$ should constitute a frame, i.e., there should exist $0 < A \leq B < \infty$ so that

$$A \|f(t)\|^2 \leq \sum_{m,n} |\langle f(t), \psi_{m,n}(t) \rangle|^2 \leq B \|f(t)\|^2. \quad (2.19)$$

The constants A, B are frames bounds and only depend on $\psi_{m,n}(t)$.

Obviously, the choice of the wavelet $\psi(t)$ and the corresponding parameters are not arbitrary. It is necessary to balance redundancy, i.e., sampling density, and restrictions on $\psi_{m,n}(t)$. If the redundancy is large (sampling is dense) then only mild restrictions are put on the wavelets. If the redundancy is small (sampling is sparse) then the wavelets are very constrained.

In fact, the distinction between various types of wavelet transforms depends on the way in which the scale and translation parameters are discretized [16]. At the most redundant end is the continuous wavelet transform; at the other extreme, a decomposition into wavelet bases only requires the values of the transform at the octave scales $a = 2^m$ and the dyadic translation $\tau = n2^m$ [17]. In this case, the number of coefficients needed for perfect reconstruction is the same as the number of data samples, which is known as critical sampling and minimizes redundant information [12]. Such a discretization procedure (shown in Figure 2.5) leads to the so-called Discrete Wavelet Transform.

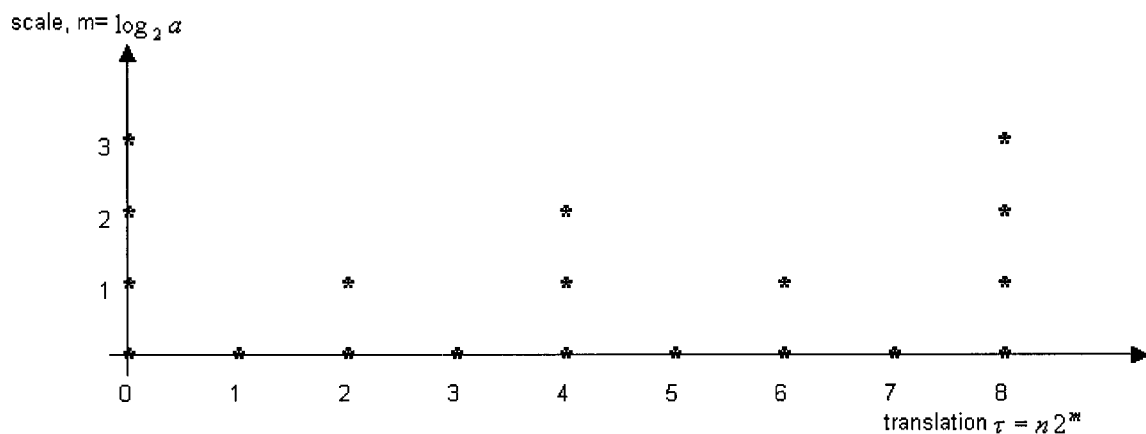


Figure 2.5 The dyadic sampling grid in the time scale plane.

2.4 Multi-Resolution Analysis And The Fast Algorithm

Discrete wavelet transforms can be implemented using extremely efficient algorithms, which are associated with Multi-Resolution Analysis (MRA) of the finite energy function space $L^2(\mathfrak{R})$.

Multi-Resolution Analysis plays a crucial role in the theory of the wavelet transform. It forms the most important building block for the construction of wavelets and the development of algorithms. The basic idea is to obtain a sequence of fine-to-coarse signal approximations by successive projection on subspaces, which are generated from the translation of a scaling function $\phi(t)$ at the corresponding resolution [16].

To achieve a multi-resolution analysis of a function, we must have a finite-energy function $\phi(t) \in L^2(\mathfrak{R})$, called a *scaling function*, that generates a nested space sequence $\{A_j\}$, namely [12]

$$\{0\} \leftarrow \cdots \subset A_{-1} \subset A_0 \subset A_1 \subset \cdots \rightarrow L^2. \quad (2.20)$$

For each scale level s , since the space A_s is a subspace of A_{s+1} , there is some space left in A_{s+1} , called W_s , which when combined with A_s gives us A_{s+1} . This space $\{W_s\}$ is called the *wavelet subspace* and is complementary to A_s in A_{s+1} , meaning that

$$A_s \cap W_s = \{0\} \quad (2.21)$$

$$A_s \oplus W_s = A_{s+1}. \quad (2.22)$$

Subspaces $\{ W_s \}$ are generated by $\psi(t) \in L^2(\mathfrak{R})$, called the *wavelet*, in the same way that $\{ A_s \}$ is generated by $\phi(t)$. In other words, any function $x_s(t) \in A_s$ can be represented as

$$x_s(t) = \sum_k a_{k,s} \phi(2^s t - k), \quad (2.23)$$

and any function $y_s(t) \in W_s$ can be represented as

$$y_s(t) = \sum_k w_{k,s} \psi(2^s t - k) \quad (2.24)$$

for some discrete coefficients $\{ a_{k,s} \}$ and $\{ w_{k,s} \}$.

The scaling function $\phi(t)$ and wavelet function $\psi(t)$ must satisfy following conditions [16]:

(i) Unconditional Riesz basis condition

$$0 < \alpha \leq \sum_{k \in \mathbb{Z}} |\widehat{\phi}(\omega + 2\pi k)|^2 \leq \beta < \infty \quad (2.25)$$

(ii) Partition of the unity

$$\sum_{k \in \mathbb{Z}} \phi(t - k) = 1 \quad (2.26)$$

or, the equivalent statement in the Fourier domain

$$\widehat{\phi}(0) = 1 \text{ and } \widehat{\phi}(2\pi k) = 0, \quad k \in \mathbb{Z}, k \neq 0 \quad (2.27)$$

(iii) Two scale relations

$$\phi(t) = \sum_{k \in \mathbb{Z}} g(k) \phi(2t - k) \quad (2.28)$$

$$\psi(t) = \sum_{k \in \mathbb{Z}} h(k) \phi(2t - k) \quad (2.29)$$

The two sequence $g(k)$ and $h(k)$ correspond to a low-pass filter and a high-pass (or band-pass) filter respectively. They show how the digital filters wholly determine the scaling function $\phi(t)$ and wavelet function $\psi(t)$ [17].

On the algorithm aspects, it has been shown the fast discrete wavelet transform illustrated in Figure 2.5 can be implemented with the two filters $g(k)$ and $h(k)$ using the subband coding scheme [13]. The procedure is shown in Figure 2.6. Basically, the continuous inner products can be evaluated numerically via simple discrete convolutions [16]. These filters cannot be arbitrary. Actually, the choice of these filters is directly related to the construction of different wavelets: Orthonormal, Semiorthogonal or Biorthogonal wavelets. For more detailed information about how to construct different wavelets, please refer to a number of excellent references [1,5,12,18].

2.5 Wavelet Applications

Although the wavelet concept was introduced within the background of time-frequency analysis, it actually has several different explanations that lead to different applications.

2.5.1 Detection and Estimation

One way to introduce the wavelet transform is to define wavelets as basis functions. In fact, the continuous wavelet transform can be considered as the inner

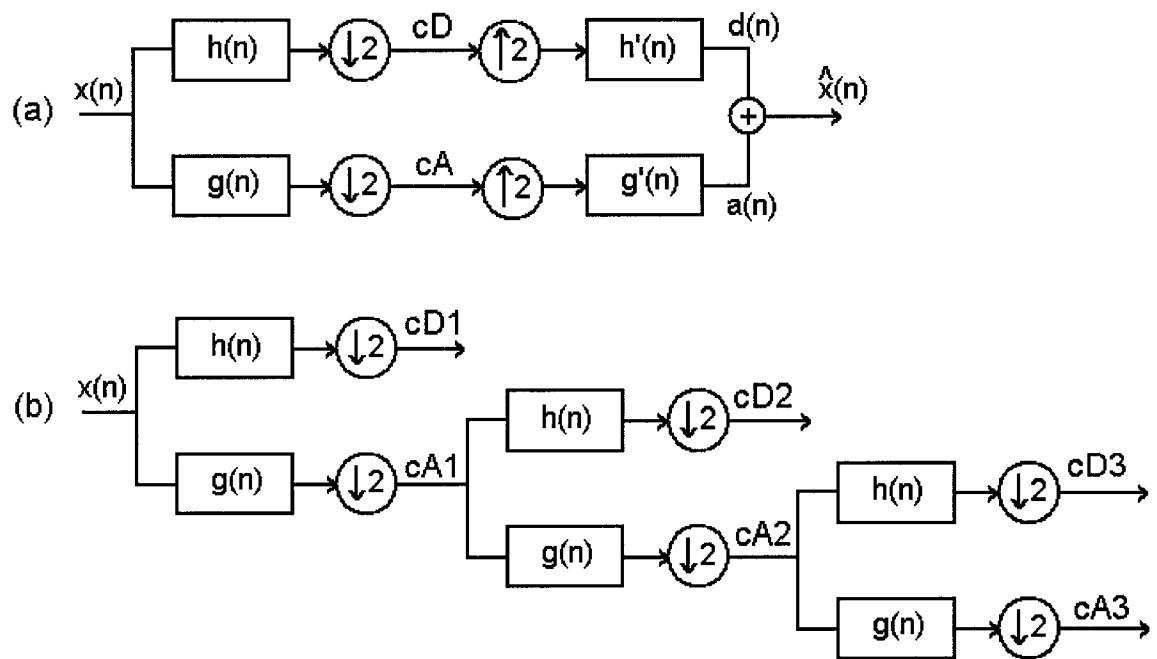


Figure 2.6 Discrete wavelet transform using subband coding scheme. (a) Subband coding scheme. The original signal $x(n)$ pass through two complementary filters $h(k)$ and $g(k)$ followed by down-sampling and emerges as two sequences cA and cD . To reconstruct the original signal, the two sequences cA and cD go through up-sampling and filtering followed by summation. (b) Filter bank tree of the discrete wavelet transform. The DWT coefficients are produced with filtering followed by down-sampling.

product of a function with corresponding wavelets. Since the inner product is often used as a similarity measurement, the continuous wavelet transform appears in several detection/estimation problems.

The estimation procedure consists in first emitting a known signal $h(t)$. In the presence of a target, this signal will be reflected back to the source (received signal $x(t)$) with a certain delay τ , due to the target's location, and a certain distortion (Doppler effect), due to the target's velocity. For wide-band signals, the Doppler frequency shift varies in the signal's spectrum, causing a stretching or a compression in the signal. The estimator thus becomes the "wide-band cross ambiguity function"[13,17,19,20]. The characteristics of the target will be determined by maximizing the ambiguity function. Since the "maximum likelihood" estimator now takes the form of a continuous wavelet transform, the basis function which best fits the signal is used to estimate the parameters.

Another view of the wavelet transform is to treat it as a bank of matched filters when the mother wavelet is chosen to be similar to the pulse to be detected. When the input signal is detected by one of the matched filters (wavelet), there is a correlation peak; its coordinates indicate the dilation factor and the time-delay of the signal [21].

2.5.2 De-noising

A commonly encountered difficulty in ultrasonic signal processing is the low signal to noise ratio. Due to its fast algorithm in the form of a filter bank, which is

illustrated in Figure 2.6, the discrete wavelet transform has been widely applied to suppressing noise and enhancing the signal to noise ratio [22,23].

The general de-noising procedure involves three steps:

1. Decompose: Choose a wavelet and a level N . Compute the wavelet coefficients c_D and c_A of the signal at level N .
2. Thresholding (Modification): for each level from 1 to N , select a threshold and apply thresholding to coefficients c_D .
3. Reconstruct: reconstruct filtered signal using the original coefficients c_A of level N and the modified coefficients c_D of levels from 1 to N .

2.5.3 Signal Characterization

Due to the time-frequency localization capability of the wavelet transform, the scalogram (defined as squared modulus of the continuous wavelet transform [13]) is an alternative to the spectrogram (defined as the square modulus of the STFT) for functions such as feature extraction, parameter estimation and pattern recognition of non-stationary signals [17, 24].

CHAPTER III

THE DYNAMIC WAVELET FINGERPRINT TECHNIQUE

3.1 Introduction

Automatic signal classification systems are used extensively for signal interpretation in non-destructive evaluation (NDE) applications. Their popularity stems from the fact that they are capable of rapid analysis of large amounts of data. In addition, they offer more accurate and consistent data interpretation as well as allowing storage of expert knowledge [25].

Most automatic signal classification systems are built upon a two-stage framework: preprocessing plus classification, for example. At the preprocessing stage, the critical point is to process the original signal in a way that some features can be generated and used to distinguish different signals. At the classification stage, an artificial neural network is often chosen to be the classifier to differentiate one class of signals from another.

Since the wavelet transform has excellent time-frequency localization properties, it is widely used as a preprocessing tool to extract features from transient signals. The most popular method involves the discrete or continuous wavelet transform of the signal of interest, with or without windowing, and then the application of a procedure such as

pruning [26,27], soft- or hard-thresholding [23,28] or dynamic programming [29] to determine the best subset of features.

Lunin and Barat [30,31] have presented an application of the magnetic field leakage technique for crack angle and depth estimation. In the preprocessing stage, six equivalent sections are extracted from the continuous wavelet transformation of the simulated magnetic field leakage signal and then five shape parameters of each section are used to construct feature vectors as inputs to a neural network. The limitation of their method is that it deals with simulated, isolated signals that have well defined boundaries. It is not suitable for a dynamic application where the transient signal is randomly distributed and the location and boundary of a transient signal needs to be identified on the spot.

In this chapter, an automatic ultrasound signal identification technique based on a dynamic wavelet fingerprint (DWFP) is proposed and developed. Dynamic wavelet fingerprints are constructed in three steps:

- (1) first, we use a pulse detection technique to locate the center of the transient signals of interest;
- (2) second, then a window with predefined width is used to isolate a transient signal from its neighborhood;
- (3) finally, a similar method to that of Lunin and Barat is used to generate a two-dimensional black and white wavelet image.

Feature vectors are constructed in terms of the moment invariants of the DWFP. These feature vectors are then used as inputs to an artificial neural network classifier.

We first introduce the dynamic wavelet fingerprint and describe its construction and the corresponding feature extraction method. We then use simulated ultrasound signals to explore the behavior and significance of the dynamic wavelet fingerprint. To evaluate the practical benefit and the feasibility of this technique, we next describe an ultrasonic classification system that sorts different materials via the echoes from their surface. A brief conclusion is given at the end.

3.2 The Dynamic Wavelet Fingerprint

Because fingerprints are useful for identifying people [4], it is natural to propose a signal “fingerprint” for classifying signals. The basic question is how to define and obtain such a fingerprint. For ultrasound applications, we are mostly concerned with the local or transient properties of the signals. Specifically, we need to locate the center of the transient signal first and then we need a properly defined window to isolate the transient signal from its neighborhood. Finally, we need to use an efficient method to extract significant information to distinguish one transient signal from another. With excellent time-frequency localization properties, the wavelet transform is a suitable tool for these requirements.

The first step is equivalent to pulse detection, which determines the presence of a transient signal and indicates its time location. From the matched filter point of view,

there is a correlation peak on the time-scale plane at the location of the transient signal, which indicates a concentration of energy [11].

In order to suppress noise in the signal, we applied a pruning procedure [11] based on the discrete stationary wavelet transform [32]:

$$W_p(a,b) = 0 \quad \text{for } a = 1, 2 \quad (3.1)$$

where $W_p(a,b)$ are the discrete stationary wavelet coefficients at scale a and time b .

By eliminating wavelet coefficients at low scale level, which corresponds to higher frequency components, the noise contribution to the signal is reduced. Then we calculated the scale-average wavelet power (SAP) proposed by Georgiou and Cohen [33] to obtain the centers of the transient signals:

$$\bar{W}^2(n) = \frac{1}{J} \sum_j |W(s_j, n)|^2, \quad (3.2)$$

where $W(s_j, n)$ are the continuous wavelet coefficients at scale s_j and position n .

In the presence of a coherent component (resolvable scatters), there is a concentration of power in the time locations of the coherent components. Specifically, we take the locations of the SAP peaks as the centers of the pulses:

$$n_c = \text{peak}(\bar{W}^2(n)). \quad (3.3)$$

Next, a suitable segment window is required to isolate the transient signal. This window should be small enough to be local to the center n_c , and large enough to

incorporate enough information of the transient signal. A natural choice is to use the duration of the initial input pulse as the width of this window. To this end, we use two times of the full width at half maximum power (FWHM in the equations) of the input transient signal

$$w = 2 \cdot FWHM \quad (3.4)$$

Thus the window for a specific pulse is $[n_c - FWHM, n_c + FWHM]$.

Figure 3.1(a) illustrates an ultrasound signal and the results of center location and window selection. A circle indicates the location of the center, which is obtained from Equation (3.3). The two squares indicate the end points of the window according to Equation (3.4). Figure 3.1(b) shows a three-dimensional view of the continuous wavelet coefficients of the ultrasound pulse in Figure 3.1(a), which was obtained when the Haar wavelet was used with a range of scale from 1 to 64 and a time window of 88 sample points wide.

To form a wavelet fingerprint, we first normalize the wavelet coefficients into the range of $[0, 1]$ and then apply the slice projection operation, which is shown in Figure 3.1(c), to project four equal-distance slices of the three dimensional continuous wavelet coefficients onto the time-scale plane, which results in a two-dimensional binary (0 and 1) image. Figure 3.1(d) shows the dynamic wavelet fingerprint obtained this way for the pulse in Figure 3.1(a).

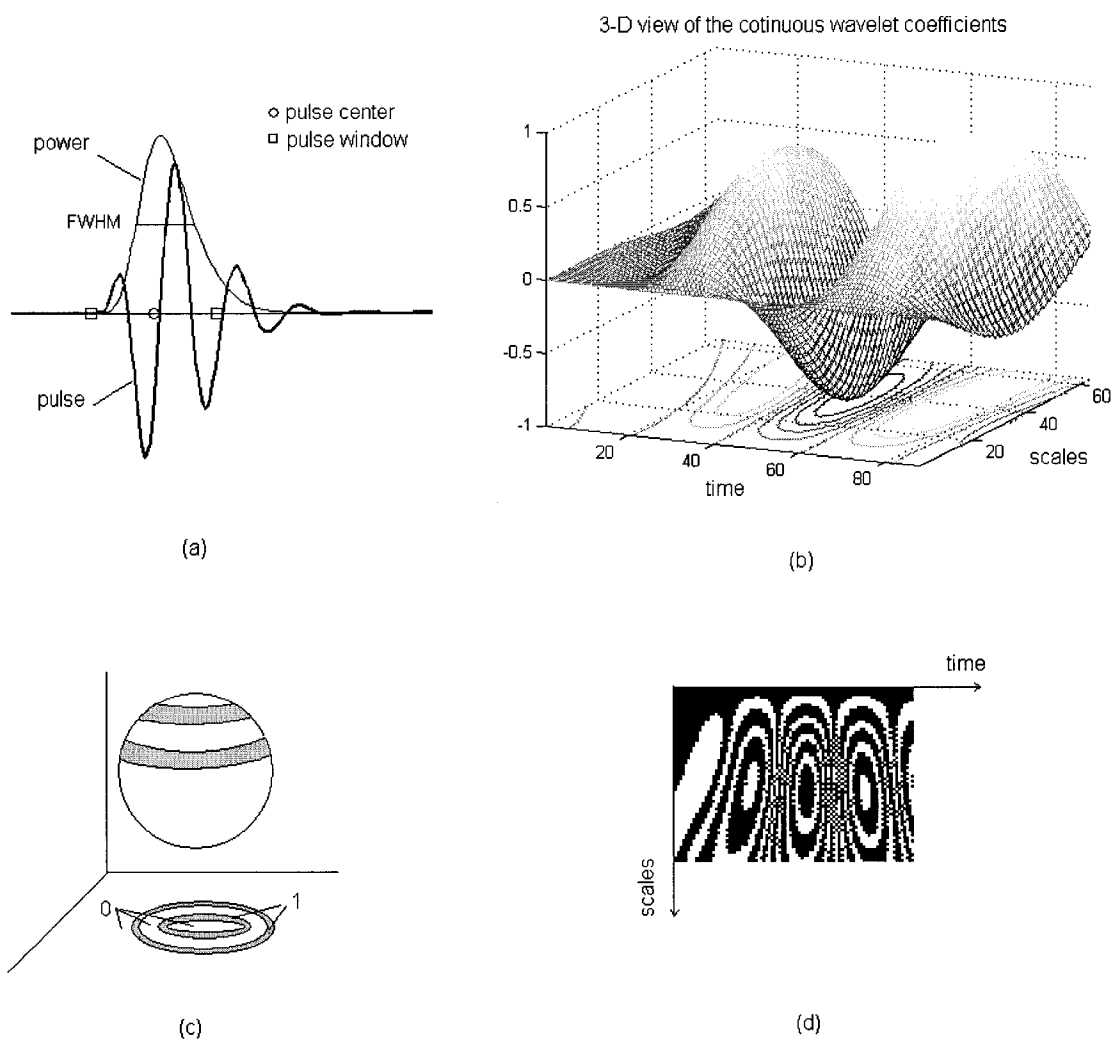


Figure 3.1 Wavelet fingerprints generation. (a) Ultrasound pulse; (b) 3-D view of the wavelet coefficients and its contour; (c) slice projection; (d) the dynamic wavelet fingerprint (b).

Once we have obtained the two-dimensional signature of the transient signal, we can convert the one-dimensional signal classification problem to a two-dimensional pattern recognition problem in order to make use of more advanced tools at our disposal.

In this chapter, we use the moment invariants [34] of the dynamic wavelet fingerprint to reduce the dimension of the two-dimensional pattern. Moment invariants are uniquely determined by an image and, conversely, determine the image. These properties of moment invariants facilitate pattern recognition in the machine vision applications [35].

The seven moment invariants developed by Hu [34] are presented as follows:

$$\begin{aligned}
\phi_1 &= \eta_{20} + \eta_{02} \\
\phi_2 &= (\eta_{20} - \eta_{02})^2 + 4\eta_{11}^2 \\
\phi_3 &= (\eta_{30} - 3\eta_{12})^2 + (3\eta_{21} - \eta_{03})^2 \\
\phi_4 &= (\eta_{30} + \eta_{12})^2 + (\eta_{21} + \eta_{03})^2 \\
\phi_5 &= (\eta_{30} - 3\eta_{12})(\eta_{30} + \eta_{12})[(\eta_{30} + \eta_{12})^2 - 3(\eta_{21} + \eta_{03})^2] \\
&\quad + (3\eta_{21} - \eta_{03})(\eta_{21} + \eta_{03})[3(\eta_{30} + \eta_{12})^2 - (\eta_{21} + \eta_{03})^2] \\
\phi_6 &= (\eta_{20} - \eta_{02})[(\eta_{30} + \eta_{12})^2 - (\eta_{21} + \eta_{03})^2] \\
&\quad + 4\eta_{11}(\eta_{30} + \eta_{12})(\eta_{21} + \eta_{03}) \\
\phi_7 &= (3\eta_{21} - \eta_{03})(\eta_{30} + \eta_{12})[(\eta_{30} + \eta_{12})^2 - (3\eta_{21} + \eta_{03})^2] \\
&\quad + (3\eta_{12} - \eta_{30})(\eta_{21} + \eta_{03})[3(\eta_{30} + \eta_{12})^2 - (\eta_{21} + \eta_{03})^2]
\end{aligned} \tag{3.5}$$

where $\eta_{p,q}$, $p, q \in \{0,1,2,\dots\}$, is the normalized central moment, which is defined by

$$\eta_{p,q} = \frac{\mu_{p,q}}{\mu_{00}^\gamma},$$

where $\gamma = \frac{p+q}{2} + 1$ and $\mu_{p,q}$ is the central moments defined by

$$\mu_{p,q} = \int_{-\infty}^{\infty} \int_{-\infty}^{\infty} (x - \bar{x})^p (y - \bar{y})^q f(x, y) dx dy$$

where the point (\bar{x}, \bar{y}) is the centroid of a two-dimensional image $f(x, y)$.

Table 3.1 lists the calculated moment invariants of the dynamic wavelet fingerprint in Figure 3.1d.

TABLE 3.1
MOMENT INVARIANTS OF A DYNAMIC WAVELET FINGERPRINT

| ϕ_1 | ϕ_2 | ϕ_3 | ϕ_4 | ϕ_5 | ϕ_6 | ϕ_7 |
|-----------------------|-----------------------|-----------------------|-----------------------|-----------------------|-----------------------|-----------------------|
| 4.23×10^{-1} | 2.61×10^{-2} | 5.21×10^{-5} | 3.48×10^{-4} | 2.46×10^{-8} | 5.38×10^{-5} | 7.37×10^{-8} |

3.3 Simulated Signals Analysis

In this section, we use simulated ultrasound signals to explore the behavior and significance of the proposed dynamic wavelet fingerprint and its corresponding moment invariants.

Figure 3.2 shows five different pulses and their dynamic wavelet fingerprints. These pulses have almost the same durations but different center frequencies: 1.0, 2.25, 3.5, 4.75 and 6.0 MHz. The wavelets used to form the DWFP images are Daubechies, Morlet and mexican hat wavelets [5].

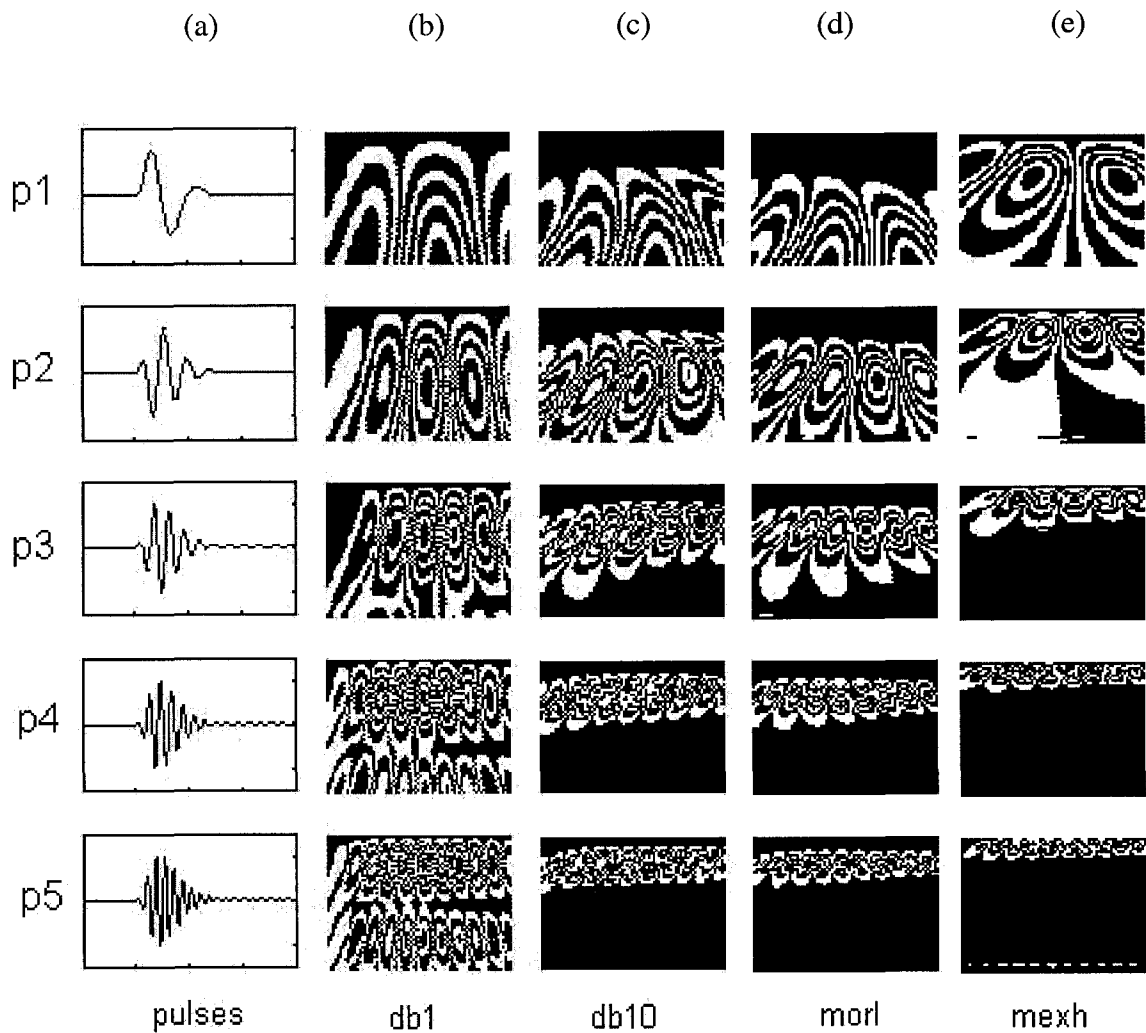


Figure 3.2 ---- Five pulses with different central frequencies and their dynamic wavelet fingerprints: (a) the pulses; (b) the Daubechies wavelet of order 1; (c) the Daubechies wavelet of order 10; (d) the Morlet wavelet; (e) the mexican hat wavelet.

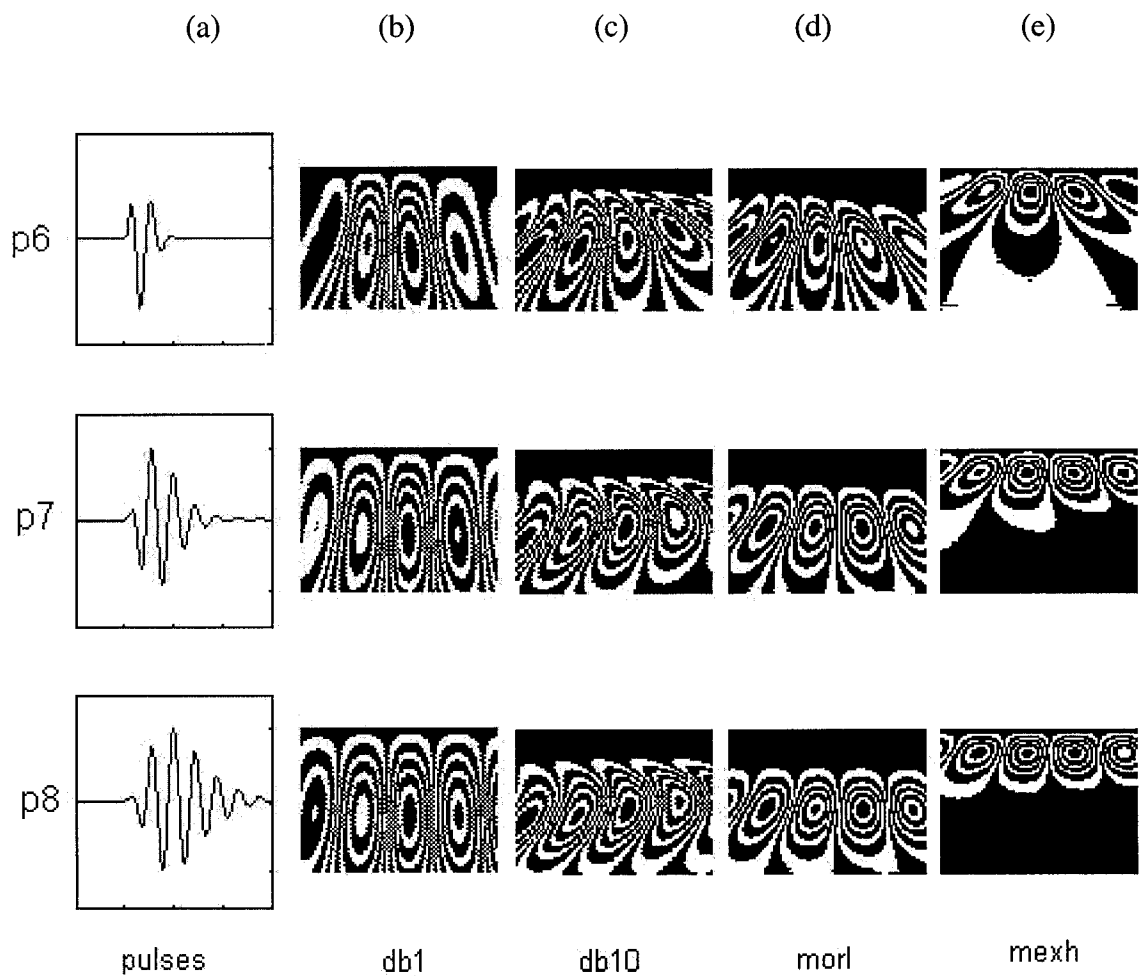


Figure 3.3 ---- Three pulses of 2.25 MHz center frequency with different durations and their dynamic wavelet fingerprints: (a) the pulses; (b) the Daubechies wavelet of order 1; (c) the Daubechies wavelet of order 10; (d) the Morlet wavelet; (e) the mexican hat wavelet.

Figure 3.3 shows another group of three pulses. They have the same 2.25 MHz center frequency but different durations. Again, the wavelets used to form the dynamic wavelet fingerprints images are Daubechies, Morlet and mexican hat wavelets.

The corresponding moment invariants of these dynamic wavelet fingerprints are listed in Table 3.2.

By comparing these images and numbers, some conclusions can be drawn as follows:

- As a two-dimensional pattern, the dynamic wavelet fingerprint is superior to the popular one-dimensional feature extraction method in that it is intuitive and self-explanatory. It directly highlights the differences between different signals.

- The dynamic wavelet fingerprint is sensitive to variations between signals. Pulses with the same duration but with different central frequencies have distinctly different fingerprints. On the other hand, with the same center frequency, pulses with different durations exhibit different fingerprints.

- The dynamic wavelet fingerprint is influenced by the wavelets used. For the same group of signals, some wavelets generate more differentiable patterns that lead to better classification performance than the others.

- Moment invariants change with corresponding dynamic wavelet fingerprints. As quantitative measures, they can be calculated as feature vectors for an automatic signal classifier.

TABLE 3.2
MOMENT INVARIANTS OF DYNAMIC WAVELET FINGERPRINT OF
DIFFERENT PULSES

| wavelet | pulse | ϕ_1 | ϕ_2 | ϕ_3 | ϕ_4 | ϕ_5 | ϕ_6 | ϕ_7 |
|---------|-------|----------|----------|----------|----------|-----------|-----------|-----------|
| db1 | P1 | 0.422229 | 0.028208 | 0.00146 | 0.000193 | -1.03E-07 | -3.02E-05 | -1.73E-08 |
| | P2 | 0.421988 | 0.029786 | 0.000893 | 0.000365 | 1.40E-07 | 3.25E-05 | -2.29E-07 |
| | P3 | 0.42188 | 0.019683 | 0.00297 | 0.000108 | 6.06E-08 | 1.46E-05 | 6.26E-09 |
| | P4 | 0.406239 | 0.019654 | 2.42E-05 | 0.000158 | -7.55E-09 | 2.02E-05 | 2.15E-08 |
| | P5 | 0.408049 | 0.019062 | 0.000105 | 0.00025 | -3.85E-09 | 3.32E-05 | -5.04E-08 |
| db10 | P1 | 0.469194 | 0.069544 | 0.000233 | 7.62E-05 | -2.94E-09 | -1.71E-05 | 8.84E-09 |
| | P2 | 0.4466 | 0.044185 | 0.001758 | 0.00015 | 1.29E-08 | 2.77E-06 | -5.44E-08 |
| | P3 | 0.519828 | 0.122571 | 0.013188 | 0.004085 | 2.94E-05 | 0.001301 | 4.08E-06 |
| | P4 | 0.747891 | 0.40358 | 0.00938 | 0.002275 | 9.32E-06 | 0.001091 | 3.00E-07 |
| | P5 | 0.9819 | 0.808212 | 0.006812 | 0.003124 | 1.41E-05 | 0.00233 | -3.90E-06 |
| morl | P1 | 0.500627 | 0.102185 | 0.002998 | 0.000386 | 2.43E-07 | 7.68E-05 | 1.50E-07 |
| | P2 | 0.458359 | 0.056972 | 0.001165 | 0.000137 | -2.70E-09 | -7.91E-06 | 4.89E-08 |
| | P3 | 0.450774 | 0.078576 | 0.005224 | 0.000901 | 1.92E-06 | 0.000253 | -2.02E-09 |
| | P4 | 0.775476 | 0.458108 | 0.019924 | 0.011048 | 0.000164 | 0.007458 | 5.08E-06 |
| | P5 | 1.144323 | 0.773773 | 0.039737 | 0.051209 | -0.00126 | 0.001684 | -0.00145 |
| mexh | P1 | 0.431961 | 0.017742 | 0.000285 | 2.54E-05 | 1.95E-09 | -5.91E-07 | -9.71E-10 |
| | P2 | 0.321164 | 0.025264 | 0.003185 | 0.002201 | 4.38E-06 | 0.000349 | 1.18E-06 |
| | P3 | 0.832875 | 0.567604 | 0.046867 | 0.037406 | 0.001566 | 0.028134 | 0.000195 |
| | P4 | 1.668968 | 1.003885 | 0.904339 | 0.412313 | 0.062484 | -0.20839 | -0.25257 |
| | P5 | 2.18924 | 0.493067 | 2.814274 | 2.185501 | 5.187905 | -1.50885 | -5.94448 |
| db1 | P6 | 0.413645 | 0.017284 | 0.00064 | 0.000132 | 3.66E-08 | 7.66E-06 | 1.66E-08 |
| | P7 | 0.42316 | 0.026091 | 5.21E-05 | 0.000348 | 2.46E-08 | 5.38E-05 | -7.37E-08 |
| | P8 | 0.424458 | 0.01834 | 6.35E-05 | 4.31E-05 | -2.10E-09 | 4.73E-06 | 1.99E-09 |
| db10 | P6 | 0.448 | 0.035953 | 0.000273 | 5.20E-05 | 4.98E-09 | 5.37E-06 | -9.57E-10 |
| | P7 | 0.449372 | 0.046767 | 0.000564 | 3.42E-06 | -1.19E-10 | -6.86E-07 | 7.07E-11 |
| | P8 | 0.445946 | 0.04509 | 0.000145 | 3.19E-05 | 2.17E-09 | 4.82E-06 | 6.66E-10 |
| morl | P6 | 0.47175 | 0.056089 | 0.001006 | 9.74E-05 | 2.06E-08 | 6.18E-06 | 2.18E-08 |
| | P7 | 0.47738 | 0.068592 | 1.39E-06 | 2.10E-06 | -3.52E-12 | 1.35E-07 | 4.71E-13 |
| | P8 | 0.44933 | 0.055813 | 0.000314 | 3.18E-05 | 1.57E-09 | -6.27E-06 | 2.32E-09 |
| mexh | P6 | 0.323953 | 0.006766 | 0.000462 | 0.000573 | -2.55E-07 | -4.47E-05 | -1.08E-07 |
| | P7 | 0.555676 | 0.164009 | 0.01067 | 0.002027 | 9.38E-06 | 0.000818 | 4.98E-07 |
| | P8 | 0.726366 | 0.370176 | 0.005418 | 0.001927 | 6.22E-06 | 0.001126 | -8.42E-07 |

Accordingly, it is possible to develop an automatic signal classification system to implement signal classification/ identification based on the dynamic wavelet fingerprint.

3.4 Application For Materials Sorting

As a demonstration, a dynamic wavelet fingerprint based automatic ultrasound signal identification system for materials sorting is presented below. The samples are five thin 305 by 305 mm (12 by 12 in.) plates of different materials as shown in Table 3.3.

TABLE 3.3
MATERIALS PROPERTIES OF SAMPLES [36]

| Materials | ρ (kg/m ³) | V_L (m/s) | V_T (m/s) | $z = \rho V_L$ (10 ⁶ kg/m ² s) |
|-----------|-----------------------------|-------------|-------------|--|
| Copper | 8.9x10 ³ | 4660 | 2260 | 41.8 |
| Steel | 7.8x10 ³ | 5660 | 3120 | 45.5 |
| Aluminum | 2.71x10 ³ | 6350 | 3100 | 17.2 |
| Glass | 2.51x10 ³ | 5770 | 3430 | 14.5 |
| Acrylic | 1.18x10 ³ | 2730 | 1430 | 3.2 |

The system setup is illustrated in Figure 3.4. It includes a 2.25 MHz transducer (V306 2.25/0.5, Panametrics Inc.), a C403 motion controller (Metrotek), a UTEX 320 pulser/receiver and an analog-to-digital converter (CompuScope 12100, Gage Applied Sciences, Inc.). The signal is digitized at a sample rate of 100 MS/s at 12 bits. The signals

are collected in a standard pulse-echo configuration in an immersion tank. The transducer was held perpendicular to the surface of the samples to obtain front face reflection echoes.

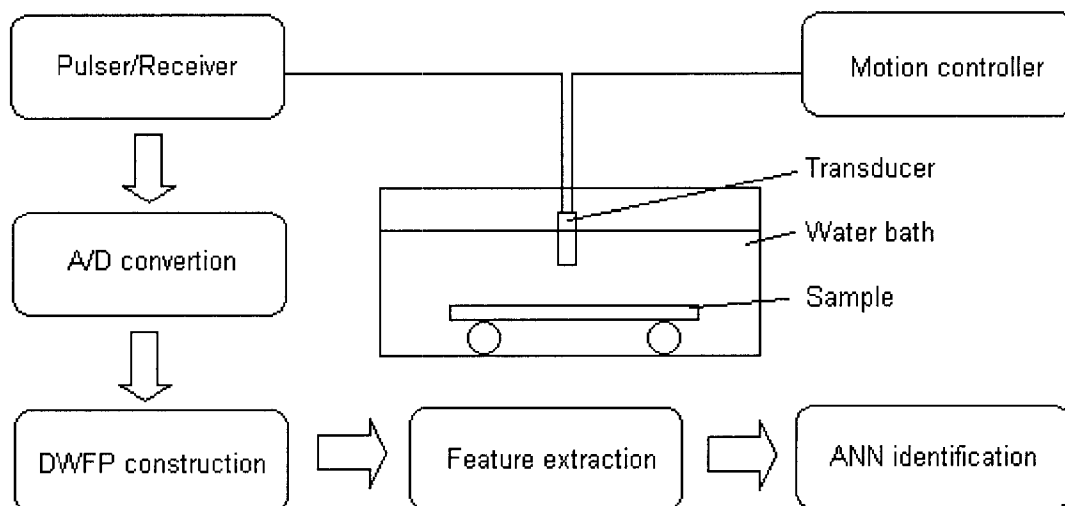


Figure 3.4 System setup for materials sorting.

The dynamic wavelet fingerprint is constructed as described above: locate the center of the reflected pulse, extract the pulse into a predefined window and make slice projection of the wavelet coefficients on to the time-scale plane. In this research, the initial input pulse is unknown. Instead, the size of the segment window is obtained by using a simulated pulse whose shape is approximate to the reflection echo from an aluminum plate surface.

For the feature vectors, however, instead of using one real wavelet to process the signal, three wavelets, including the Daubechies, mexican hat and Gaussian derivative wavelets, are used to generate dynamic wavelet fingerprints for each pulse, as illustrated in Figure 3.5. The feature vector is generated by the combination of the three first moment invariants (ϕ_1) of these dynamic wavelet fingerprints.

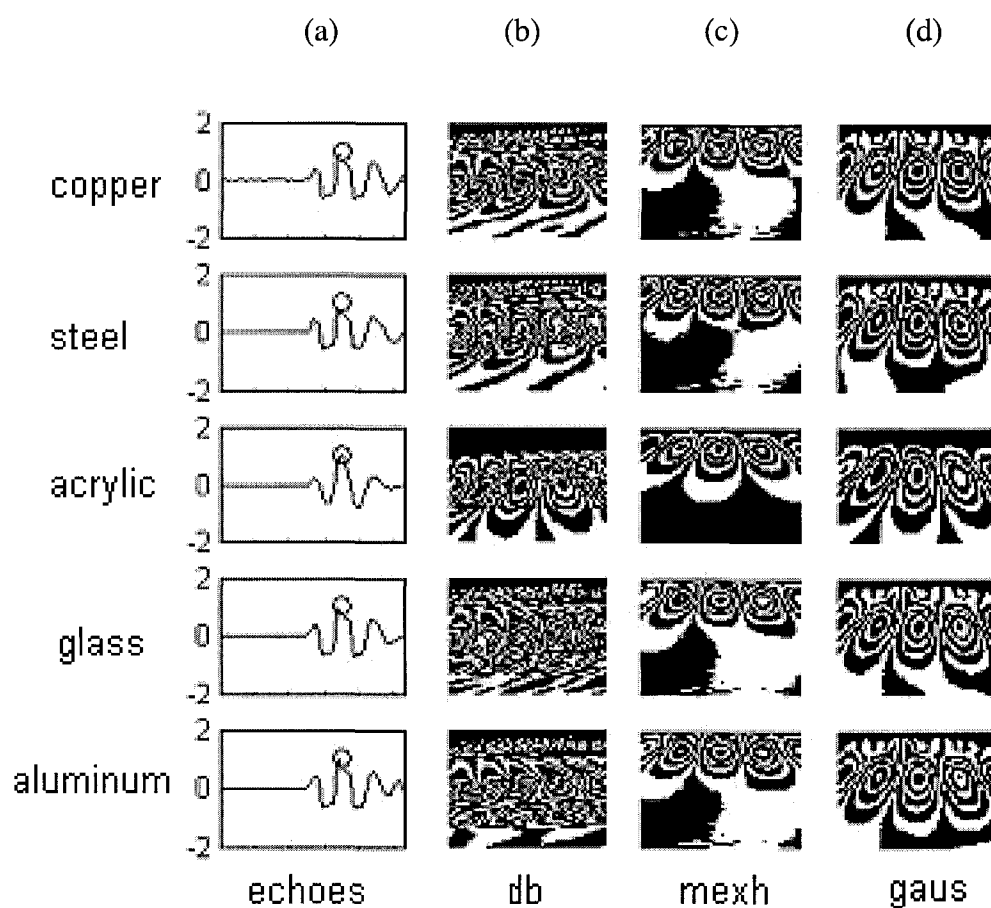


Figure 3.5 ---- Echoes from different material surface and their dynamic wavelet fingerprints. (a) echoes; (b) Daubechies wavelet of order 1; (c) mexican hat wavelet; (d) the sixth derivative of Gaussian wavelet.

To solve this classification problem, a two-layer feed forward neural network was used (Figure 3.6). The network is a two-layer log-sigmoid/log-sigmoid network. The first layer has 12 neurons and the output layer has 5 neurons. After being trained, the output of the network for every input waveform is then processed by a competitive transfer function. As a result, only the neuron corresponding to a specific material has an output value of 1, others have values of 0.

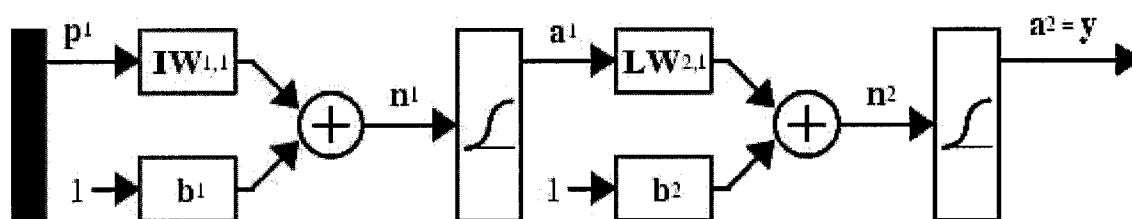


Figure 3.6 Artificial neural network used to sort materials.

For each of the five materials, 120 samples were acquired when moving the transducer randomly (at the same distance from the plate). These samples were then used as training and test sets respectively. There are 60 samples in each set. Figure 3.7 illustrates the neural network training process. After 361 epochs of training, the network learned to classify the training samples. The ratio of correct identification is 100% for both the training and testing set.

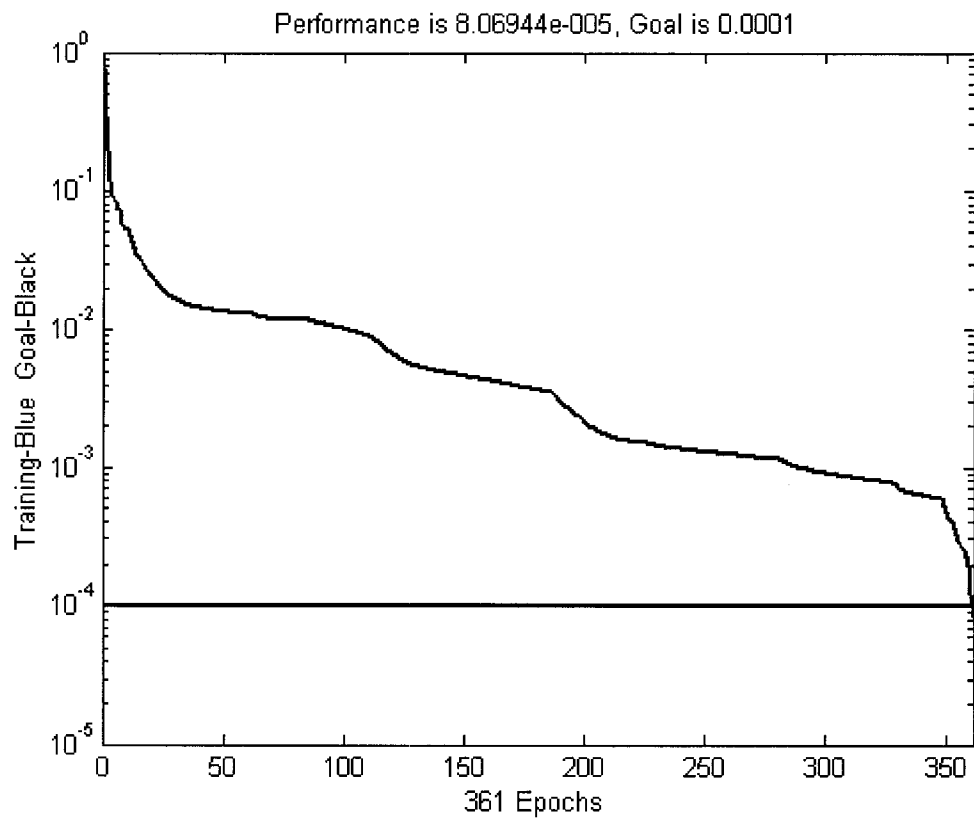


Figure 3.7 Artificial neural network training: performance as a function of training epochs (goal = 1×10^{-4}).

3.5 Conclusion

This chapter describes the development of the dynamic wavelet fingerprint technique. Put simply, this technique is a *combination* procedure for detection and characterization of transient signals. For detection, it makes use of the matched filter bank property of the wavelet transform to “sift out” candidate transient signals; for characterization, it takes the form of sliced projections of the three dimensional wavelet coefficient distribution, which is actually the time-scale (frequency) representation of the transient signal.

By analyzing simulated ultrasonic signals, it was found that the dynamic wavelet fingerprint is sensitive to variations between signals. However, for the same group of signals, some wavelets generate more easily differentiable patterns and lead to better classification performance than other wavelets.

Moment invariants were used in this chapter to extract features from the dynamic wavelet fingerprint. Although a systematic approach, the calculation of these moment invariants is time consuming. As will be seen in the following chapters, more efficient feature extraction methods can be developed for different applications.

As a demonstration, an ultrasonic material sorting system was developed based on the dynamic wavelet fingerprint technique. With an artificial neural network as the “brain”, the knowledge about the reflection signals from different materials was learned in terms of their distinctive dynamic wavelet fingerprints. After training, a perfect classification performance was achieved.

It is worth noting that the core idea behind the dynamic wavelet fingerprint technique is to transform a one-dimensional signal detection and characterization problem into a two-dimensional pattern recognition problem. Since the dynamic wavelet fingerprint is intuitive and self-explanatory, we can use it directly to “watch” the difference between signals rather than depending totally on some “black-box” operations to extract significant information. In addition, the dynamic wavelet fingerprint technique enables the use of more advanced tools, some of which are now being widely deployed for security applications, for example, fingerprint and face recognition. Finally, human knowledge can be more easily built up and artificial intelligence may be more easily integrated into an automatic system.

CHAPTER IV

ULTRASONIC PERIODONTAL PROBING

4.1 Introduction

Most adults have a mild form of periodontal disease, while over 20 percent of older Americans have severe periodontal disease [37-39]. Periodontal disease involves the loss of tooth connective tissue (attachment) with subsequent destruction of tooth-supporting bone, leading to loss of teeth. In addition to being a major cause of tooth loss, periodontal disease has recently been associated with several systemic diseases. Animal and population-based studies have demonstrated an association between periodontal disease and diabetes, cardiovascular disease, stroke, and adverse pregnancy outcomes [40-42]. Despite the widespread problem of periodontal disease today, currently available diagnostic tests are limited in their effectiveness. None are a completely reliable indicator of periodontal disease activity and the best available diagnostic aid, manually probing pocket depths, is only a retrospective analysis of attachment already lost [43-49]. In traditional manual probing, which is now routinely done in the general dentistry office [50], a metal probe is inserted between the soft tissue of the gingival margin (gum line) and the tooth (Figure 4.1). Using fixed markings on the probe, the depth of probe penetration is typically measured relative to the gingival margin.

Numerous studies have questioned the ability of the periodontal probe to accurately measure the anatomic pocket depth [51-54]. The degree of probe tip

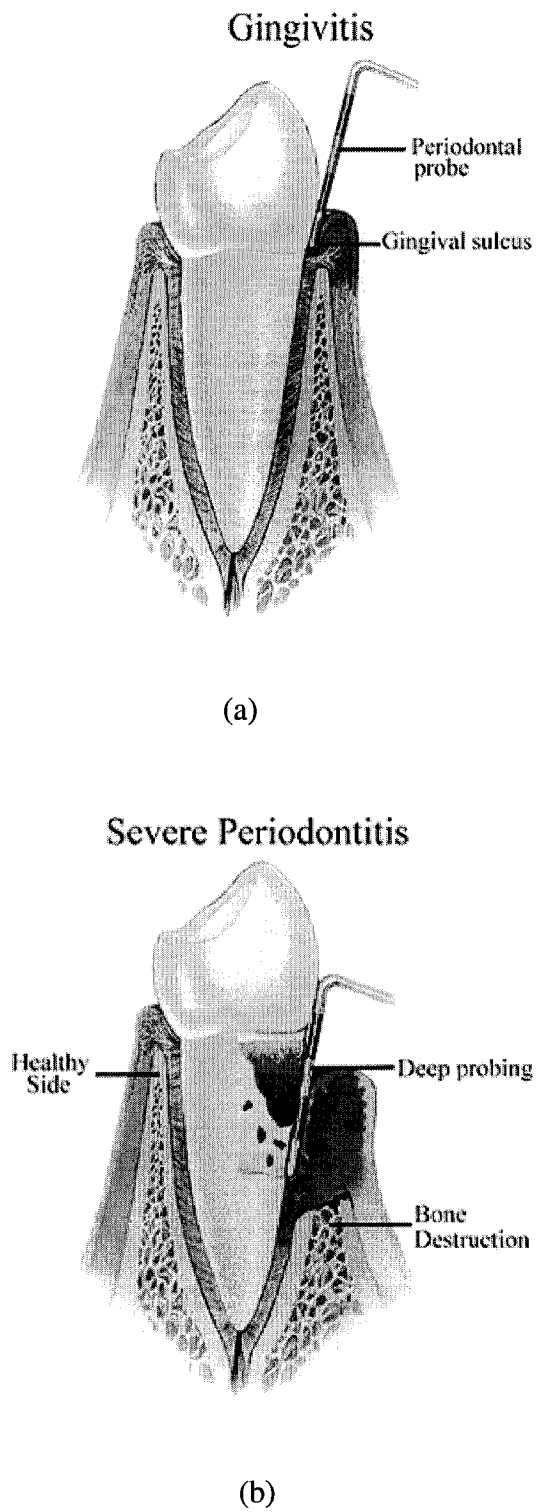


Figure 4.1 Traditional manual periodontal probing. (a) Gingivitis. (b) Severe Periodontitis.

penetration may be influenced by factors such as thickness of the probe, pressure applied, tooth contour, tooth position, presence of calculus, degree of periodontal inflammation, and the actual level of connective tissue fibers [55-60]. As a result, probing measurements may overestimate attachment loss by as much as 2 mm in untreated sites, while underestimating attachment loss by an even greater margin following treatment [61,62]. The development of automated, controlled-force probes has reduced some of the operator-related error and subjectivity inherent in manual probing techniques [63-66]. However, standardized probing forces do not address anatomic and inflammatory factors [67,68].

The first tests of ultrasonic imaging of the periodontal space attempted to image the crest of the alveolar bone by aiming the ultrasound transducer perpendicular to the long axis of the tooth [52,69,70]. While these efforts proved the feasibility of ultrasonic imaging in dentistry, this version of the technique could not detect periodontal attachment loss, and failed to gain clinical acceptance. Recently, researchers have begun exploring new uses of ultrasound in dentistry [71-74] and studies have been conducted using ultrasound to image the periodontal pocket space by aiming the transducer apically into the pocket from the gingival margin [75-81]. The major technical barrier to this approach is providing an efficient coupling medium for the ultrasonic wave into the thin (0.25 - 0.5 mm) periodontal pocket. The probe described by Hinders and Companion uses a slight flow of water to couple the ultrasound wave into the pocket space. A hollow tip placed over the transducer narrows the ultrasonic beam, so that the beam is approximately the same width as the opening into the sulcus at the gingival margin.

The ultrasonic probe works by projecting a narrow, high-frequency (10-15 MHz) ultrasonic pulse into the gingival sulcus/periodontal pocket, and then detecting echoes of the returning wave. The time series return signal (A-scan) can then be converted into a depth measurement by multiplying the time of arrival of the return signal by the speed of sound in water (1500 m/s) and dividing by two (since the signal travels into the pocket and back). Ultrasonic probing is entirely painless, is as fast as manual probing, and has the potential to yield much more diagnostic information by providing the dentist and patient with a graphical representation of changes in pocket depth. However, due to the inherent complexity in the way ultrasonic waves interact with the inner structure of periodontal anatomy, it is unrealistic to train a dental hygienist to read out each pocket depth by watching and interpreting the echo waveform. Automated interpretation of these echoes is what enables a practical clinical system.

As an initial effort to automate interpretation of the echoes, a time domain procedure was developed to simplify the waveforms and infer the depth of the periodontal pocket [79-81]. This procedure used a slope-detection algorithm to pick peaks in the A-Scan signal, followed by smoothing and averaging operations to eliminate small random variations. The pocket depth was then inferred by dividing the simplified waveform into three regions and assuming the second transition from weaker peaks to noise as the estimation of the bottom of the periodontal pocket. Unfortunately, in many cases it was difficult or even impossible to define three such distinctive regions based on the echo amplitude. Even if the second transition point can be called out in some way, the depth of the periodontal pocket can only be inferred from it approximately. To overcome

these limitations, information other than echo amplitude should be used to develop sensitive and reliable models to estimate the bottom of the periodontal pocket.

The wavelet transform (WT) can be constructed as a bank of matched filters if the mother wavelet is chosen to be an efficient representation of the input signal itself, so it has been widely used to solve detection/estimation problems [21,82-85]. As a multi-resolution analysis approach, the WT is also an effective method to extract significant information from dynamic signals, which is often the key in automated signal classification applications [26,28,29,33,86]. To take advantage of this potential of the WT, a dynamic wavelet fingerprint technique [87] was adapted to develop a signal processing algorithm for the ultrasonic periodontal probe. In this approach, potential scattering centers are first detected by picking peaks in the scale averaged power (SAP) curve. A two-dimensional black and white pattern, called a DWFP, is then generated at each peak location to characterize the local transient signal. A two-dimensional FFT procedure is then applied to generate an inclination index for each DWFP pattern. The bottom of the periodontal pocket is then estimated from the third broad peak of the inclination index curve.

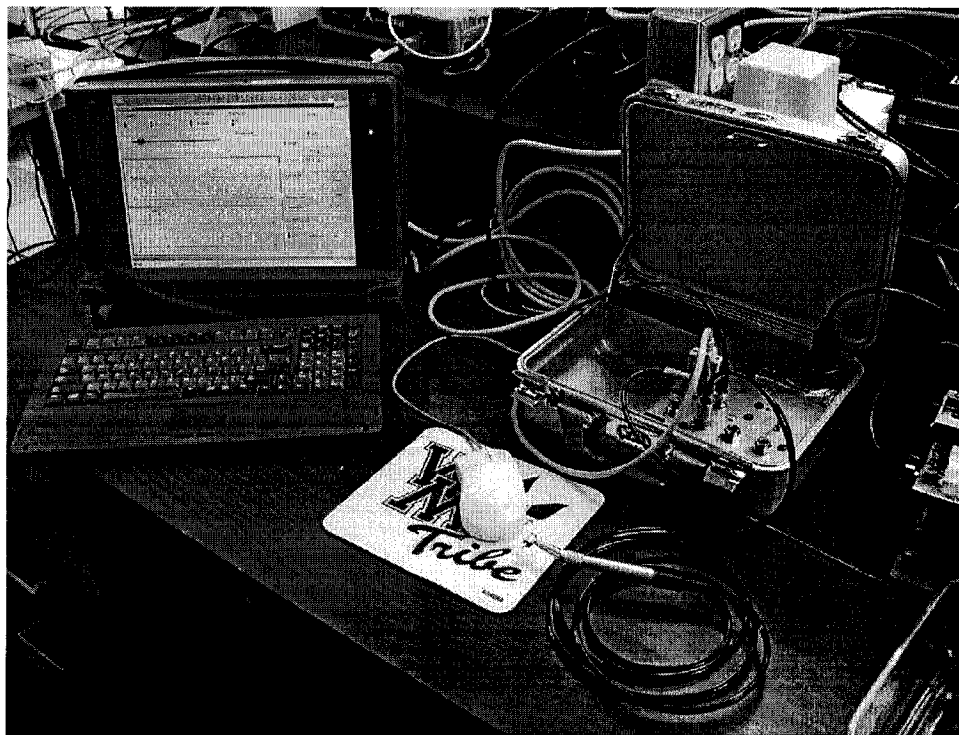
This chapter is organized as follows. In Section 4.2, the experimental device and procedure are described. The algorithm used in this work is discussed in Section 4.3. The results are presented in Section 4.4. A discussion and conclusion is given in Section 4.5.

4.2 Clinical Instrument and Signals

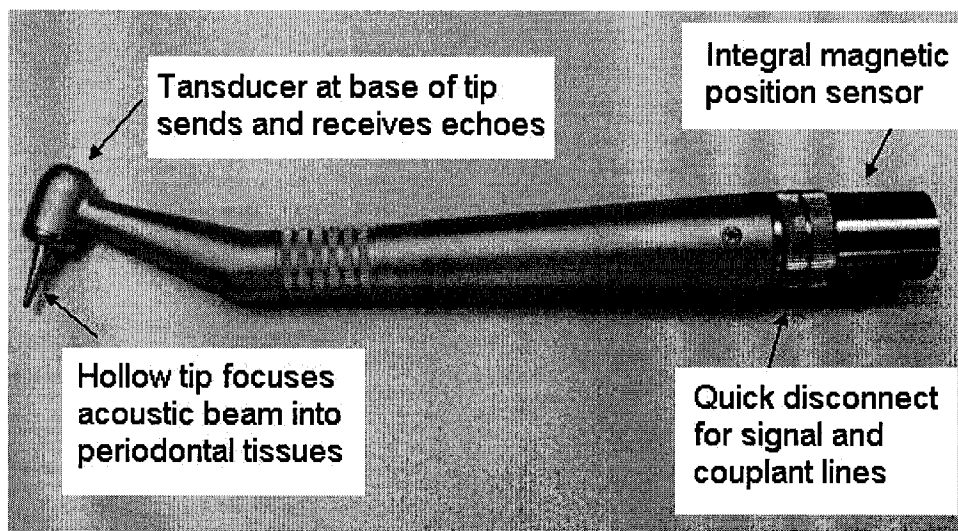
As shown in Figure 4.2, an ultrasonic periodontal probe was operated using a portable computer system. The probe handpiece included a 10 MHz piezo-composite transducer with a 2 mm-diameter active area. The transducer was housed within a contra-angled handpiece at the base of a hollow conical tip. The tip was designed to narrow the ultrasonic beam profile to 0.5 mm and to provide an area for water to sustain the ultrasonic wave and carry it into the periodontal pocket.

Figure 4.3 illustrates how the ultrasonic probe is used to explore the periodontal pocket. A stream of water is used as couplant to launch ultrasound energy into the periodontal pocket. The ultrasound wave interacts with the periodontal tissue and echoes carry relevant information back to the transducer. During operation, the ultrasonic probe is held in a pose similar to manual probing but with its tip touching the gingival margin. The ultrasonic probe is momentarily held in place at each of the standard probing locations to acquire a series of ultrasonic A-scan signals that are digitized and saved in the computer for later analysis. Water flow and data acquisition is automated via foot pedal control.

At Valley Periodontics, Appleton, WI, 14 patients were examined both by hand and by the ultrasonic instrument on two visits scheduled three months apart. For each patient, full mouth probing was carried out, first by hand and then by the ultrasonic instrument. For each of up to 32 teeth for each patient, a periodontist performed probing at 6 sites (facial distal, facial middle, facial mesial, lingual distal, lingual middle and lingual mesial), providing up to 192 corresponding ultrasonic and manual probing



(a)



(b)

Figure 4.2 The ultrasonic periodontal probing system. (a) overview of the system; (b) the ultrasonic probe handpiece.

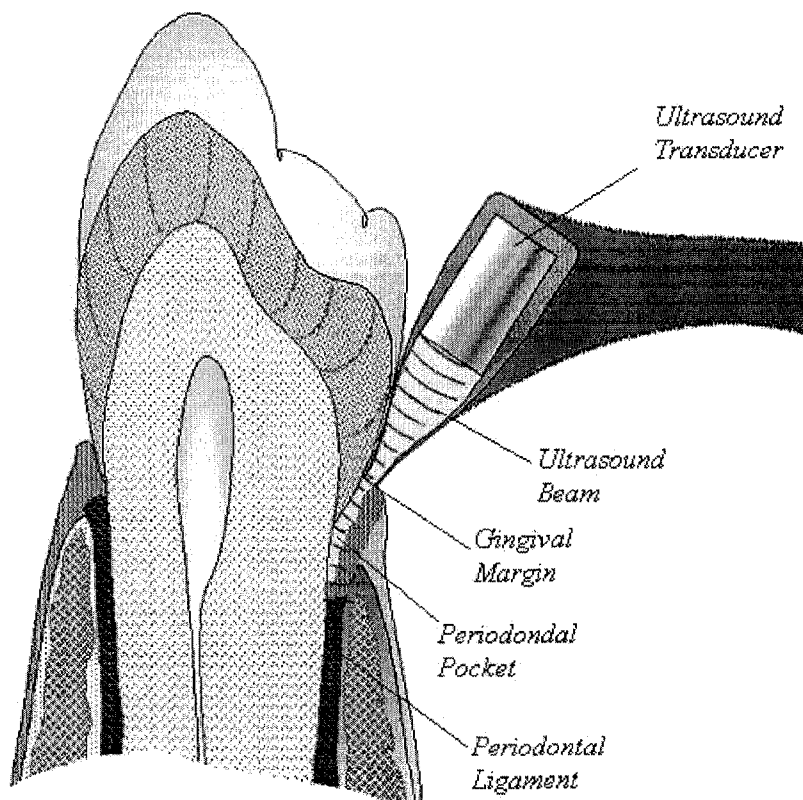


Figure 4.3 Schematic of ultrasonic periodontal probing.

measurements per patient.

A typical A-scan signal obtained is shown in Figure 4.4(a). The horizontal axis represents the time from 0 to 20.48 μsec at 100MHz sampling rate. The vertical axis represents normalized voltage on an arbitrary scale digitized at 12 bits. The strong reflection region before point 2.5 μsec arises from the echoes internal to the probe tip. After point 2.5 μsec , it is the signal from the periodontal anatomy.

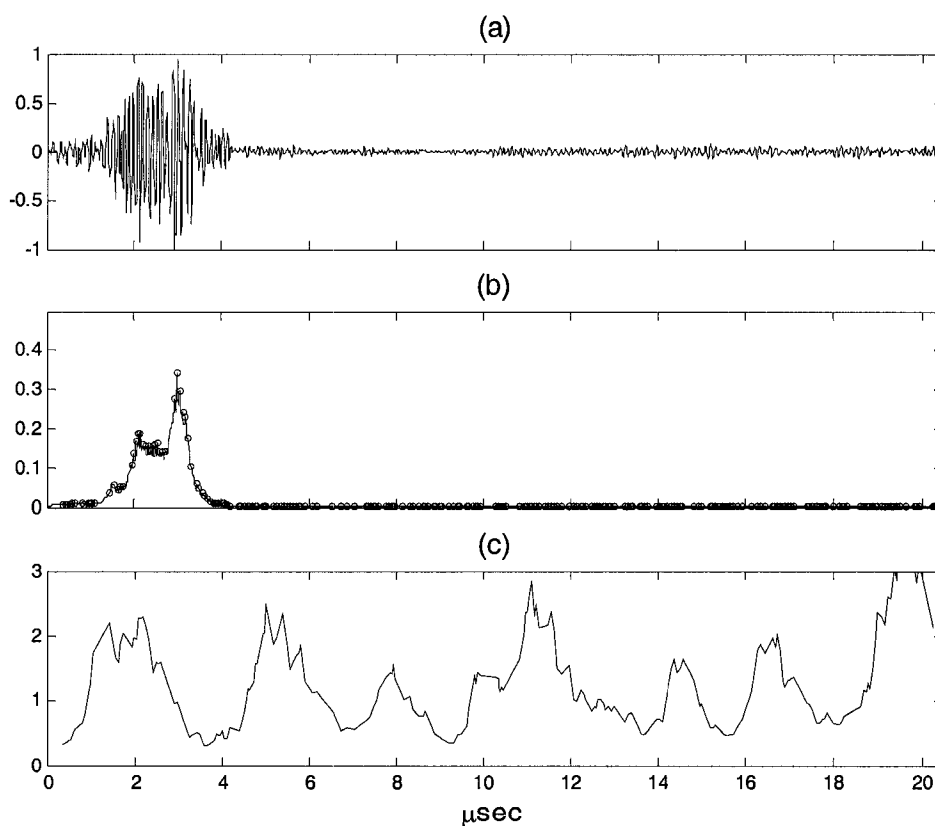


Figure 4.4 Illustration of signal processing for ultrasonic periodontal probing. (a) Original A-scan signal, (b) SAP peaks marked by the small circles, (c) The inclination index curve. The third significant peak (at about 8 μsec) corresponds to the estimated location of the bottom of the periodontal pocket.

4.3 Algorithm Development

A flowchart of the proposed algorithm is shown in Figure 4.5, which involves three main steps: echo detection/characterization, echo classification, and echo identification.

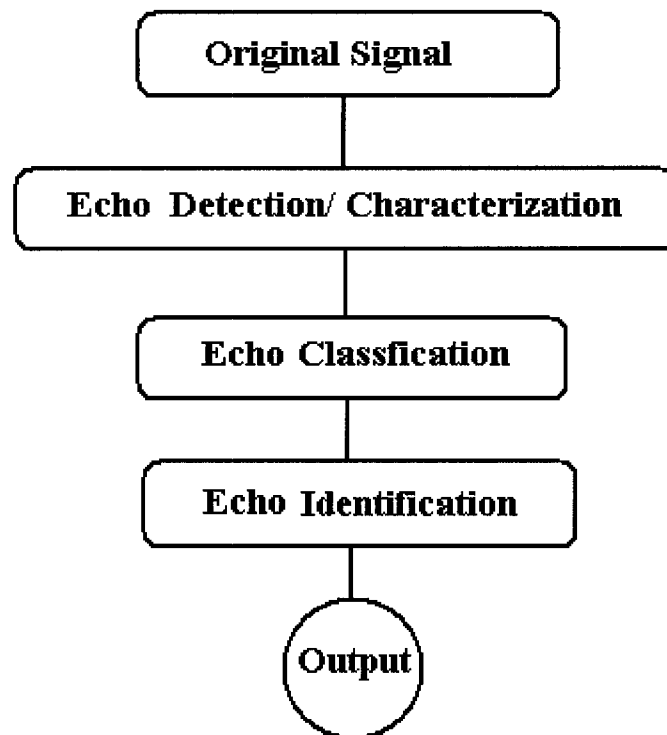


Figure 4.5 Flowchart of the algorithm used to process ultrasound signal to detect the bottom of the periodontal pocket.

Since the bottom of the periodontal pocket can be considered as a significant discontinuity of the periodontal tissue, there should be an echo at corresponding location. The dynamic wavelet fingerprint (DWFP) technique introduced in chapter III and

presented in [87] is adapted here for echo detection and echo recognition. It generates a simplified and intuitive two-dimensional pattern in time-scale domain for each detected echo so that significant features can be extracted directly by watching the patterns or by using advanced pattern recognition techniques. These features then can be used to identify the specific echo of interest.

The proposed algorithm is described in detail as follows: first, the scale-averaged wavelet power (SAP) proposed by Georgiou and Cohen [33] was calculated, i.e.,

$$W_a^2(n) = \frac{1}{J} \sum_{j=1}^J |W(s_j, n)|^2, \quad (4.1)$$

where $W(s_j, n)$ is the continuous wavelet coefficients at scale s_j and position n , i.e.,

$$W(s_j, n) = \frac{1}{\sqrt{s_j}} \int_{-\infty}^{\infty} x(t) \psi_0^* \left(\frac{t-n}{s_j} \right) dt \quad (4.2)$$

where $x(t)$ is the signal to be analyzed; ψ_0 is the mother wavelet; and * denotes conjugate.

The result obtained by (4.1) was then smoothed by a median filter to generate an SAP curve. According to Georgiou and Cohen, the significant SAP peaks correspond to coherent scattering centers that can be differentiated from the diffuse background. Here the SAP peaks were picked out wherever the sign of the first derivative of the SAP curve changed from positive to negative as shown in Figure 4.4(b). Assuming that the bottom of the periodontal pocket belongs to such coherent and resolvable scattering centers, and that it can be detected as one of the SAP peaks, the question now is how to differentiate it from other scatterers.

To suppress noise and high frequency interference that may cause distortion of the DWFP pattern generated later, a pruning procedure [11] based on the stationary discrete wavelet transform [32] was applied to the original A-scan signal, i.e.,

$$W_s(a,b) = 0 \quad \text{for } a = 1 \dots 5 \quad (4.3)$$

where $W_s(a,b)$ is the stationary discrete wavelet coefficients at scale a and time b .

Next, a continuous wavelet transform was performed on the pruned A-scan signal using the Morlet wavelet [5,15]:

$$\psi(x) = C e^{-x^2/2} \cos(5x) \quad (4.4)$$

where the constant C is used for normalization. Different choices for the mother wavelet will, of course, give different DWFPs [87] with some better highlighting features of interest in the signals under study than others. For the ultrasonic periodontal probing data the Morlet wavelet seemed to give DWFP sequences dominated by “loop” features with varying inclination, which could then be quantified in an automatic way.

For each peak in the SAP curve, the wavelet coefficients in its neighborhood are normalized into the range of [-1, +1] and then projected onto the time-scale plane to generate a two dimensional black and white pattern [87]. A typical DWFP sequence obtained is shown in Figure 4.6. In each frame of the sequence, time is the horizontal axis and wavelet scale is the vertical axis. This gives an abstract two-dimensional representation which allows “patterns” in the data to be recognized even when none are evident in the one-dimensional waveforms.

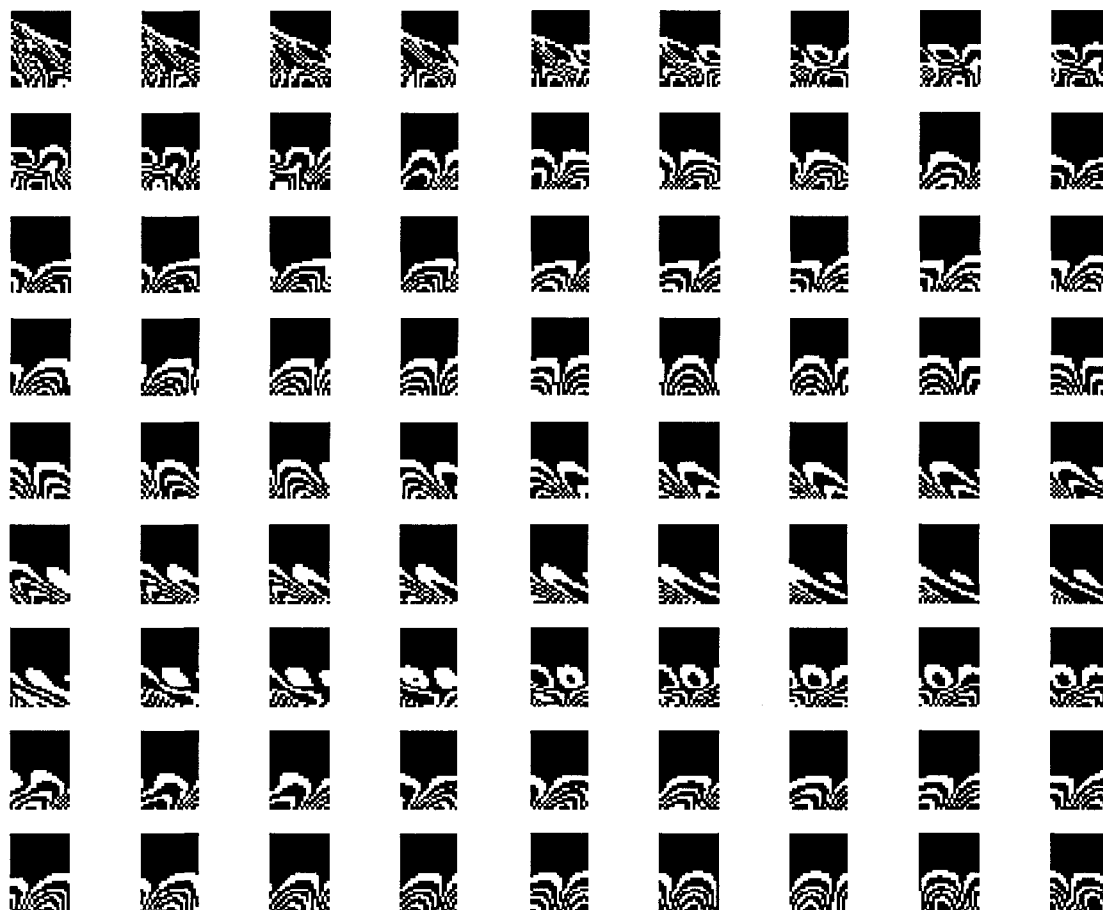


Figure 4.6 Typical DWFP sequence of an A-scan signal (time sequence: from left to right, from top to bottom).

By observing the DWFP sequences carefully, it was noted that these DWFP patterns change their inclination regularly, i.e., from left inclined to vertical and to right inclined, and repeating. A two-dimensional FFT based approach was designed to quantitatively characterize such variations.

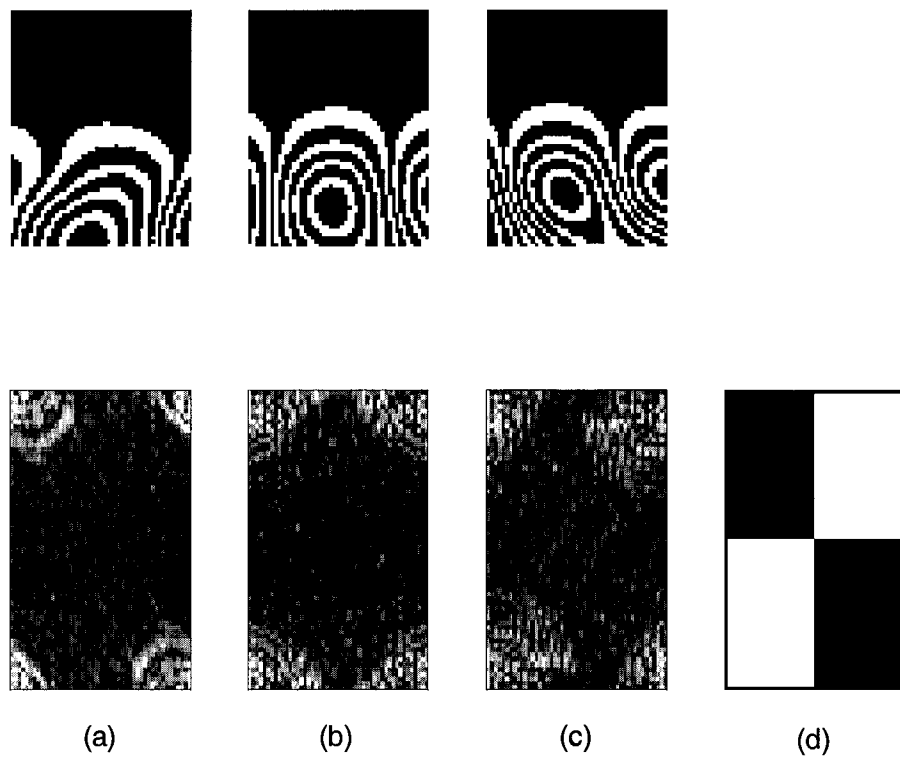


Figure 4.7 Two-dimensional FFT images of three typical DWFP patterns. (a) Right inclined DWFP and its two-dimensional FFT image (b) Vertical DWFP and its two-dimensional FFT image (c) Left inclined DWFP and its two-dimensional FFT image (d) Two regions (shaded quadrants and un-shaded quadrants) used to calculate the inclination index of the two-dimensional FFT image.

Figure 4.7 shows three typical DWFP patterns from such a sequence along with their corresponding two-dimensional FFT images. For the right inclined DWFP, it can be seen that its image is left diagonally dominated, i.e., there are more bright pixels at the top-left and bottom-right corners than at the top-right and bottom-left corners. On the contrary, for the left inclined DWFP, its image is right diagonally dominated. For the vertical DWFP, its two-dimensional FFT image is almost symmetric.

Based on these observations, each two-dimensional FFT image was divided into two pairs of quadrants as shown in Figure 4.7(d). An inclination index, I_x , was defined as the ratio of the number of white pixels in the shaded quadrants to that in the un-shaded quadrants. The DWFP sequence was then mapped into an I_x curve as shown in Figure 4.4(c). The regular variation of the DWFP is thus displayed as identifiable peaks and valleys.

To better explore the relationship between this intuitive pattern variation and the complex physics behind it, the same system was used to probe a simplified phantom built of a block of stainless steel with holes of different depths (Figure 4.8). This sort of phantom is typically used to calibrate new automatic periodontal probes, and although it doesn't represent all of the complicated periodontal pocket anatomy it does provide us with an ultrasonically well-characterized system with which we can be certain that our algorithms are isolating true ultrasonic echoes from noise/artifacts inherent in the probing measurement.

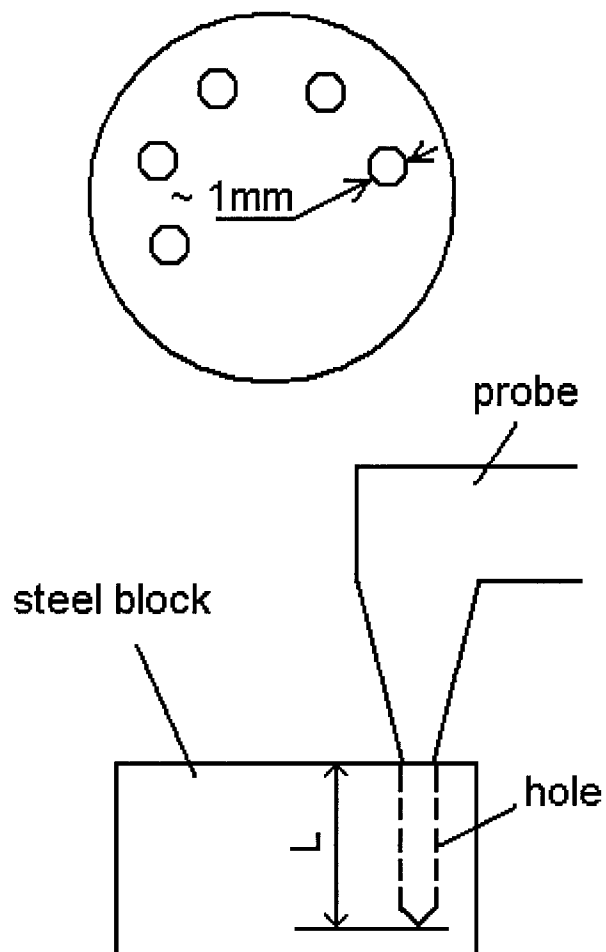


Figure 4.8 Phantom probing using the ultrasonic probe.

Figure 4.9 illustrates an A-scan signal from this phantom and its corresponding processing results. In the I_x curve, similar peaks and valleys can be seen as in Figure 4.4(c). It is clear that the first significant peak corresponds to the reflection from the probe tip at about $2.5 \mu\text{sec}$, and the third significant peak is close to the reflection from the bottom of the hole. As for the second significant peak in between, it is assumed to be caused by the interference of the water flow and the reflections of the wall of the hole.

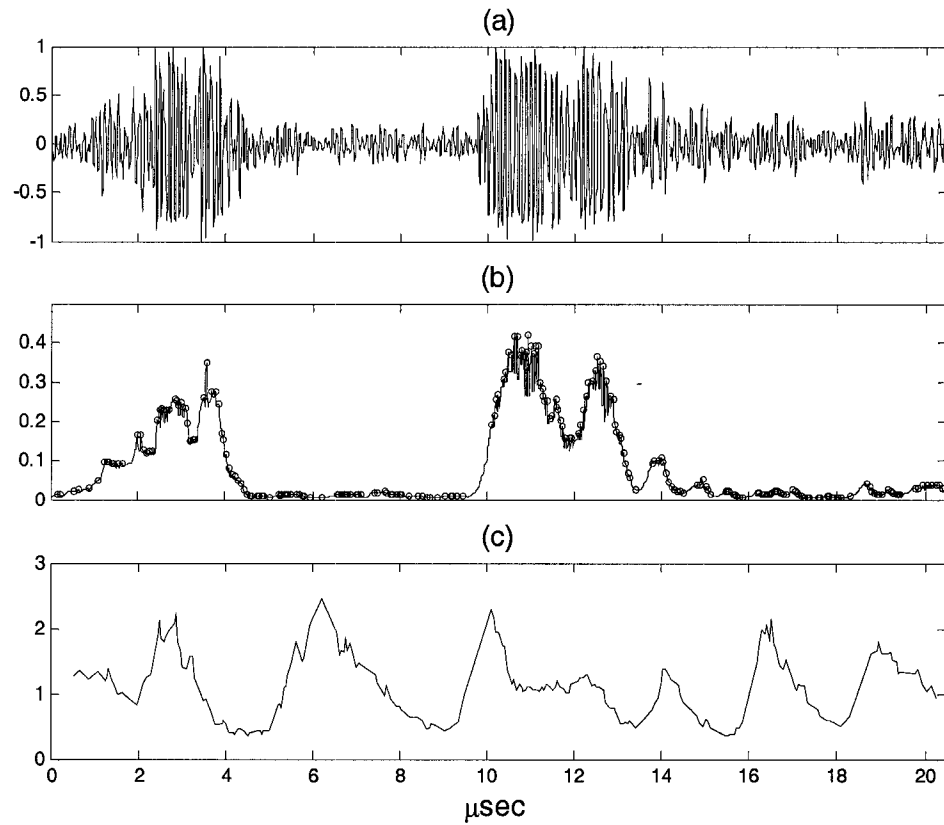


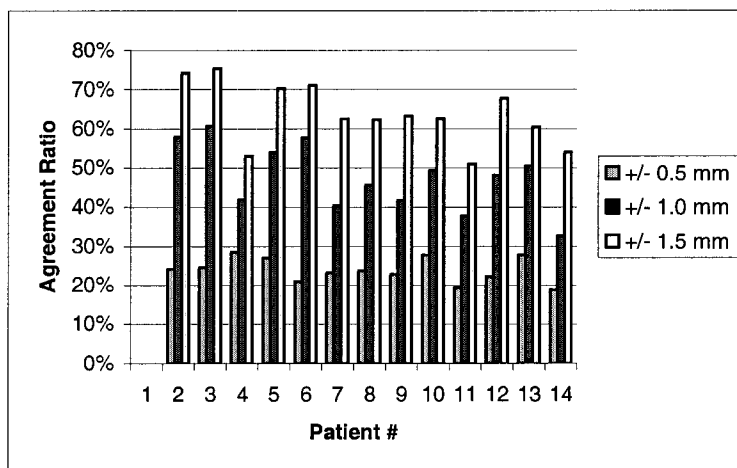
Figure 4.9 Phantom probing signal and corresponding processing results. (a) Original A-scan signal, (b) SAP peaks (c) the inclination index curve. The third broad peak corresponds to the reflection from the bottom of the hole.

Accordingly, a qualitative explanation was proposed to describe the regular peaks and valleys in the Ix curve of the ultrasonic periodontal probing signal: the first significant peak arises from the probe tip, the second significant peak may be caused by the tooth surface, and the third significant peak may correspond to the bottom of the periodontal pocket. After the location of the bottom of the periodontal pocket is estimated as above, the pocket depth is calculated as the product of the time delay from the probe tip and the speed of ultrasound in water ($1.5\text{mm}/\mu\text{sec}$), then divided by two.

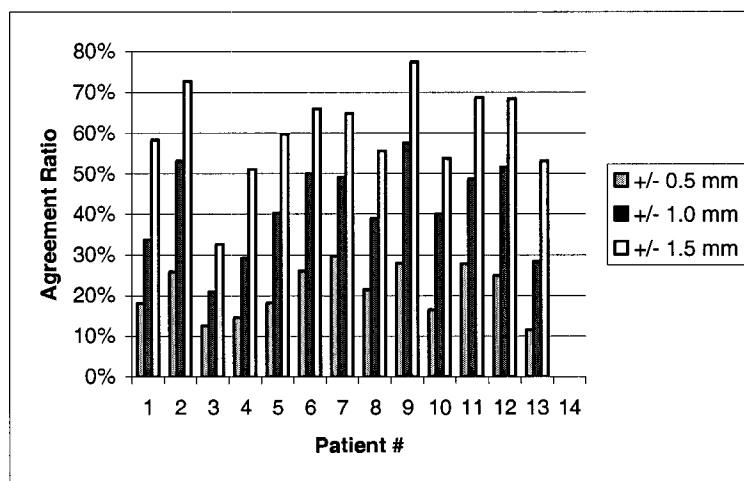
4.4 Results

A MatLab® (The MathWorks, Inc) program was developed to process full mouth ultrasonic probing data of 14 patients acquired during two clinical sessions. It works in off-line mode and runs automatically until all of the digitized A-scan signals are processed.

Because of the lack of any ideal standard to compare with, we take the manual probing result as the “gold standard” and compare it with ultrasonic probing, keeping in mind that an accuracy of ± 1 mm for manual probing is perhaps being generous. Ultrasonic probing readings were compared with manual probing readings at each probing site. If we allow for the “error bar” of ± 0.5 mm, ± 1 mm and ± 1.5 mm respectively, the agreement ratio (number of ultrasonic probing measurements within the “error bar” divided by number of total ultrasonic probing results) is about 20%, 40% and 60% correspondingly as shown in Figure 4.10.



(a)



(b)

Figure 4.10 Ratio of agreement of ultrasonic probing vs. manual probing. (a) May 18, 2001 (b) August 17, 2001. Note that results for patient #1 in (a) and patient #14 in (b) are unavailable due to personal absence in corresponding clinical visit.

Statistically, the agreement between ultrasonic probing and manual probing was evaluated by the Bland-Altman method [88].

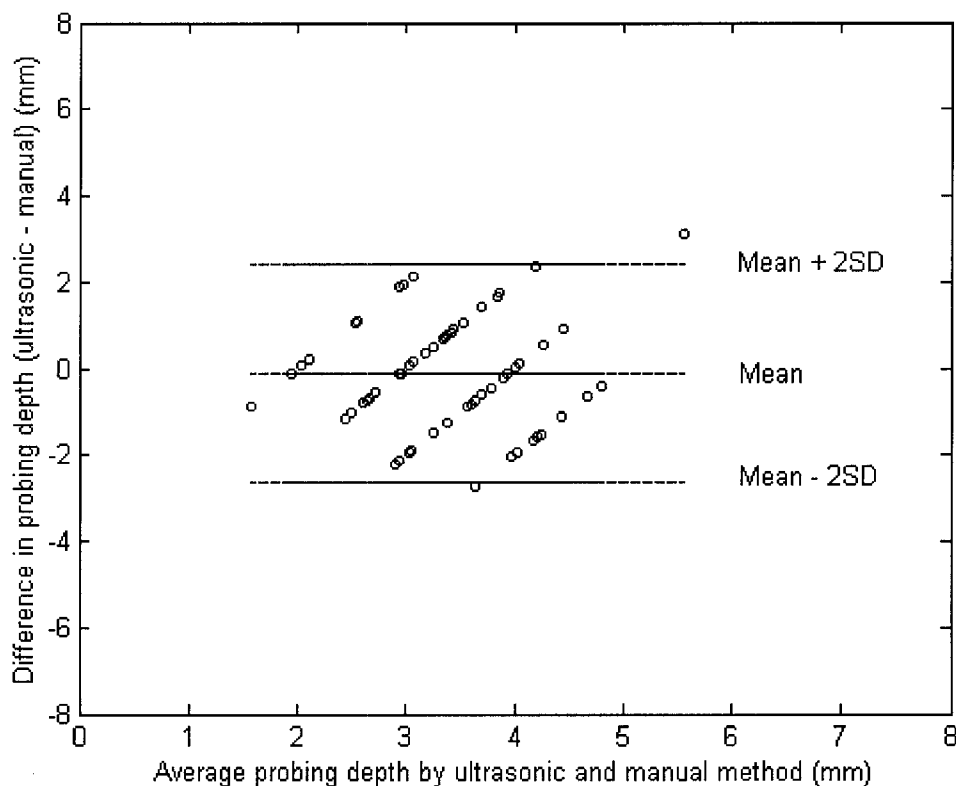


Figure 4.11. Difference against mean for periodontal probing depth of Patient #2, May 18.

As an example, a plot of the difference between the methods and their mean was drawn for patient #2, May 18, in Figure 4.11. It seems that the difference does not increase with the mean. The regular gaps are due to integer measurements of manual probing. Assuming that the difference is normally distributed, the mean difference \bar{d} and

the standard deviation SD of the difference was calculated as $\bar{d} = -0.1128$ and SD = 1.2611. The “limits of agreement” can be obtained as:

$$\bar{d} - 2SD = -0.1128 - (2 \times 1.2611) = -2.635 \text{ mm}$$

$$\bar{d} + 2SD = -0.1128 + (2 \times 1.2611) = 2.409 \text{ mm}$$

According to Bland and Altman, about 95% of differences will lie between these limits. In other words, the ultrasonic probing depth may be 2.6 mm below or 2.4 mm above the manual probing depth. The precision of the estimation of \bar{d} , $\bar{d} + 2SD$ and $\bar{d} - 2SD$ can be evaluated by using 95% confidence interval of a *t*-distribution with *n*-1 degree of freedom, where *n* is the sample size. For the patient chosen above, these confidence intervals were obtained as [-0.3818 0.1563], [1.9433 2.8754] and [-3.1010 -2.1689], respectively. Similar calculations were performed on other data sets (see Appendix B) and the results were presented in Tables 4.1 and 4.2.

Taking the non-zero mean into consideration, the “limits of agreement” are generally in the range of ± 3 mm. This may indicate a lack of agreement between ultrasonic probing and manual probing, which could be caused by several factors. The specific anatomical features measured by the two methods may be different; the probing point and angle may not be exactly same. More likely, it may arise from the model used in the algorithm. As mentioned above, the regular variation of the inclination of the DWFP patterns is motivated by an experiment on a steel block phantom, which is not entirely representative of the problem at hand, even though it does eliminate the sizeable error in the manual probing “gold standard.” To better understand the regular variation of

the DWFP patterns, a more accurate model should be developed guided by systematic clinical experiments carried out in the future.

4.5 Conclusions

An ultrasonic periodontal probing instrument is being developed. It uses a hollow water-filled tip to couple the ultrasound energy into and back out of the periodontal pocket, thus probing the periodontal anatomy by a non-invasive, painless and automatic technique. Key to automation of the probing is an ultrasonic signal processing algorithm for the periodontal probing instrument, which uses the dynamic wavelet fingerprint technique to detect and characterize the transient signals that arise from each suspected scatterer and estimate the location of the echoes corresponding to the bottom of the periodontal pocket.

In its original form, the ultrasonic waveform of periodontal probing is too complex to be understood even by experts. The reflections from the bottom of the periodontal pocket, which is the target of interest, are not evident and are mixed with other interference echoes due to other periodontal structures. The dynamic wavelet fingerprint technique visualizes the variation of the waveform and highlights the hidden features in the original one-dimensional waveform.

For this specific application, it is found that the regular change of inclination of the dynamic wavelet fingerprints can be used to distinguish different regions along the path of the probing ultrasound. Accordingly, instead of using moment invariants as in

Chapter III, a two-dimensional FFT procedure is designed to extract and quantify that inclination feature. Finally, the location of the bottom of the periodontal pocket is estimated by the third significant peak in the inclination index curve.

Clinical data from 14 patients have been processed with the proposed algorithm. Site by site comparison shows about 40% agreement ratio between ultrasonic and manual probing at the tolerance of ± 1.0 mm. Statistically, however, lack of agreement between ultrasonic and manual probing was found in terms of the “limits of agreement” proposed by Bland and Altman. It may arise from the model used in the algorithm and further research is necessary to develop more accurate phantom and understand the physics behind the intuitive variation of the DWFP patterns.

TABLE 4.1
BLAND-ALTMAN EVALUATION OF ULTRASONIC PROBING RESULTS
(MAY 18)

a. Mean Difference \bar{d} and its 95% Confidence Intervals (May 18)

| Patient # | 1 | 2 | 3 | 4 | 5 | 6 | 7 | 8 | 9 | 10 | 11 | 12 | 13 | 14 |
|------------|-----|---------|--------|---------|--------|---------|---------|---------|---------|---------|---------|---------|---------|---------|
| \bar{d} | N/A | -0.1128 | 0.4532 | 0.1722 | 0.8217 | 0.0176 | -0.7202 | 0.2462 | 0.1853 | -0.7140 | -0.3904 | -0.0353 | -0.6021 | -1.2224 |
| Low Limit | N/A | -0.3818 | 0.1741 | -0.1305 | 0.5303 | -0.3553 | -1.0045 | -0.0501 | -0.0714 | -0.9960 | -0.7110 | -0.3243 | -0.8485 | -1.4429 |
| High Limit | N/A | 0.1563 | 0.7323 | 0.4750 | 1.1130 | 0.3905 | -0.4360 | 0.5425 | 0.4421 | -0.4320 | -0.0697 | 0.2538 | -0.3557 | -1.0019 |

b. Limits of agreement $\bar{d} \pm 2SD$ and their 95% Confidence Intervals (May 18)

| Patient # | 1 | 2 | 3 | 4 | 5 | 6 | 7 | 8 | 9 | 10 | 11 | 12 | 13 | 14 |
|-----------------|-----|---------|---------|---------|---------|---------|---------|---------|---------|---------|---------|---------|---------|---------|
| $\bar{d} + 2SD$ | N/A | 2.4094 | 3.0481 | 3.7399 | 3.8056 | 2.7541 | 2.6465 | 3.7914 | 3.2574 | 2.3447 | 3.3886 | 3.0618 | 2.3459 | 1.6769 |
| Low Limit | N/A | 1.9433 | 2.5647 | 3.2156 | 3.3009 | 2.1082 | 2.1542 | 3.2782 | 2.8127 | 1.8562 | 2.8332 | 2.5612 | 1.9191 | 1.2950 |
| High Limit | N/A | 2.8754 | 3.5315 | 4.2643 | 4.3103 | 3.3999 | 3.1388 | 4.3047 | 3.7021 | 2.8331 | 3.9440 | 3.5625 | 2.7727 | 2.0588 |
| $\bar{d} - 2SD$ | N/A | -2.6349 | -2.1417 | -3.3955 | -2.1623 | -2.7188 | -4.0869 | -3.2991 | -2.8867 | -3.7726 | -4.1693 | -3.1324 | -3.5502 | -4.1217 |
| Low Limit | N/A | -3.1010 | -2.6251 | -3.9199 | -2.6669 | -3.3647 | -4.5792 | -3.8123 | -3.3315 | -4.2611 | -4.7247 | -3.6331 | -3.9769 | -4.5036 |
| High Limit | N/A | -2.1689 | -1.6583 | -2.8712 | -1.6576 | -2.0729 | -3.5946 | -2.7858 | -2.4420 | -3.2842 | -3.6139 | -2.6317 | -3.1234 | -3.7398 |

N/A- patient not available

TABLE 4.2
BLAND-ALTMAN EVALUATION OF ULTRASONIC PROBING RESULTS
(AUGUST 17)

a. Mean Difference \bar{d} and Its 95% Confidence Intervals (August 17)

| Patient # | 1 | 2 | 3 | 4 | 5 | 6 | 7 | 8 | 9 | 10 | 11 | 12 | 13 | 14 |
|------------|---------|--------|--------|---------|---------|--------|---------|--------|--------|--------|---------|---------|--------|-----|
| \bar{d} | -0.0383 | 0.4431 | 2.1375 | 0.0154 | -0.7111 | 0.4561 | 0.1884 | 0.9767 | 0.5739 | 1.2619 | -0.0827 | 0.1696 | 1.3116 | N/A |
| Low Limit | -0.3708 | 0.2035 | 1.9106 | -0.5105 | -1.0207 | 0.2277 | -0.0732 | 0.7546 | 0.3573 | 1.0374 | -0.3309 | -0.0641 | 1.0875 | N/A |
| High Limit | 0.2941 | 0.6826 | 2.3644 | 0.5414 | -0.4015 | 0.6844 | 0.4500 | 1.1989 | 0.7905 | 1.4863 | 0.1654 | 0.4034 | 1.5356 | N/A |

b. Limits of agreement $\bar{d} \pm 2SD$ and their 95% Confidence Intervals (August 17)

| Patient # | 1 | 2 | 3 | 4 | 5 | 6 | 7 | 8 | 9 | 10 | 11 | 12 | 13 | 14 |
|-----------------|---------|---------|---------|---------|---------|---------|---------|---------|---------|---------|---------|---------|---------|-----|
| $\bar{d} + 2SD$ | 3.4348 | 2.9452 | 4.7704 | 4.0246 | 2.5230 | 3.5555 | 3.5133 | 4.2047 | 3.2903 | 4.4792 | 3.0848 | 3.0615 | 4.4338 | N/A |
| Low Limit | 2.8589 | 2.5303 | 4.3774 | 3.1137 | 1.9868 | 3.1600 | 3.0602 | 3.8200 | 2.9152 | 4.0904 | 2.6551 | 2.6567 | 4.0457 | N/A |
| High Limit | 4.0106 | 3.3601 | 5.1634 | 4.9356 | 3.0592 | 3.9510 | 3.9664 | 4.5895 | 3.6655 | 4.8679 | 3.5146 | 3.4664 | 4.8219 | N/A |
| $\bar{d} - 2SD$ | -3.5115 | -2.0591 | -0.4953 | -3.9938 | -3.9452 | -2.6434 | -3.1365 | -2.2513 | -2.1425 | -1.9554 | -3.2503 | -2.7223 | -1.8107 | N/A |
| Low Limit | -4.0873 | -2.4739 | -0.8884 | -4.9048 | -4.4814 | -3.0389 | -3.5895 | -2.6360 | -2.5176 | -2.3441 | -3.6801 | -3.1271 | -2.1988 | N/A |
| High Limit | -2.9356 | -1.6442 | -0.1023 | -3.0828 | -3.4089 | -2.2479 | -2.6834 | -1.8665 | -1.7674 | -1.5667 | -2.8206 | -2.3174 | -1.4226 | N/A |

N/A- patient not available

CHAPTER V

MULTI-MODE LAMB WAVE TOMOGRAPHY

5.1 Introduction

Lamb waves are ultrasonic guided waves that follow the curvature of the structure and allow large sections of thin-wall structures, such as airframe skins, storage tanks and pressure vessels to be quickly inspected for structural defects such as disbonds, corrosion and delaminations. However, due to the complex physics of Lamb wave propagation, it is very difficult to interpret the waveforms directly, and is generally considered to be too complicated to be useable by technicians in the field.

If Lamb wave measurements are made for a number of relative transducer positions (projections), then an image of a large region can be reconstructed tomographically to give an easily interpretable quantitative map of the parameter of interest, e.g., thickness loss due to corrosion [89]. In this case we have an inverse problem of having to reconstruct a medium from waves propagating through it: a tomographic problem [90].

Numerous Lamb wave tomography studies have been conducted to explore different measurement geometries, to increase reconstruction speed and to improve the resolution and quality of the generated image [91-95]. The most critical part of these works is to develop robust and reliable algorithms that process the Lamb waveforms

automatically to extract the information of interest. Unlike the bulk wave case where gating and peak-detection techniques are usually adequate to obtain the time of flight, with guided waves more sophisticated signal processing is required to extract the arrival times of various Lamb wave modes [89].

One important characteristic of a Lamb wave is that it can have multiple modes propagating simultaneously in the plate. However, most research on Lamb wave tomography has so far used only a single mode. Since different modes have different wave structures, for a specific defect presented in the plate, such as surface corrosion, one mode may be more sensitive than other modes. Therefore, it is of practical interest to exploit several Lamb wave modes and generate corresponding tomographic images.

In this chapter, a dynamic wavelet fingerprint based approach to estimate the arrival times of the first three Lamb wave modes and generate corresponding tomographic images is described. In Section 5.2, the fundamental theory of Lamb waves is introduced. The algorithm used to estimate the arrival times of the first three modes is presented in Section 5.3. The performance of the algorithm is evaluated in Section 5.4 by comparing the estimated values with theoretical values and by direct observation of the final tomography images. A discussion and conclusion is given in Section 5.5.

5.2 Lamb Wave Fundamentals

Theoretical analysis of Lamb wave propagation has been widely studied by Viktorov, Achenbach, Graff, Brekhovskikh, Grinchenko, Rose, Auld and others [95]. The

fundamental conclusions of Lamb wave theory can be obtained by analyzing a classical example: propagation of Lamb waves in an elastic plate with traction free boundaries. The geometry of the free plate problem is illustrated in Figure 5.1. The wave propagates parallel to the y-axis and its behavior is governed by the following equations:

$$\sigma_{ij,j} + \rho f_i = \rho \ddot{u}_i, \quad \text{Equations of motion } (i, j = 1, 2, 3); \quad (5.1)$$

$$\varepsilon_{ij} = \frac{1}{2}(u_{i,j} + u_{j,i}), \quad \text{Strain displacement equations}; \quad (5.2)$$

$$\sigma_{ij} = \lambda \varepsilon_{kk} \delta_{ij} + 2\mu \varepsilon_{ij}, \quad \text{Constitutive equations (isotropic materials)}. \quad (5.3)$$

written in index notation.

Eliminating stress and strain from these equations, we have Navier's equation:

$$\mu u_{i,jj} + (\lambda + \mu) u_{j,ji} + \rho f_i = \rho \ddot{u}_i. \quad (5.4)$$

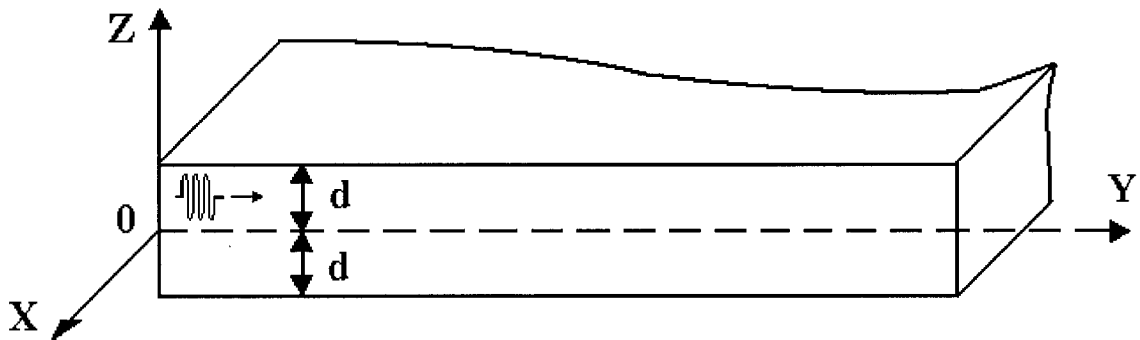


Figure 5.1 Lamb waves traveling in the Y direction in a traction free isotropic plate of thickness $2d$.

The exact solution of this problem with traction-free boundary conditions has been obtained by several different approaches. The most popular methods of solution are the displacement potentials and the partial wave techniques (see Achenbach [96] and Auld [97], respectively). All of these methods lead to the same results summarized below [95]:

1. Lamb waves are a combination of coupled horizontal and vertical motions in the yz plane.

2. There exist symmetric and antisymmetric families of Lamb waves depending on the displacement symmetry with respect to the plate centerline $z = 0$.

3. Each family has a corresponding dispersion equation (Rayleigh-Lamb frequency equations):

$$\frac{\tan(qh)}{\tan(ph)} = -\frac{4k^2 pq}{(q^2 - k^2)^2} \quad \text{for symmetric modes.} \quad (5.5)$$

$$\frac{\tan(qh)}{\tan(ph)} = -\frac{(q^2 - k^2)^2}{4k^2 pq} \quad \text{for antisymmetric modes.} \quad (5.6)$$

where k is the wavenumber and

$$p = \left(\frac{\omega}{c_L}\right)^2 - k^2, \quad q = \left(\frac{\omega}{c_T}\right)^2 - k^2.$$

4. By solving these transcendental dispersion equations (5.5) and (5.6), dispersion curves relating the phase velocity c_p to the frequency ω can be obtained. For an aluminum plate, the dispersion curves are presented in Figure 5.2.

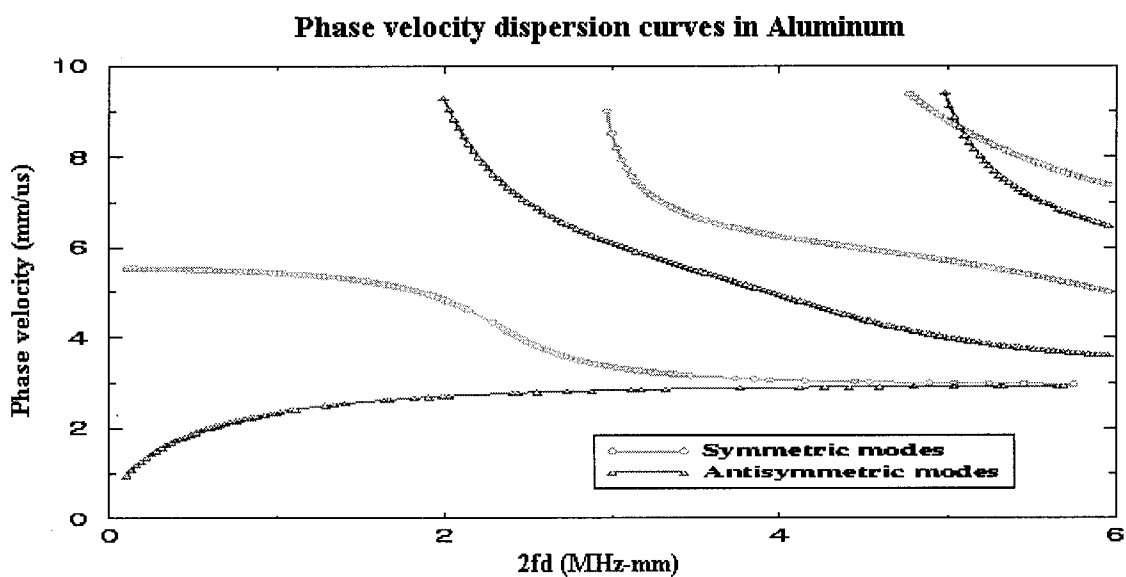


Figure 5.2 Phase velocity dispersion curves in Aluminum plates for the first three symmetric and antisymmetric modes. Phase velocity is plotted versus the product of frequency f (MHz) and plate thickness $2d$ (mm) [95].

In general, at a given frequency, there are several modes propagating in the plate, each with a different phase velocity. Symmetric modes S_n , $n = 0,1,2,\dots$ and antisymmetric modes A_n , $n = 0,1,2,\dots$ are enumerated according to the order of their cut-off frequencies. All modes except the S_0 and A_0 have such frequencies defined as:

$$\omega_{cs} = n\pi \frac{c_T}{d}; \quad \omega_{cs} = \pi(n + \frac{1}{2}) \frac{c_L^2}{c_T d} \quad \text{for symmetric modes} \quad (5.7)$$

$$\omega_{cs} = \pi(n + \frac{1}{2}) \frac{c_T}{d}; \quad \omega_{cs} = n\pi \frac{c_L^2}{c_T d} \quad \text{for antisymmetric modes} \quad (5.8)$$

where n is a positive integer.

Below the cut-off frequency, each mode represents an exponentially decaying wave, which means they are evanescent. On the other hand, the higher the frequency, the more modes will be beyond their cut-off frequency and propagate through the plate.

5. If the frequency spectrum of the disturbance is nonzero within only a narrow range, the wave packet, once blurred to a certain extent, will later preserve its shape and move as a whole with a group velocity.

In our study, Lamb waves are generated with a tone burst composed of several harmonic cycles at the carrier frequency. The envelope of the initial disturbance is roughly rectangular but after traveling some distance in the plate it generally splits into several envelopes corresponding to different modes that exist in the plate at a given frequency and propagate with group velocities corresponding to their modes. Accordingly, group velocities of various modes were measured and used for reconstruction.

Theoretically, the group velocity c_g can be obtained as

$$c_g = \frac{d\omega}{dk} = \left[c_p - \omega \frac{dc_p}{d\omega} \right]^{-1} \quad (5.9)$$

and the dispersion curve for group velocity is shown in Figure 5.3.

As can be seen in Figure 5.3, the higher the excitation (carrier) frequency, the more modes will develop and propagate through the plate. On the other hand, at a specific frequency, the group velocities of some modes change more rapidly than that of other modes. In other words, at any specific frequency, different Lamb wave modes have different sensitivity to variations of the thickness.

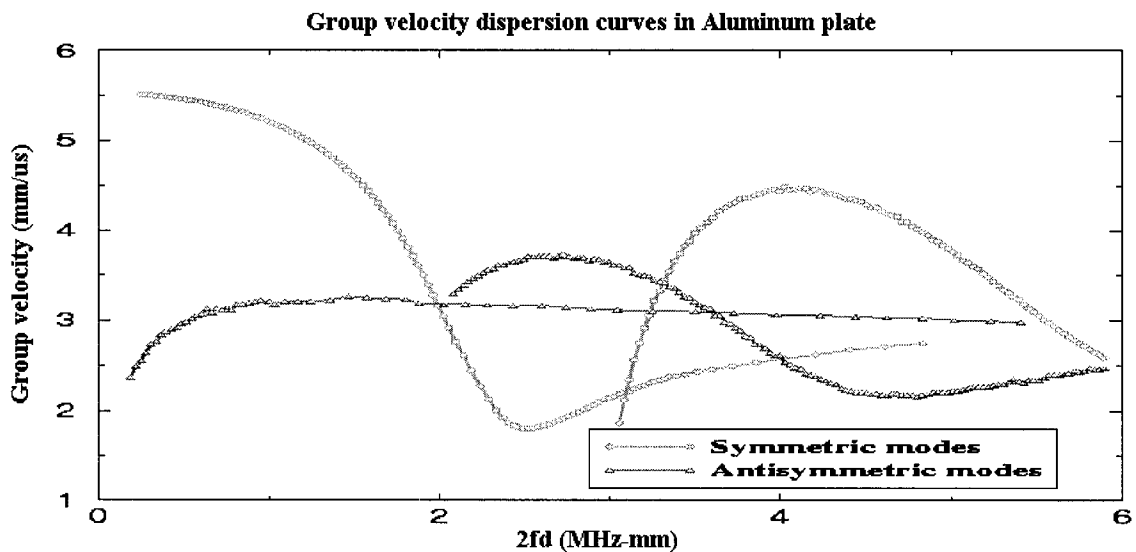


Figure 5.3 Group velocity dispersion curves in Aluminum plates for the first two symmetric and antisymmetric modes. Group velocity is plotted versus the product of frequency f (MHz) and plate thickness $2d$ (mm) [95].

5.3 Double Crosshole Tomography

There are many ways to carry out Lamb wave tomography imaging. One appropriate choice is to use double crosshole scanning geometry with the algebraic reconstruction technique [95].

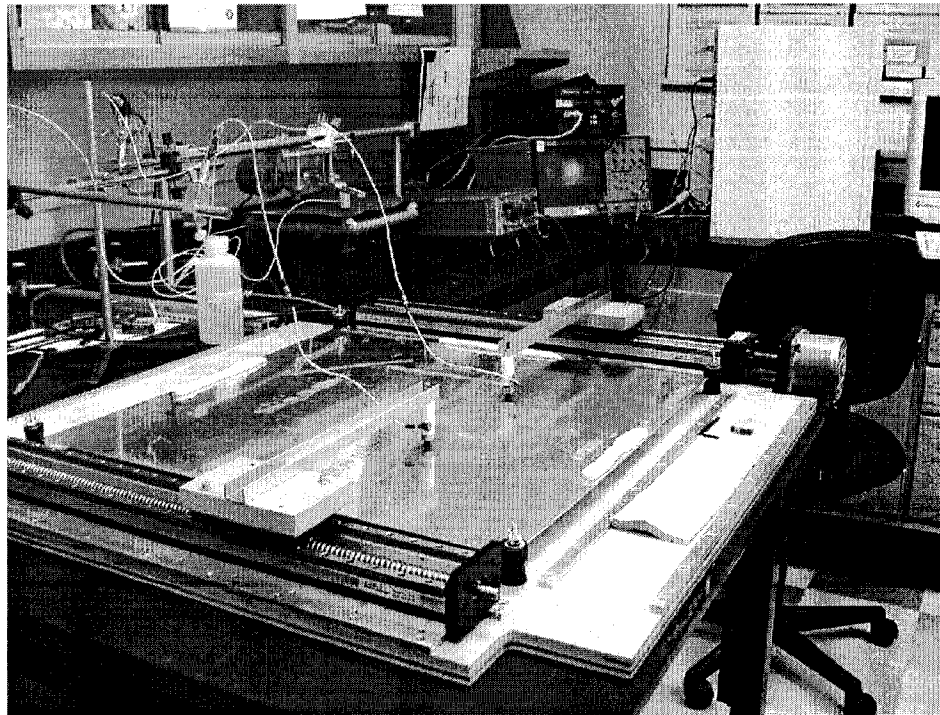


Figure 5.4 Double crosshole scanning system.

The configuration of the double crosshole scanner used in this research is shown in Figure 5.4. A pair of transducers are attached to linear slider screws and moved back and forth along two parallel sides. At any single position (from 0 to $N-1$) the transmitting transducer generates Lamb waves to propagate in the plate, and the receiving transducer sweeps all N available positions (from 0 to $N-1$) to record the transmitted Lamb waves.

After N^2 measurements, the first cross-hole projection is complete. Similarly, the second cross-hole projection is obtained by moving a pair of transducers along the other two parallel sides and collect corresponding waveforms.

As illustrated in Figure 5.5, two coordinates i, j are used to indicate a “ray” which represents the path the Lamb wave travels from the transmitter to the receiver in the plate. The square area covered by the “rays” can be divided into square cells (pixels) by making the cell size equal to the transducer step size a . Each cell in the resulting matrix has unique coordinates $m, n < [0, N)$. Each ray $[i, j]$ crosses a certain number of pixels on its way from the transmitter to the receiver.

We assume all the rays to be straight lines and the velocity of the wave to be constant for each pixel and denote it as $v[m, n]$ where m, n are that pixel’s coordinates starting from the bottom left corner. The time the wave spends crossing the pixel will then be $t[i, j; m, n] = \delta[i, j; m, n] / v[m, n]$, where $\delta[i, j; m, n]$ is the length of a segment that pixel m, n cuts from the ray $[i, j]$. The arrival time for a given ray $[i, j]$ can be estimated by summing all partial times $t[i, j; m, n]$ over the pixels involved:

$$T[i, j] = \sum_{m, n \in \text{ray}[i, j]} t[i, j; m, n] = \sum_{m, n \in \text{ray}[i, j]} \frac{\delta[i, j; m, n]}{v[m, n]} \quad (5.10)$$

This is a system of linear equations with unknown slownesses $1/v[m, n]$. We can calculate the segment length $\delta[i, j; m, n]$ theoretically and measure $T[i, j]$ experimentally. Solving the matrix equation will yield the velocity pattern of a given

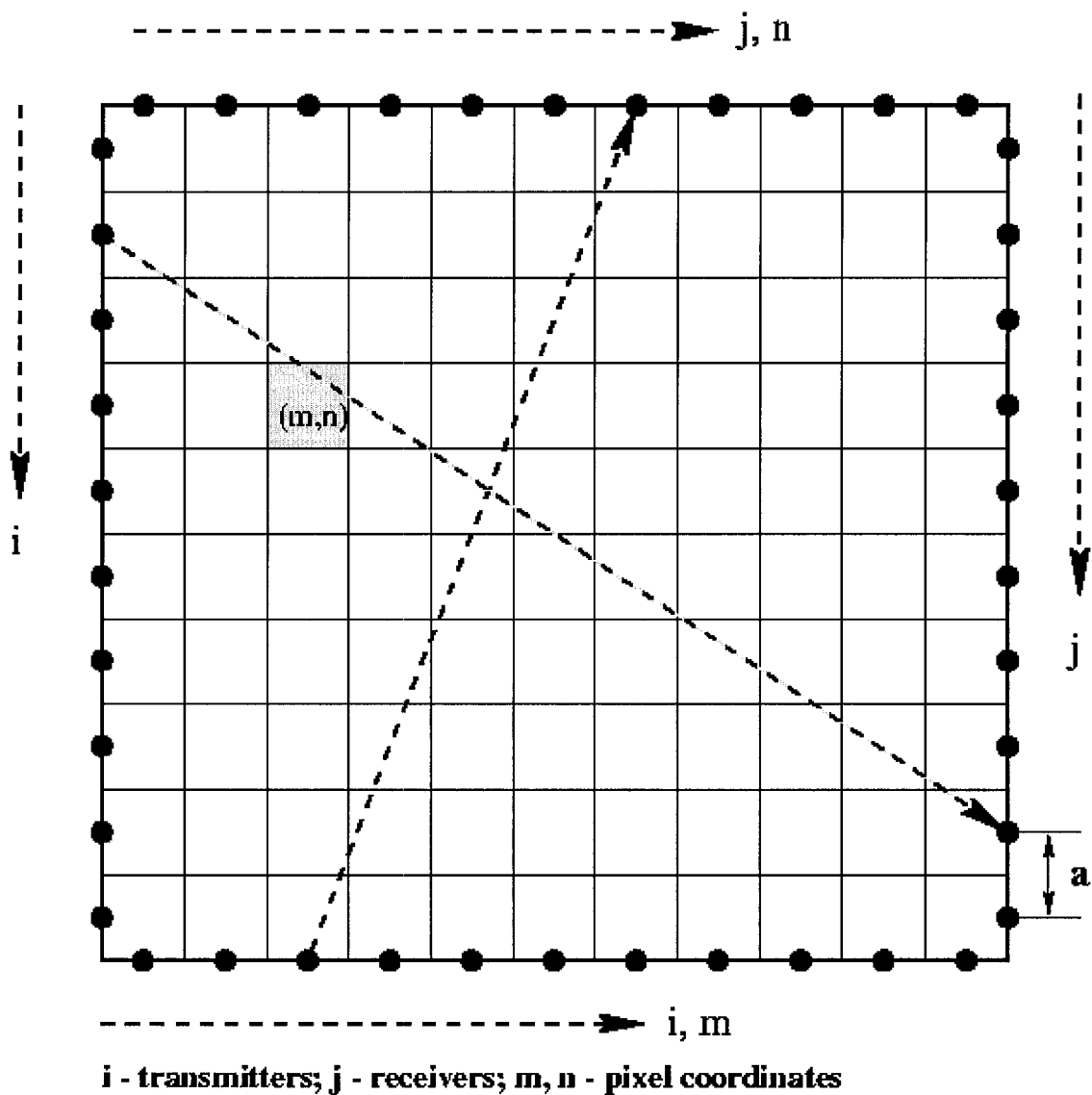


Figure 5.5 Explanation of the ART algorithm for the double crosshole geometry. a - distance between transducers; pixels (m, n) are indexed as shown; ray enumeration order (i, j) is different from different projections [95].

Lamb wave mode throughout the square region. Since the operation frequency is known, it can be transformed into a thickness map via the dispersion curves.

To solve the equations without direct inversion of a large matrix, the less computationally intensive iterative Algebraic Reconstruction Technique [98] is commonly used. When applied to double crosshole Lamb wave tomography it leads to the following sequence of operations [95]:

1. Determine the segment lengths $\delta[i, j; m, n]$, then estimate pixel velocities (an initial guess) and calculate estimated values for the arrival time of each ray:

$$T^0[i, j] = \sum_{m, n \in \text{ray}[i, j]} \frac{\delta[i, j; m, n]}{v^0[m, n]} \quad (5.11)$$

2. For each ray calculate velocity updates in the cells containing that ray:

$$\Delta \frac{1}{v_{m, n \in \text{ray}[i, j]}[m, n]} = \frac{T[i, j] - T^0[i, j]}{L[i, j]} \quad (5.12)$$

where $L[i, j]$ is the length of ray $[i, j]$ and $T[i, j]$ is the experimentally measured arrival time for ray $[i, j]$.

3. Add the update to the current slowness $1/v[m, n]$ values for that ray thus completing the first iteration:

$$\frac{1}{v^1[m, n]} = \Delta \frac{1}{v[m, n]} + \frac{1}{v^0[m, n]}; \quad m, n \in \text{ray}[i, j] \quad (5.13)$$

4. The values $v^1[m, n]$ can be used as an input for the second iteration. Steps (5.11)-(5.13) are repeated until the required accuracy is reached.

To suppress the “salt and pepper” noise frequently encountered in the ART images, instead of updating the pixel velocity immediately after each ray is used, one can first calculate the updates for all the rays and only then update all the pixel velocities simultaneously. The modified method is called Simultaneous Iterative Reconstruction Technique (SIRT) [98], which is applied here to reconstruct all following tomographic images.

5.4 Estimation of Arrival Times of Multi Lamb Modes

Accurate measurement of the arrival times of Lamb wave modes is a critical step in the tomographic imaging process since it strongly affects all subsequent steps. Several signal processing techniques have been developed in either time-domain or time-frequency domain in [95], including:

- Pattern matching technique

The basic idea is that given some signal-like pattern one can match it point by point against parts of the signal until a specified accuracy is reached. With static pattern, thoughtful design of the templates is critical. However, in tomographic experiments where thousands of rays are traveling through an unknown media, it is impossible to know *a priori* the shape of the next signal. With adaptive patterns, part of the previously processed signal can be used as a pattern to match against the current signal. However, the stability of this algorithm strongly depends on the accuracy of previous steps and the first arrival time for each measurement set has to be extracted manually. With neural

networks [99], despite their ability to partially eliminate the systematic uncertainty in the arrival times, in general, the approach investigated was unable to successfully recognize the signal (the S_0 mode) and its arrival time.

- Time-frequency analysis

A specially designed positive joint time-frequency distribution can be used to estimate the arrival time of the S_0 mode:

$$P(t, \omega) = |S(\omega)|^2 |s(t)|^2 \quad (5.14)$$

where $|s(t)|^2$ is the intensity per unit time at time t and $|S(\omega)|^2$ is the intensity per unit frequency ω . This approach is computationally efficient and capable of working in the autonomous mode for temporal localization of the first arrivals and produces results yielding satisfactory image quality after reconstruction. However, these results suffer from significant systematic errors related to the uncertainty principle.

- Time-domain search

The time domain group delay is measured as the arrival time of a chosen point on the leading edge of the S_0 mode. Although not strictly in accordance with the physical definition of group velocity, this approach demonstrated the highest accuracy and superiority to all methods implemented in [95].

- Generalized travel time method

A general travelttime estimation method for dispersive media developed by Ernst and Herman is defined as follows [90]:

$$\tau^{GT}(d, \omega) = t_{\min} - \frac{d}{d\omega} \Im \left[\log \left\{ \sum e^{-(\alpha + j\omega)(t_i - t_{\min})} \widehat{d}(t_i) \right\} \right] \quad (5.15)$$

with i such that $t_{\min} < t_i < t_{\max}$ where t_{\min} and t_{\max} denote the start and end of a time window surrounding the arrival of the direct guided wave. Here α is a real positive damping constant to avoid zeros in the complex frequency plane, \widehat{d} is a windowed and tapered version of the input time data d , and \Im stands for the imaginary part of a complex number.

A more numerically robust method can be derived by differentiating equation (5.15) and using the differentiation property of the Fourier transform (denoted by F):

$$\tau^{GT}(d, \omega) = t_{\min} + \Re \frac{F\{te^{-\alpha} d(t)\}}{F\{e^{-\alpha} d(t)\}} \quad (5.16)$$

where \Re denotes the real part of a complex number. Using an adapted version of (5.16), high overall quality of the travel time of the S_0 mode was obtained, even though there is rather large mean square error compared with theoretical ones.

Unfortunately, all of the above methods only deal with a single mode: the fastest symmetric mode S_0 . When multiple modes need to be considered, it becomes more complex and difficult to extract the travel time of each mode due to following factors:

- Unlike the fastest symmetric mode S_0 which usually has significantly large amplitude to be easily identified, other Lamb wave modes are generally of moderate or even weak amplitude.

- Lamb waves are inherently dispersive, i.e., different frequency components propagate at different speeds in a wave-packet, which causes wave-packets to spread out in space and time when they propagate through a structure [100]. Due to the continuously evolved shape (increased duration and reduced amplitude) and signal overlapping of wave-packets, many of the techniques mentioned above, such as time domain searching, static pattern matching, global time-frequency analysis, are either invalid or lack sufficient accuracy.
- In the presence of discontinuities such as corrosion and damage, mode conversion may occur at the discontinuity [86]. This may generate coherent interferences (false peaks) in the waveform. In that case, the generalized travel time method may produce misleading results.
- Scanner vibration and imperfect coupling may introduce random noise in the waveform.

Accordingly, to accurately estimate the arrival time of each Lamb mode, it is necessary to develop a robust detection technique to overcome the difficulty caused by the non-stationary property of the Lamb waveform. At the same time, it is also necessary to apply an efficient characterization method to differentiate different Lamb modes as well as coherent interferences.

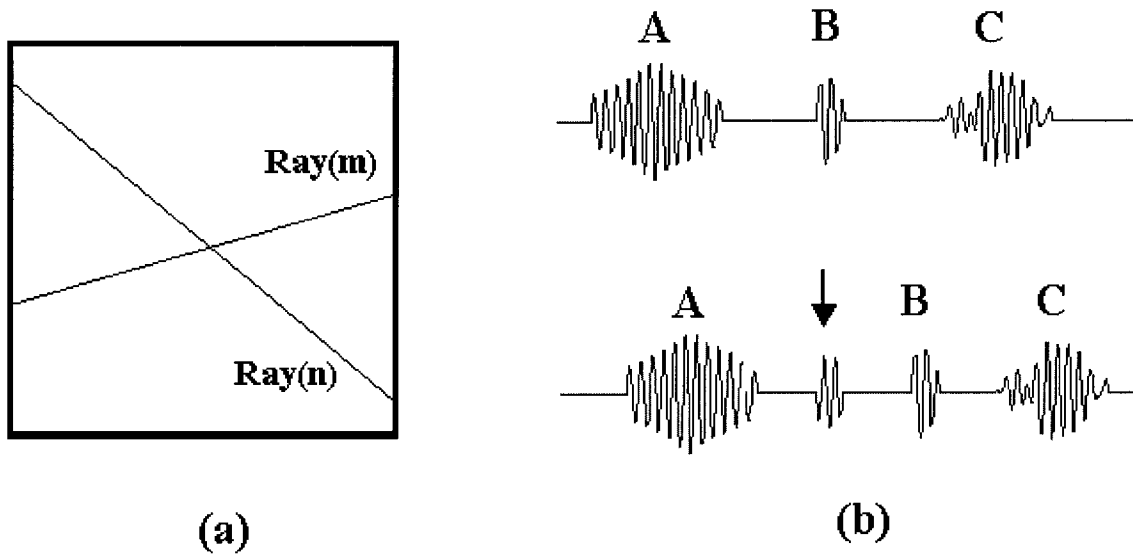


Figure 5.6 Demonstration of the arrival sequence of three Lamb wave modes. (a) Two arbitrary rays. (b) The arrival sequence of the three modes remains unchanged, although there may be interferences indicated by the black arrow in between.

Despite the complex mechanism of Lamb wave propagation, it was found that the arrival sequence of the first several modes generally remains unchanged, i.e., the fastest mode always arrives in the first place in different “rays”, the second fastest mode always arrives in the second place in different “rays”, and so on. As a result, different modes can be distinguished naturally by their arrival sequence. However, due to mode conversion and edge reflections, there may be interference that arrives in between, see Figure 5.6. The problem is then simplified as to detect the arrival times of the first several suspect modes (including possible interference) followed by identifying the interference and differentiating it from the real modes.

To this end, a dynamic wavelet fingerprint based algorithm is adapted to solve this detection and identification problem, which is summarized in Table 5.1 and illustrated in Figure 5.7.

TABLE 5.1
MULTI-MODES TRAVELTIME MEASUREMENT
BASED ON THE DWFP TECHNIQUE

1. Perform continuous wavelet transform of the original signal
2. Calculate the scale-averaged wavelet power (SAP)
3. Extract the envelope of the SAP
4. Find peaks in the envelope of SAP
5. Generate dynamic wavelet fingerprints at each peak location
6. Extract the feature of each dynamic wavelet fingerprint
7. Differentiate real modes from interference.

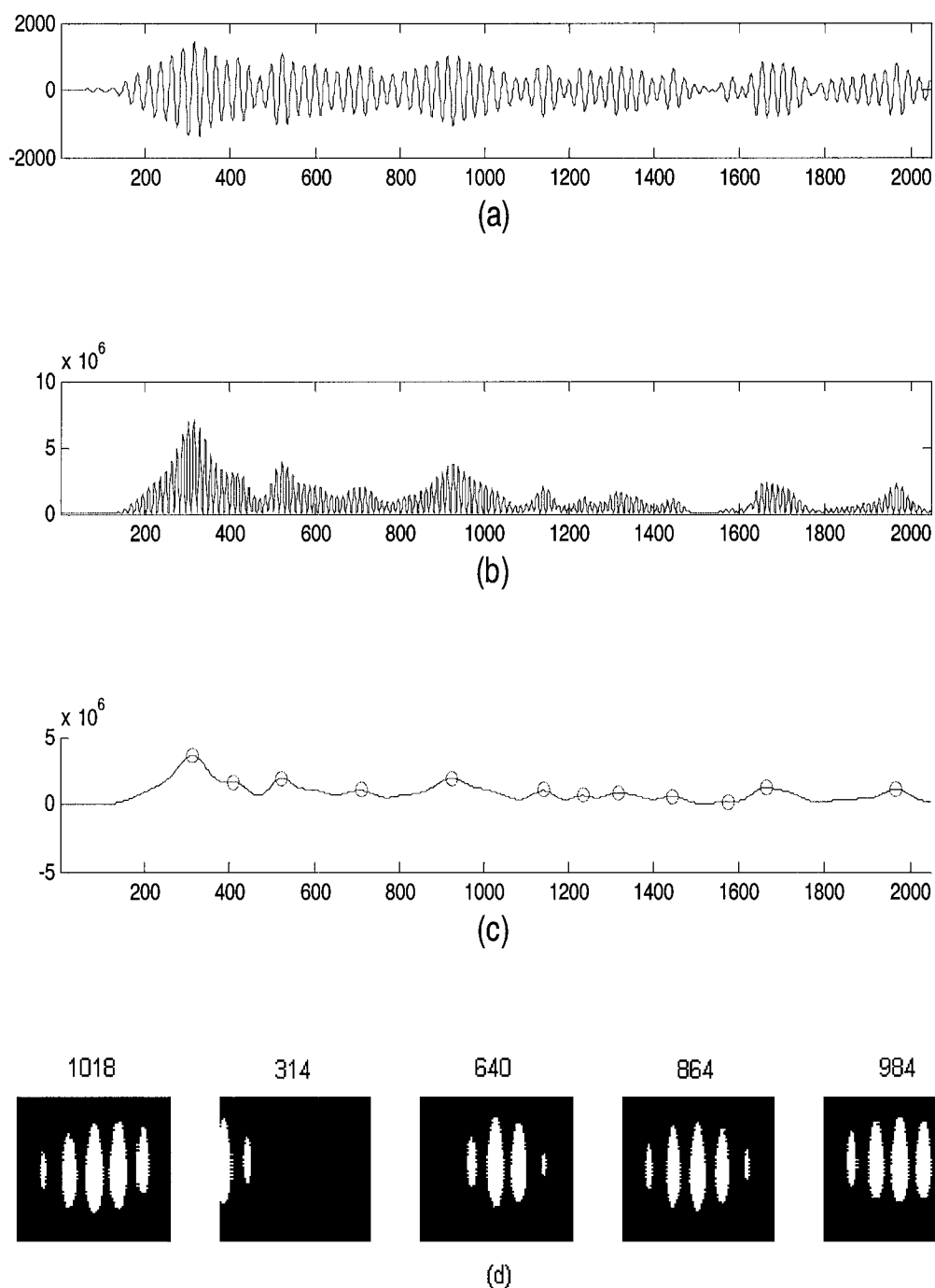


Figure 5.7 Illustration of the DWFP based algorithm to measure the arrival times of the multiple Lamb wave modes. (a) Original waveform. (b) Scale-averaged wavelet power (SAP). (c) Envelope of the SAP. Detected peaks are indicated by small circles. (d) DWFP patterns at the first five peak locations. The number on top of each pattern is the area of the white region in the pattern. Note the second pattern has significant smaller white area.

Since Lamb wave packets can be treated as Gaussian envelop carried by the excited frequency, the Morlet wavelet is used to perform the continuous wavelet transform:

$$W(s_j, n) = \frac{1}{\sqrt{s_j}} \int_{-\infty}^{\infty} x(t) \psi_0^* \left(\frac{t-n}{s_j} \right) dt, \quad j=1,2,\dots,64 \quad (5.17)$$

where $x(t)$ is the signal to be analyzed; s_j is the scale level; n is the time; ψ_0 is the mother wavelet; and * denotes conjugate.

Next, the scale-averaged wavelet power (SAP) was calculated:

$$W_a^2(n) = \frac{1}{64} \sum_{j=1}^{64} |W(s_j, n)|^2, \quad j=1,2,\dots,64 \quad (5.18)$$

According to Rose [101], group velocity is the velocity of energy transportation. For each Lamb wave mode, its energy is contained in the corresponding wave packet and travels at a corresponding group velocity. Based on the definition of group velocity, it would search for the delay of a center of gravity of the wave packet envelope. In this study, however, the peak of the envelope of the SAP curve is used as an alternative to track the movement of the wave packet.

To extract the envelope of the SAP curve, a pruning procedure [11] based on the stationary discrete wavelet transform [32] was applied to remove high frequency contents, i.e.,

$$W_s(a, b) = 0 \quad \text{for } a = 1 \dots 5 \quad (5.19)$$

where $W_s(a, b)$ is the stationary discrete wavelet coefficients at scale a and time b . Then the suspect Lamb modes were detected as the peaks of the envelop, see Figure 5.7(c).

To identify real Lamb modes from all the candidate modes, the dynamic wavelet fingerprint was generated at each peak location by using the complex Gaussian wavelet of order two. At first, it was expected that each real mode would have a distinct dynamic wavelet fingerprint in order to be identified uniquely. It turned out that such a goal was impractical due to the significant variation of the dynamic wavelet fingerprint from one ray to another. This was because the sample under test generally had irregular defects inside so that ultrasound could undergo quite different modulation from ray to ray. Therefore, instead of identifying each mode by watching its dynamic wavelet fingerprint, it was decided to use the dynamic wavelet fingerprint to differentiate interference from real modes and the remaining true modes are naturally sorted by their arrival order.

As illustrated in Figure 5.7(d), it was found that the patterns corresponding to real Lamb wave modes have significantly larger white areas than those corresponding to the interference. Accordingly, the amount of white area of the dynamic wavelet fingerprint was chosen as its feature and used to distinguish interference from real Lamb modes.

In this study, only the first three modes were considered. An empirically determined threshold of 500 was used to classify each suspect mode into either a real mode or interference.

5.5 Experimental Results

To evaluate the performance of the proposed algorithm, waveforms collected from four aluminum plates were processed to estimate the arrival times of the first three

modes. Corresponding double crosshole Lamb wave tomographic images were generated and are illustrated later. The four plates used in this study are listed below [102]:

- Plate #1: Flat bottom hole 2.2-inch diameter, 50% thickness loss.
- Plate #5: 2-inch dished-out circle flat on the bottom with max 60% thickness loss.
- Plate #6: Rectangular thinned region 1"x2" with rounded corners. 10% thickness loss.
- Plate #15: Plate with no flaws.

For each plate, total of 20000 waveforms resulting from all possible transmitter-receiver positions were recorded. The carrier frequency used was 0.99 MHz. The transducer step size was 2 mm. The shortest distance between transmitter and receiver lines was 200 mm.

For the defect-free plate #15, the experimentally estimated arrival times of the first three modes are shown in Figure 5.8. For comparison, the theoretical arrival times of the first three modes are shown in Figure 5.9. Visual inspection reveals that the estimated arrival times of the first mode (A1) are distributed rather smoothly and agree very well with theoretical values. The estimated arrival times of the second mode (A0) and the third mode (S0) are more noisy, however, the overall agreement with theoretical values is still acceptable.

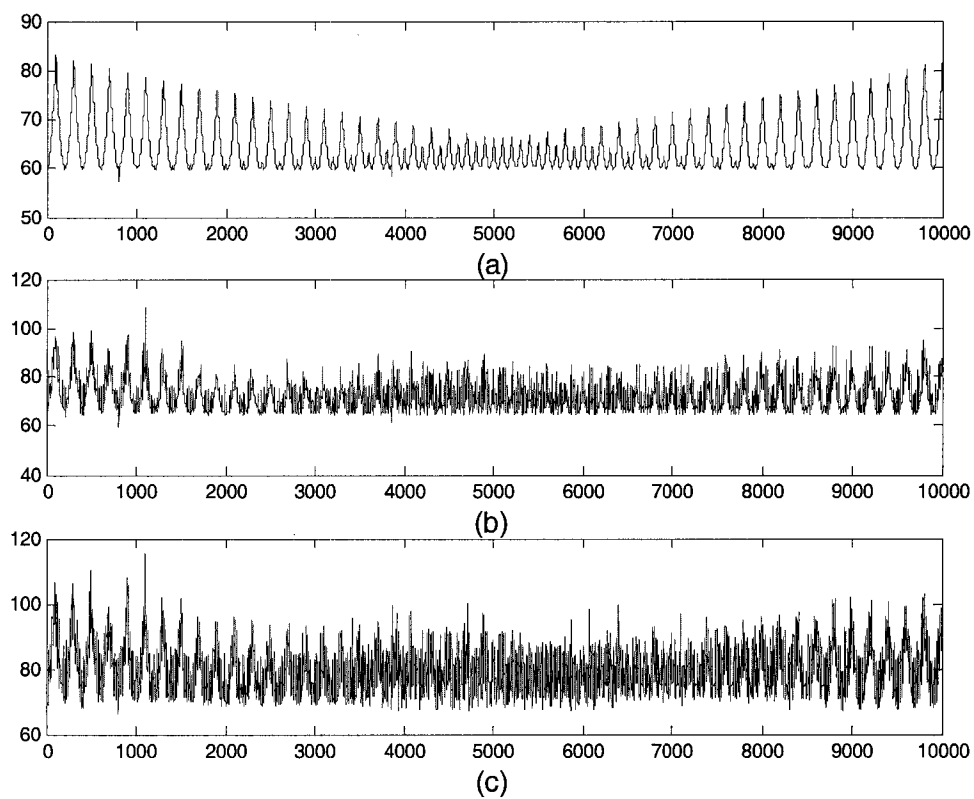


Figure 5.8 Experimentally estimated arrival times of the first three modes in a defect-free aluminum plate. (a) A1 mode. (b) A0 mode. (c) S0 mode.

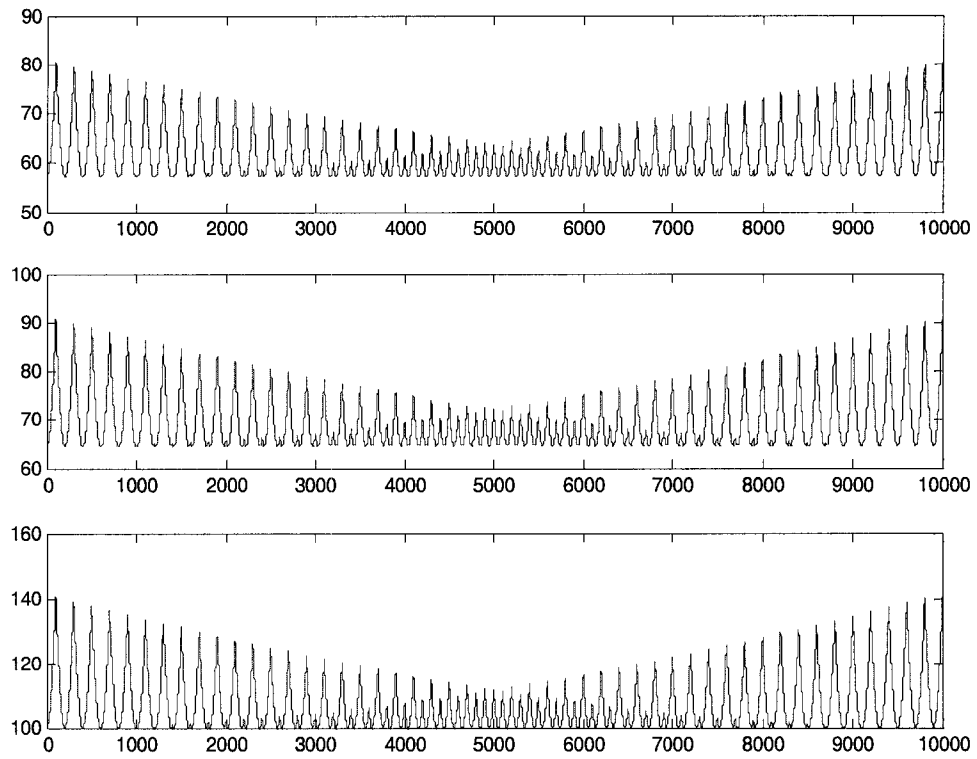


Figure 5.9 Theoretical arrival times of the first three modes in a defect-free aluminum plate. (a) A1 mode. $v = 3500 \text{ m/s}$. (b) A0 mode. $v = 3100 \text{ m/s}$. (c) S0 mode. $v = 2000 \text{ m/s}$.

Quantitatively, we computed mean square errors between 10000-point sequences of experimental and theoretical arrival times:

$$\delta = \frac{1}{N} \sum_{i=0}^{N-1} (E_i - T_i)^2 \quad (5.20)$$

where E_i and T_i is the experimental and theoretical arrival time of “ray” i . It gives an MS-error of 0.43, 4.23 and 6.29 for the A1, A0 and S0 mode respectively.

For plate #1, which has a 2.2 –inch flat bottom hole in the center, the experimental arrival times of the first three modes were shown in Figure 5.10. For the A1 mode, the distribution of the arrival times is smooth and regular. For modes A0 and S0, although the regular change of the time of flight is still quite obvious, the distribution is more noisy.

At 0.99 MHz, the flat bottom hole should cause A1 and A0 to speed up and S0 to slow down. For the A1 mode, visual inspection reveals the presence of a thinning defect in the middle of the scanned area. This shows up as a relative speeding up in the central part of the lower boundary of the arrival times of A1 mode. However, these patterns are not obvious in Figure 5.10 (b) and (c) for modes A0 and S0. One explanation is the diffraction effect at the discontinuity, which may extend the travel path of ultrasound. On the other hand, the simple threshold method used to differentiate real modes from interference may not be robust enough to handle distorted waveforms due to the discontinuity.

For plate #5, which has a 2-inch dished-out flat bottom circle with max 60% thickness loss, the experimental arrival times of the first three modes were shown in

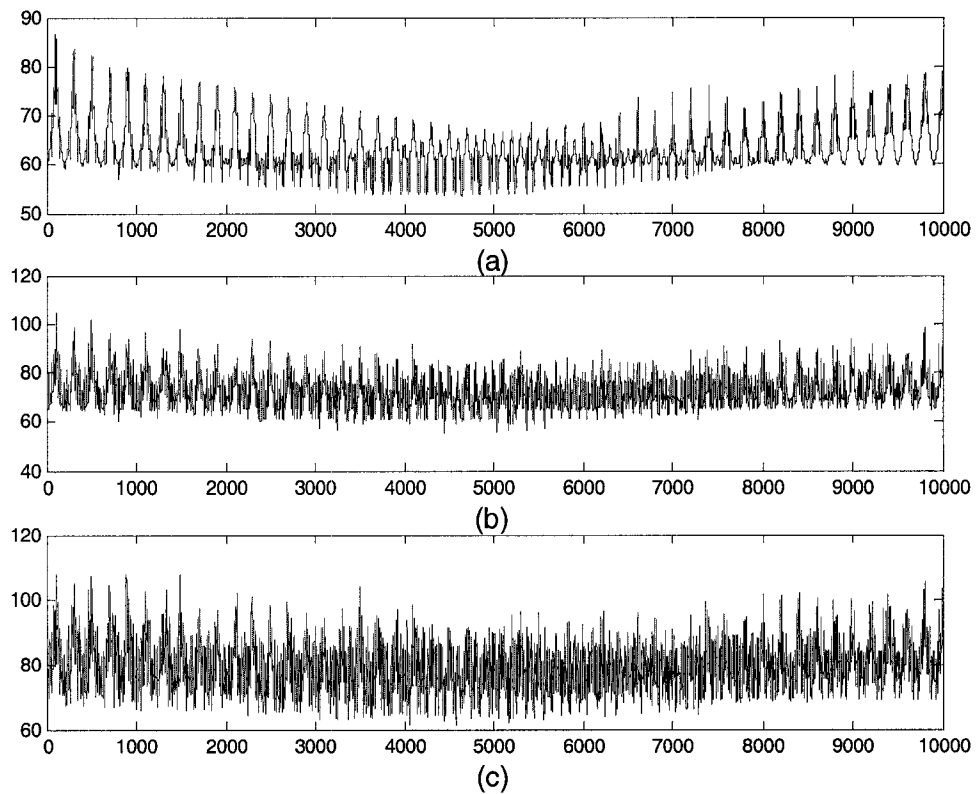


Figure 5.10 Experimentally estimated arrival times of the first three modes in an aluminum plate with a 2.2 –inch flat bottom hole in the center. (a) A1 mode. (b) A0 mode. (c) S0 mode.

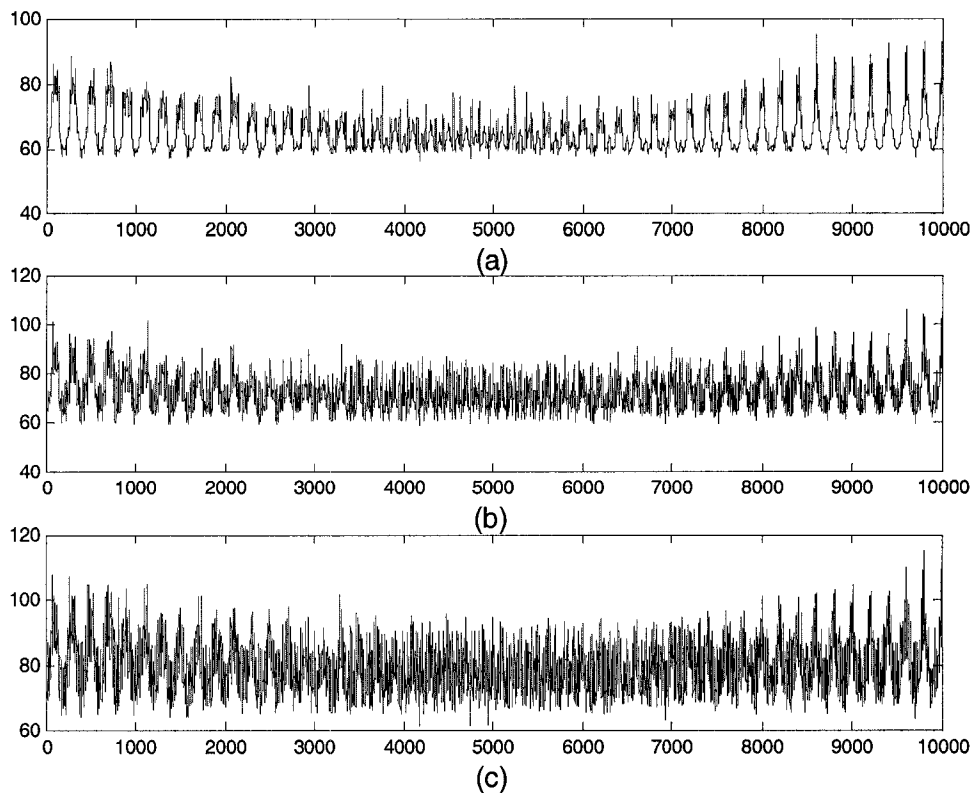


Figure 5.11 Experimentally estimated arrival times of the first three modes in an aluminum plate with a 2-inch dished out flat bottom circle with max 60% thickness loss. (a) A1 mode. (b) A0 mode. (c) S0 mode.

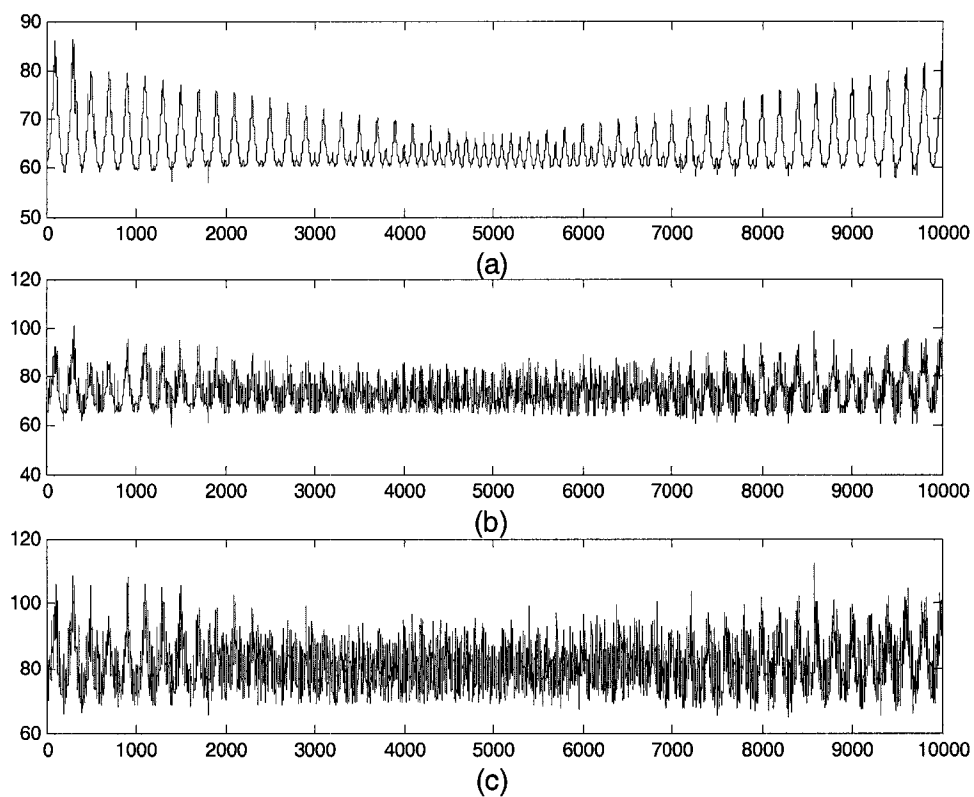


Figure 5.12 Experimentally estimated arrival times of the first three modes in an aluminum plate with a 1"x2" rectangular thinned region with rounded corners. (a) A1 mode. (b) A0 mode. (c) S0 mode.

Figure 5.11. The overall distribution of the arrival times of A1 mode is smooth and regular. However, the sharp peaks of the arrival times now become “fork-like”, which may be due to the more irregular shape of the dished-out circle. The slow down pattern in the central part of the upper boundary of the arrival times of A1 mode may be due to the diffraction effect of the dished-out circle. For modes A0 and S0, the distribution is more noisy and the speed change pattern is not clear for the same reason mentioned above.

For plate #6, which has a 1”x2” rectangular thinned region with rounded corners, the experimental arrival times of the first three modes were shown in Figure 5.12. Again, the overall distribution of the arrival times of the A1 mode is smooth and regular while those for modes A0 and S0 are more noisy. The speed change pattern is not obvious for all three modes in this case. This may be in part due to the mild extent of discontinuity (10% thickness loss).

Since the ultimate goal of this project is to generate accurate quantitative tomography which precisely maps out any defects in plate structures, it is reasonable to reconstruct tomographic images from these experimental arrivals times and use them to evaluate the performance of the proposed algorithm. Figures 5.13 – 5.16 are the reconstructed images for plates 15, 1, 5 and 6 respectively.

For plate # 15, which is defect free, the reconstructed tomographic images of the three modes are generally uniform, especially for mode A1. For plate #1, the flat bottom

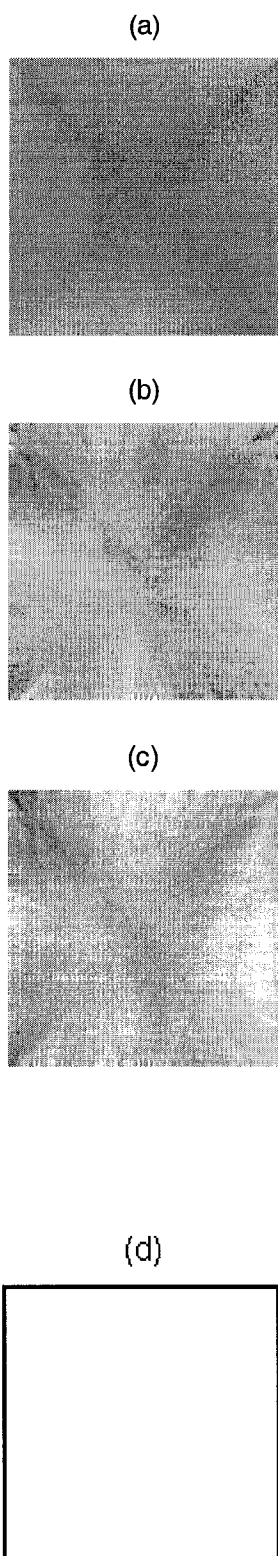


Figure 5.13 Plate #15 – SIRT reconstruction of defect free aluminum plate. Image size: 200 x 200 mm. (a) A1 mode. (b) A0 mode. (c) S0 mode. (d) Cartoon of the plate.

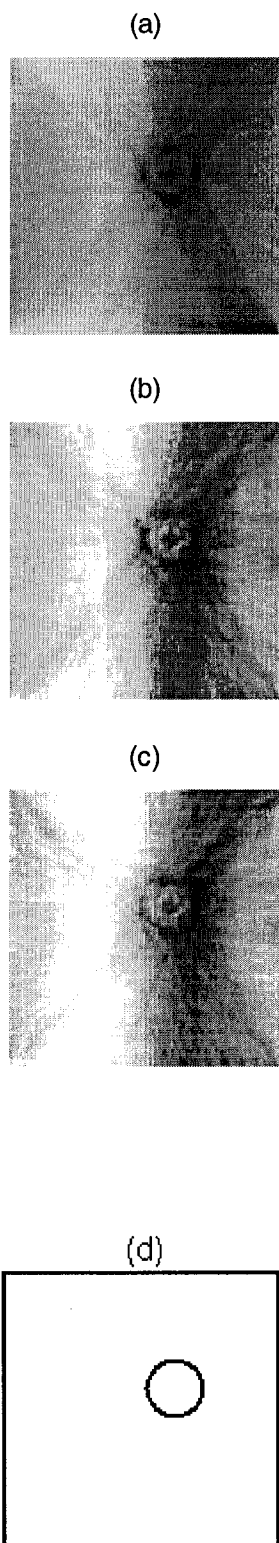


Figure 5.14 Plate #1 - SIRT reconstruction of a flat bottom hole 2.2-inch diameter, 50% thickness loss. Image size: 200 x 200 mm. (a) A1 mode. (b) A0 mode. (c) S0 mode. (d) Cartoon of the plate.

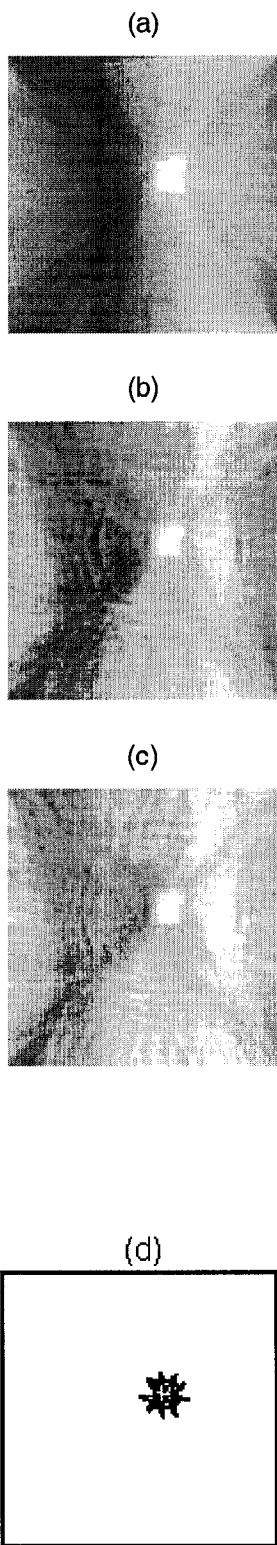


Figure 5.15 Plate #5 - SIRT reconstruction a 2-inch dished out flat bottom circle with max 60% thickness loss. Image size: 200 x 200 mm. (a) A1 mode. (b) A0 mode. (c) S0 mode. (d) Cartoon of the plate.

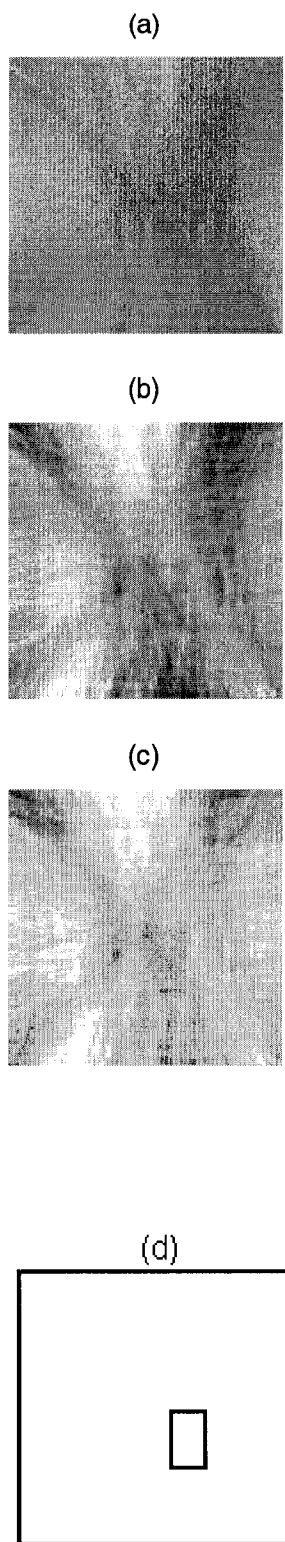


Figure 5.16 Plate #6- SIRT reconstruction a rectangular thinned region 1"x2" with rounded corners. Image size: 200 x 200 mm. (a) A1 mode. (b) A0 mode. (c) S0 mode. (d) Cartoon of the plate.

hole can be seen resolved in the reconstructed tomographic images of the three modes. For plate #5, the irregular bright spots in the center of the reconstructed tomographic images indicates the dished-out circle defect. For plate #6, the two long edges of the rectangular thinning can be seen clearly from the tomographic image of mode A1, while the overall rectangular shape of the defect can be seen more clearly from the tomographic images of modes A0 and S0. In conclusion, the spatial resolution of all reconstructed images is good enough to ensure visual detection of all the defects studied.

5.6 Conclusions

This chapter presents the application of the dynamic wavelet fingerprint technique to estimating arrival times of multiple Lamb wave modes. Although the mechanism behind Lamb wave propagation is quite complex, which makes the waveform difficult to interpret, the application of the dynamic wavelet fingerprint technique leads to automatic detection of multiple Lamb wave modes in a systematic way. The characterization step then helps to remove interference and improve the detection robustness.

Instead of using moment invariants as features, by directly watching the dynamic wavelet fingerprints, only a simple feature – the amount of white area in the fingerprint – was extracted to differentiate interference from real modes. In general, smooth distribution of arrival times was obtained for the first mode (A1), which validates the merit of this simple feature. However, for the second and third mode, the distribution of their arrival times is more noisy. Physically it may be due to the diffraction effects at the defect and the geometry of the plate. On the other hand, it may indicate that the simple

feature used is not robust enough to handle complex situations. Instead, a set of features or a dictionary of characteristic dynamic wavelet fingerprints should be exploited to recognize different modes and interference.

Acceptable tomographic images were reconstructed from the estimated arrival times of the three Lamb wave modes. The spatial resolution of all reconstructed images is good enough to ensure visual detection of all the defects studied. It demonstrates the feasibility of the dynamic wavelet fingerprint based algorithm to estimate arrival times of multiple Lamb wave modes. To optimize the performance of the suggested algorithm, it is necessary to choose carefully the experimental parameters, such as frequency, duration of the wave packet, etc., so that multiple modes are more separated in time or more differentiable in terms of their dynamic wavelet fingerprints.

CHAPTER VI

ULTRASONIC INSPECTION OF THIN MULTILAYERS

6.1 Introduction

Multilayer structures play important roles in many engineering applications such as aerospace, automotive and microelectronics. The quality and reliability of these structures are strongly dependent on the integrity of the interfaces between different layers. Because ultrasonic waves are reflected or scattered by discontinuities in acoustic impedance, they are very sensitive to defects such as cracks and delaminations at the interfaces of multilayers. Therefore ultrasonic-based techniques are widely used to inspect these multilayer structures [103-106].

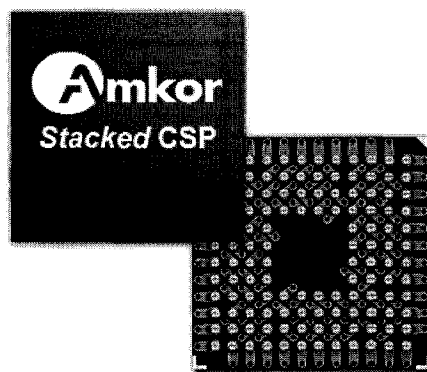


Figure 6.1 Typical stacked chip scale packages. Multiple dies are stacked in one package.

However, with the rapid development of materials science and packaging technology, the thickness of these layers has been reduced significantly. In microelectronic devices, for example, it begins to see packages with four to six dies stacked together with each die only 100-200 μm thick. Such extremely thin multilayer structures are becoming a serious challenge to current ultrasonic inspection techniques. On one hand, it is necessary to use much higher frequency to achieve high resolution (both longitudinal and lateral); on the other hand, there is a limit to the highest frequency that can be used for a particular application. This limit is due to several factors such as [107]:

- narrowness of the spike generated by the ultrasonic pulser,
- bandwidth of the ultrasonic receiver,
- frequency response of the transducer,

and more importantly,

- material propagation properties, such as strong attenuation for higher frequencies that can limit the frequency content of the ultrasonic signal.

Even after overcoming these limitations, the ultrasonic waveforms reflected from these thin multilayer structures can be very complicated due to overlapping echoes. Furthermore, other difficulties arise in the case of similar acoustic impedances involving a weak amplitude of reflected echoes and hence low signal to noise ratio (SNR). In order to detect and locate potential defects at each interface, specific treatment of the ultrasonic waveform with advanced signal processing algorithms is required.

Classical methods implemented in current ultrasonic inspection systems include peak detection and thresholding techniques, which use one or several electronic “gates” to extract sufficiently strong transients as suspect defects. Although simple and fast, this is not stable in noisy situations and cannot deal with partially overlapped signals. On the other hand, time or frequency domain methods based on stationary rules (cross-correlation, logarithmic power spectrum, cepstrum analysis, ...) have been developed but they can fail in the representation of ultrasonic signals containing successive echoes close in time added to a lower SNR [108]. Because of the non-stationary property of these signals, time-frequency analysis has turned out to be more successful than the previous technique. However, due to the constant resolution of traditional time-frequency representations (Short time Fourier transform, Wigner-Ville, Gabor), a number of ambiguous echo detections may occur in the case of partially overlapped echoes. Better performance can be achieved by using a wavelet transform. Due to their flexible time-frequency resolution, wavelet transforms perform better than other time-frequency representations in analyzing ultrasonic signals in the presence both of low SNR and partially overlapped echoes [109,110].

A digital signal processing method, based on the continuous wavelet transform, is proposed in [109,110] for automatically detecting and measuring the time-of-flight between ultrasonic echoes. It makes use of the properties of the continuous wavelet transform modulus maxima to discriminate the signal from noise. The continuous wavelet transform modulus shows local maxima in correspondence with signal discontinuities introduced either by real echoes or random noise. All local maxima points obtained for different frequencies can be connected to form a chain. The chain due to an actual echo

presents a trend with frequency different from that of the chain due to random noise. It is thus possible to retain those chains related to actual echoes and remove most of the noise chains. Some noise chains survive this reduction (because their trend is similar to that of chains related to actual echoes), so a preliminary calibration phase is required to choose a suitable threshold level to remove them. Unfortunately, this threshold level depends on the specific application and adopted hardware, also, the preliminary calibration phase may be time consuming and need experienced operators.

Another promising ultrasonic signal processing method for multilayer structures is model based estimation [107,111-114] where the ultrasonic signals are modeled as a superposition of a series of Gaussian shaped echo wavelets with unknown parameters. Based on prior knowledge of the spectral characteristics of the ultrasonic transducer, the Maximum A Posteriori (MAP) estimation technique can be used to estimate these unknown parameters for a single echo. Coupled with the space-alternating generalized expectation-maximization algorithm (SAGE) [115], the multi-echo estimation problem can be transformed into a series of one-echo estimation problems and thus achieve computational flexibility and efficiency. However, prior knowledge of the spectral characteristics of the specific ultrasonic transducer makes this approach case dependent. More importantly, for most practical nondestructive evaluation applications, it is impossible to know in advance the number of layers in the sample due to the varying defects one is inspecting for.

In this chapter, a pattern-based auto-detection technique is presented. The basic idea is to generate simplified and intuitive two-dimensional time-scale patterns (the dynamic wavelet fingerprint, or DWFP) to characterize local signals. It is expected that a

true echo will have a distinctive time-scale pattern that can be differentiated from that of noise and interference. Because of its two-dimensional nature, a pattern is intuitive to be recognized and less sensitive to noise. Furthermore, as a knowledge-based approach, the algorithm can be customized for specific application and its performance can be improved by learning.

This chapter is organized as follows. As a proof of concept study, in Section 6.2, simulated ultrasonic signals are used to explore the existence and property of the distinctive time-scale patterns of real echoes. An automated transient detection algorithm is then developed in Section 6.3 with the knowledge from such patterns. In Section 6.4, the feasibility and performance of the algorithm is evaluated by automatically processing simulated ultrasonic signals under various conditions. A practical application of the proposed technique is demonstrated to generate a B-Scan interface map of a plastic IC package. A discussion and conclusion is given in Section 6.5.

6.2 Simulated Ultrasonic Signals

The ultrasonic signal model used in this chapter is:

$$x(t) = \sum_{i=1}^m A_i s(t - \tau_i) + n(t) \quad (6.1)$$

where $s(t)$ is a transient echo modeled by [116]

$$s(t) = \left(\frac{t}{3\alpha}\right)^3 \sin(2\pi f_0 t) e^{\left(3-\frac{t}{\alpha}\right)} \quad (6.2)$$

The center frequency f_0 is set as 15 MHz and the sampling frequency is set as 1 GHz. The parameter α is set to make the shape of the simulated signal similar to that of a real ultrasonic signal. Other parameters include A_i the amplitude of each echo, $n(t)$ the zero-mean uniform noise and τ_i the time delay between each pair of echoes. The duration of each echo is set as 128 ns (128 sample points).

6.3 The Distinctive Time-Scale Pattern

Time-Frequency Representations (TFRs) have been recognized as an effective approach to analyze ultrasonic echoes in critical conditions (low SNR, partial echo overlap). The success of these methods is largely due to the fact that coherent echoes have different time-frequency representations from those of random noise, which can be exploited to reject noise and other interference.

Many detection methods make use of the coefficients of the TFRs directly, e.g., finding the local maximum of the coefficients. Unfortunately, the two-dimensional property of the TFR is then largely ignored. To fully exploit the two-dimensional potential of TFRs, a pattern-based approach seems more suitable. The dynamic wavelet fingerprint (DWFP) technique developed in Chapter III can be used to generate simplified and intuitive two-dimensional time-scale patterns to characterize transient signals. It is expected that true echoes should have distinctive DWFPs that can be differentiated from that of random noise.

For ultrasonic inspection of thin multilayers, the received ultrasonic waveform is generally composed of narrowly spaced or partially overlapped echoes. To achieve high-resolution and avoid missing detected echoes, the DWFP is generated at every sample point instead of at the scale-averaged wavelet power (SAP) peaks as carried out in the previous chapters. For other details about how to generate a DWFP, please refer to Chapter III.

To identify the distinctive DWFPs corresponding to real echoes, simulated two-echo signals using (6.1) and (6.2) were first analyzed to explore the existence and properties of such distinctive patterns under different conditions as below:

$$A_1=A_2= 1 \text{ V};$$

$$\tau_1 = 0 \text{ ns}, \tau_2 \in \{50, 80, 100, 120, 160\} \text{ ns};$$

$$\text{SNR: } \infty, 24, 18, 12, 6, 0 \text{ dB.}$$

Here the SNR is defined as $20\log_{10}(A_i/A_n)$, where A_i and A_n represent the peak amplitudes of each real echo and uniform noise respectively.

One simulated ultrasonic waveform is shown in Figure 6.2. The corresponding DWFP sequence shown in Figure 6.3 was produced by generating a DWFP at each sample point. Here, the Mexican hat wavelet:

$$\psi(x) = \left(\frac{2}{\sqrt{3}} \pi^{-1/4} \right) (1-x^2)e^{-x^2/2} \quad (6.3)$$

was used with a window of 11 ns to generate the DWFP. It can be seen that the DWFP of the true echo has a well-developed circle inside. Similar observations obtained for other cases are shown in Table 6.1.

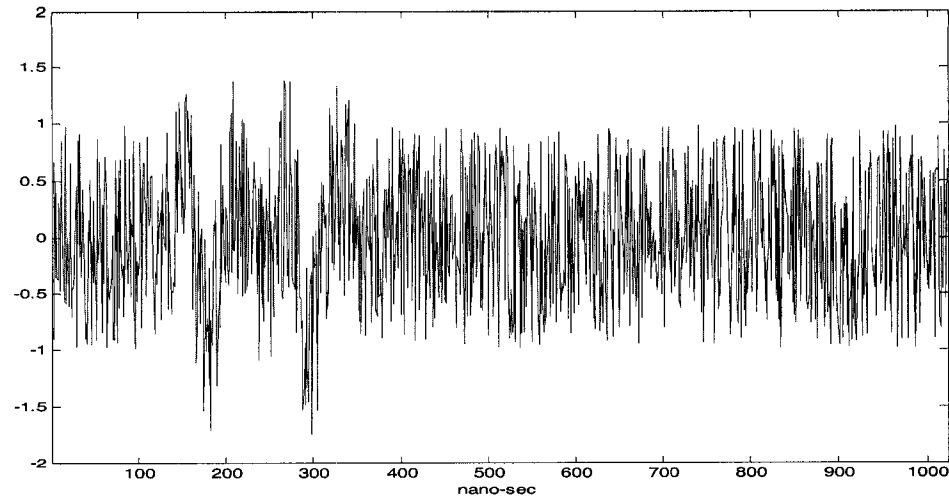


Figure 6.2 Two echoes corrupted by uniform noise. The first echo is at 177 ns , the second echo is at 297 ns , $\tau = 120 \text{ ns}$, $\text{SNR} = 0 \text{ dB}$.

Based on the analysis of these patterns, a brief summary is given below:

- In high SNR cases, the DWFPs are smooth and clean; in low SNR cases, the DWFPs become noisy. However, the basic patterns remain stable and recognizable. In other words, the distinctive pattern is not sensitive to noise.
- For widely spaced echoes, the DWFPs have a well developed circle inside; for narrowly spaced or partially overlapped echoes (e.g., when the spacing is less than 80 ns), the DWFPs have a distorted circle inside.

Thus for the simulated ultrasonic signals, the distinctive pattern corresponding to a true echo was found as a DWFP with a well-developed circle inside.

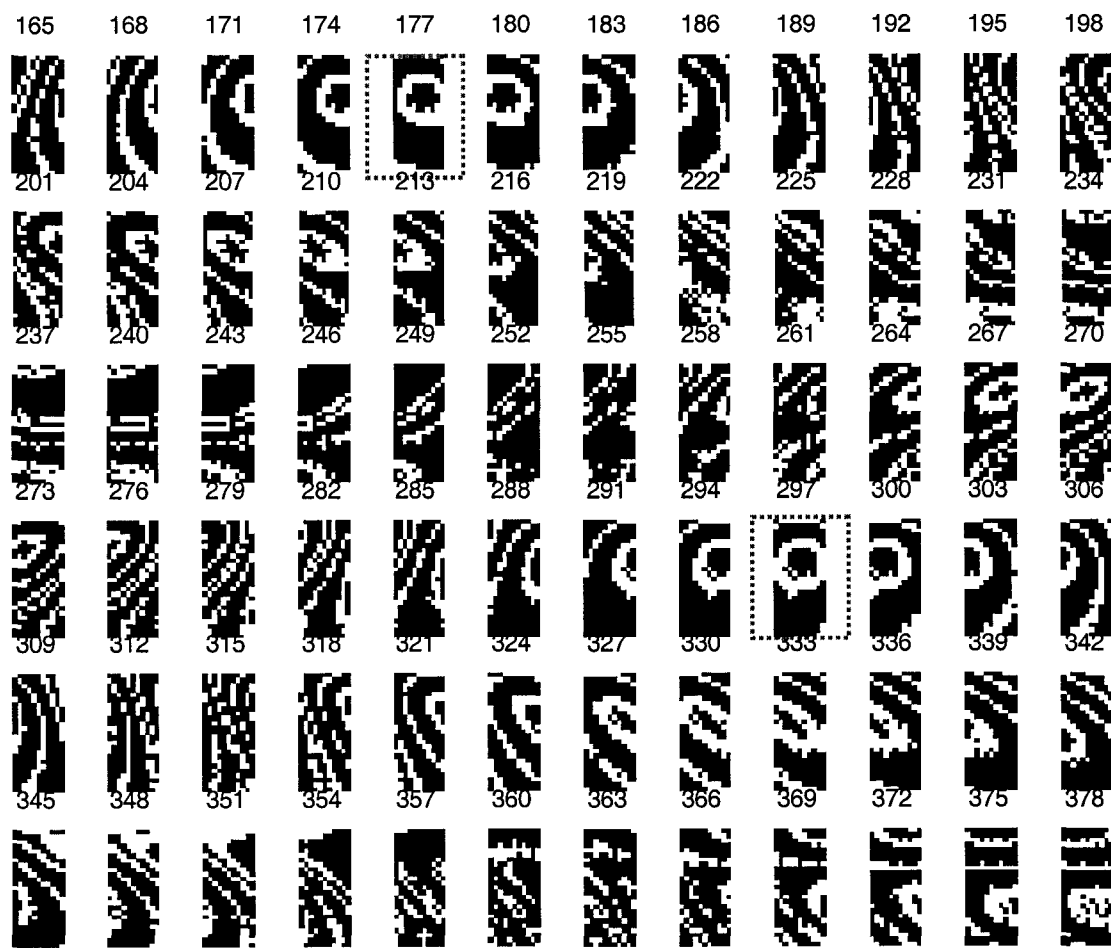






























































Figure 6.3 The DWFP sequence of the signal in Figure 6.2. The number on the top of each DWFP is the time where the DWFP is generated. Note the two patterns at 177 ns and 297 ns, each has a well developed circle inside. The wavelet used: Mexican hat. Scale range: 8:32.

TABLE 6.1
 DWFPS CORRESPONDING TO THE TWO SIMULATED ECHOES

| | | spacing ns | | | | | | | | | |
|-----------|----------|---|---|---|---|---|--|---|---|---|---|
| | | 50 | | 80 | | 100 | | 120 | | 160 | |
| | | 1st | 2nd | 1st | 2nd | 1st | 2nd | 1st | 2nd | 1st | 2nd |
| SNR dB | ∞ |  |  |  |  |  |  |  |  |  |  |
| | 24 |  |  |  |  |  |  |  |  |  |  |
| | 18 |  |  |  |  |  |  |  |  |  |  |
| | 12 |  |  |  |  |  |  |  |  |  |  |
| | 6 |  |  |  |  |  |  |  |  |  |  |
| | 0 |  |  |  |  |  |  |  |  |  |  |

6.4 Echo Detection Algorithm

Now that a distinctive DWFP pattern has been found, an automatic echo detection algorithm can be developed based on it. A flowchart of the algorithm is shown in Figure 6.4.

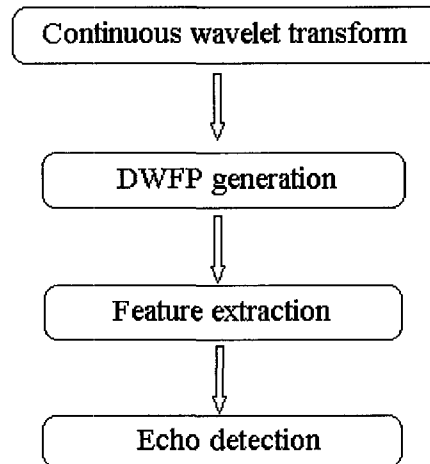


Figure 6.4 Flowchart of the DWFP-based echo detection algorithm.

The algorithm consists of the following steps:

1. Perform continuous wavelet transform on the original waveform. The selection of wavelet is important in that it will affect the recognition and characterization of the distinctive pattern. In this chapter, the Mexhat wavelet is used because of the easy-to-recognize patterns being generated.

2. Generate a DWFP at each sample point. The key parameter to be decided upon is the size of the window, which varies from case to case depending on the specific application. Generally, it should be just large enough to incorporate significant features in

generated patterns. In this chapter, an 11 *ns* window is used so that a center circular region in the distinctive DWFP can be incorporated.

3. Extract features from each DWFP. In this chapter, the existence of the well-developed circle is the main characteristic of the distinctive DWFP. The eccentricity, defined as the ratio of the distance between the foci of the ellipse, which has the same second-moments as the center white region, and its major axis length, is calculated and used as the feature. For an ideal circle, its eccentricity is 0, for a straight line, its eccentricity is 1. A circularity curve is generated by calculating (1- eccentricity) at each sample point.

4. Detect transient echoes from the circularity curve. The significant peaks in the circularity curve which dominate in their neighborhood are picked out as true echoes. By “dominant”, we mean that the value of the peak is the largest in its neighborhood. In this dissertation, the neighborhood is taken as ± 60 *ns* . Hence the resolution limit between two echoes is 60 *ns* .

6.5 Performance Evaluation

The feasibility and performance of this algorithm was evaluated by automatically processing simulated ultrasonic signals at different operating conditions. Instead of using a two-echo model, a five-echo model is constructed with (6.1) and (6.2) as following:

$$A_i \text{ is designed as } A_1 = 2A_2 = 4A_3 = 8A_4 = 16A_5 ;$$

$n(t)$ is zero-mean uniform noise with amplitude of A_5 .

The signal-to-noise ratio (SNR) is defined as $20 \log_{10}(A_i/A_n)$, where A_i and A_n represents peak amplitude of each echo and noise respectively. Hence the SNR for echoes 1 to 5 is 24 dB, 18 dB, 12 dB, 6 dB and 0 dB respectively.

Two scenarios are used in the simulation.

(1) Spacing τ_i is kept the same so that periodic spacing is simulated.

(2) Spacing τ_i is changed randomly between 80 ns and 200 ns to simulate random spacing cases.

Simulation and corresponding auto-processing was performed 100 times for each equal spacing case and total 1000 times for the random spacing case. Typical processing results are shown in Figures 6.5 for scenario 1 and in Figure 6.6 for scenario 2 respectively.

Generally, the circularity curve is clean with significant peaks corresponding to real echoes and a few small peaks elsewhere. Such detection ability is largely due to the pattern-based property of the feature extraction algorithm. A DWFP is either accepted as a possible distinctive pattern and then characterized with large fidelity, or rejected. To remove the few interference peaks in the circularity curve, a peak-picking procedure is applied to pick the dominant peak in a ± 60 ns neighborhood. However, this comes with the price of the resolution limit between two echoes. In this dissertation, the ± 60 ns window was chosen based on the fact that the DWFP distorted significantly when the spacing between two echoes is less than about 50 ns.

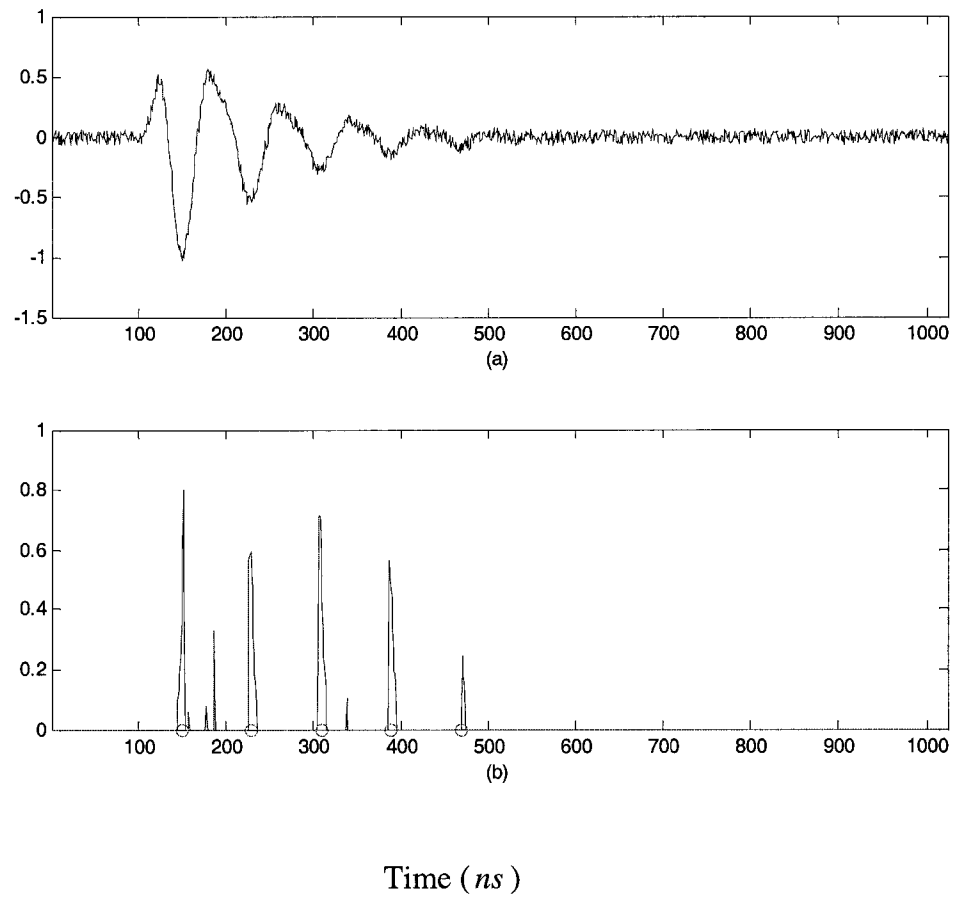


Figure 6.5 (a) Simulated five-echo signal with periodic spacing of 80 ns. (b) The circularity curve. The circles on the x-axis indicate the actual locations of the echoes. Note that each echo has a significant peak associated with it, even for the weakest one (SNR = 0 dB).

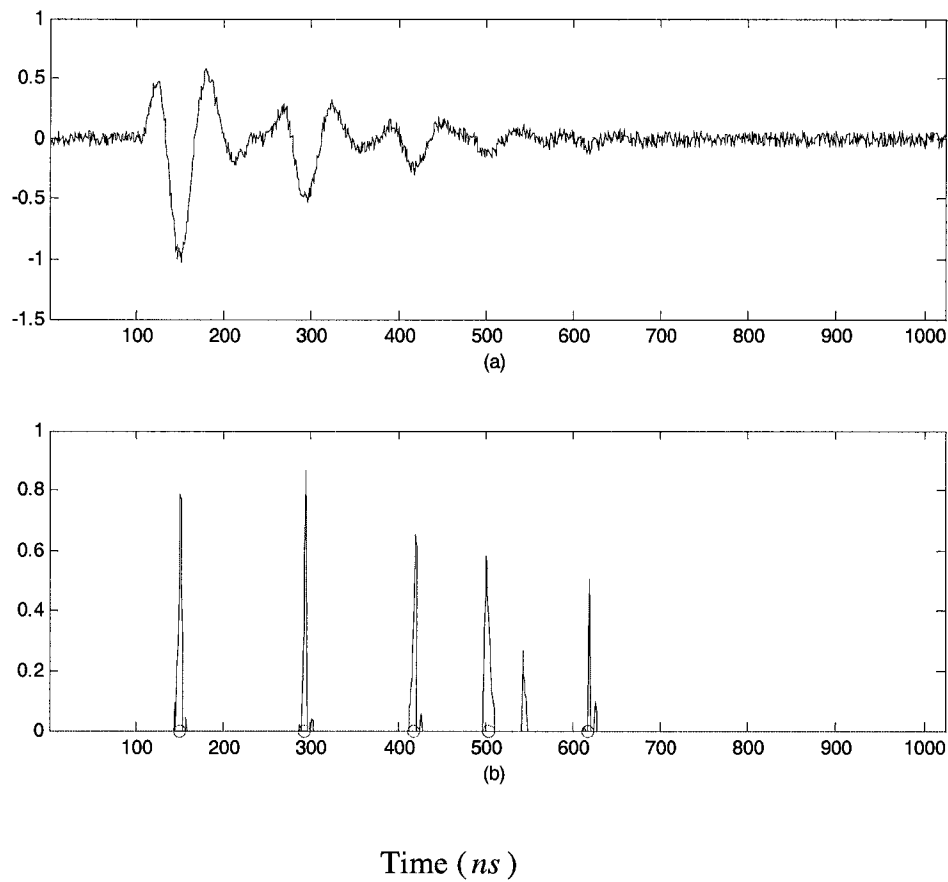


Figure 6.6 (a) Simulated five-echo signal with random spacing. (b) The circularity curve. The circles on the x-axis indicate the actual locations of the echoes. Note that each echo has a significant peak associated with it, even for the weakest one (SNR = 0 dB).

Intuitively it can be seen that the detection precision is very high. Actually, if an echo is detected, the bias of the detected location from the true location is usually within $\pm 5 \text{ ns}$. The detection is also robust in that echoes at low SNR levels still can be automatically detected without any filtering.

Quantitatively, a performance index called detection ratio (DR) is proposed to evaluate the performance of the algorithm. In every simulation, for each of the five known echoes, if it is detected with a precision of $\pm 5 \text{ ns}$ by one and only one detected peak, the detection count increases by one for this known echo. The DR is defined as the ratio of its detection count to the number of simulation. For example, if an echo is detected 87 times in 100 simulations, the DR for this echo is 87%.

The quantitative result for the equal spacing case is shown in Figure 6.7. As can be seen, the detection ratio decreases as the SNR level of the echo goes down, which is as expected. However, even at very low SNR levels, about 50% of the echoes still can be detected with a precision of $\pm 5 \text{ ns}$ (Five sample points).

It is interesting to note that, at the same SNR level (the same line in Figure 6.7), the detection ratio does not always increase with spacing. Instead, the detection ratio is very high for the narrowly spaced cases ($<95 \text{ ns}$). It decreases significantly for the spacing range from 120 ns to 140 ns and increases again. Such fluctuation may be caused by the limited duration (128 ns) and the periodic property of the simulated signal, i.e., for some spacing cases, the interaction between the simulated echoes may lead to “difficult” patterns to be recognized.

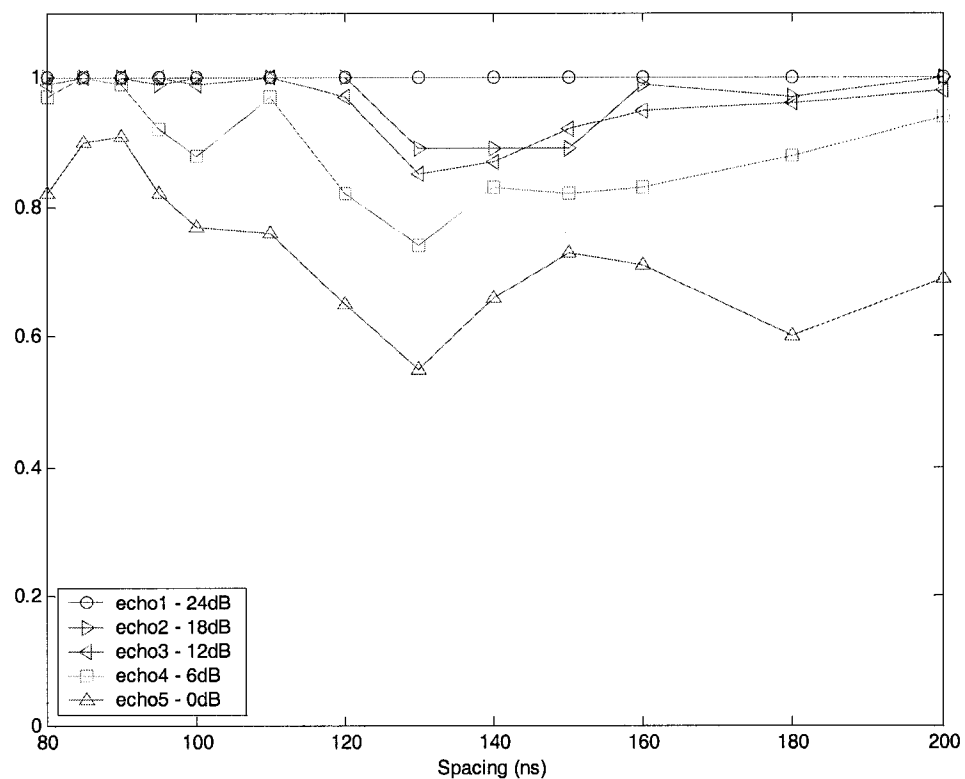


Figure 6.7 Detection ratios of equally spaced echoes. For each spacing case, there are five echoes representing different SNR levels to be detected. The precision of the detection is ± 5 ns.

TABLE 6.3

DETECTION RATIO OF FIVE RANDOM SPACED ECHOES REPRESENTING DIFFERENT SNR LEVELS

| SNR (dB) | 24 | 18 | 12 | 6 | 0 |
|----------|------|-------|-------|-------|-------|
| DR | 100% | 96.6% | 95.3% | 88.2% | 70.1% |

For random spacing cases, the spacing between any two echoes varies from 80 *ns* to 200 *ns*. As shown in Table 6.3, the detection ratio decreases as the SNR level of the echo goes down, which is as expected. Again, even at very low SNR levels, there is still more than 70% chance for an echo to be detected with a precision of ± 5 *ns*.

In this chapter, no filtering was applied to the simulated signal. For echoes with low SNR level, their DWFP patterns become noisy also. The feature extracted therefore becomes unstable, which can lead to poor detection ratio. However, by using additional filtering procedures, such as pruning and thresholding [11], noise can be suppressed and higher detection ratios may be obtained.

Since the duration of a single echo is 128 *ns* and the simulated spacing is from 80 *ns* to 200 *ns*, this work is actually dealing with partially overlapped echoes. Although the detection performance is good when the spacing is larger than 80 *ns*, the real challenge is encountered when the spacing between two echoes is less than 80 *ns*. The overlapping is so significant that the DWFP patterns are distorted significantly so that the DWFP with a well-developed circle inside cannot be used as the distinctive pattern of the true echoes anymore. To overcome such difficulty, one option is to identify different distinctive patterns by experiment/observation and then develop a corresponding auto-detection algorithm. Another option is to use higher frequency ultrasound so that the overlapping can be physically reduced.

6.6 Ultrasonic Imaging of Microelectronic Device

The reliability of modern microelectronic devices is of great concern because of the severe environment where they are working. Generally, these devices are multilayer structures consisting of one or more semiconductor dies mounted on a substrate with various attaching paste. Typical failures are delaminations, cracks, voids, metal corrosion, and so on; they are generally localized at the interface between different layers [110]. Ultrasonic imaging has already been demonstrated as an effective non-destructive technique to inspect the integrity of microelectronic devices. One of the key steps in ultrasonic imaging of microelectronic devices is to identify the echoes corresponding to each interface. Due to the thinness of each layer, it usually requires an expert to figure out the suitable inspection parameters.

As a further evaluation of the proposed ultrasonic echo detection algorithm, it is used here to process the ultrasonic waveforms generated on a plastic encapsulated IC package. A schematic of the sample is shown in Figure 6.8.

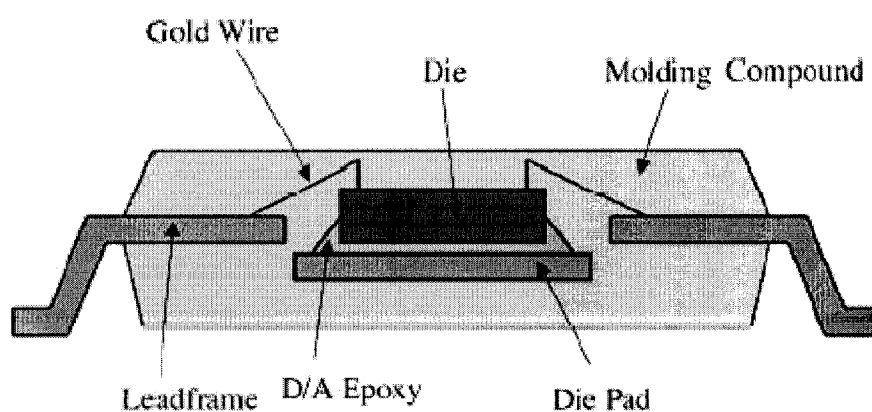


Figure 6.8. Cross-section schematic of a plastic encapsulated IC package.

The waveform acquisition was carried out in pulse-echo mode with a raster scanning set up. The system used is a SONIX UHR-2001[®] high resolution scanning acoustic microscope (Figure 6.9). A 75 MHz transducer with a focal length of 12 mm was used. The sampling frequency is 1 GHz. The scanning resolution is $50\ \mu\text{m}$.

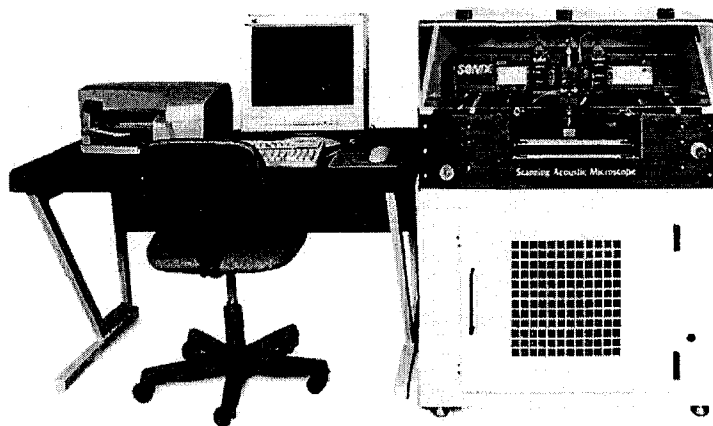


Figure 6.9 UHR-2001[®] Scanning Acoustic Microscope. (Courtesy of Sonix, Inc.)

The resulting ultrasonic image gives a top view of the internal structure of the plastic encapsulated IC package is shown in Figure 6.10. The region of interest where the ultrasonic waveforms were collected is the center area (including the die and the die pad) as indicated by the blue box. At the $50\ \mu\text{m}$ scanning resolution, it corresponds to a 210×210 grid. A typical ultrasonic waveform is shown in Figure 6.11(a). The corresponding DWFP sequence is shown in Figure 6.12. Note that some DWFP patterns have a well-developed circle inside. They are indications of candidate echoes from different interfaces. Using the circularity as the feature of the DWFP patterns,

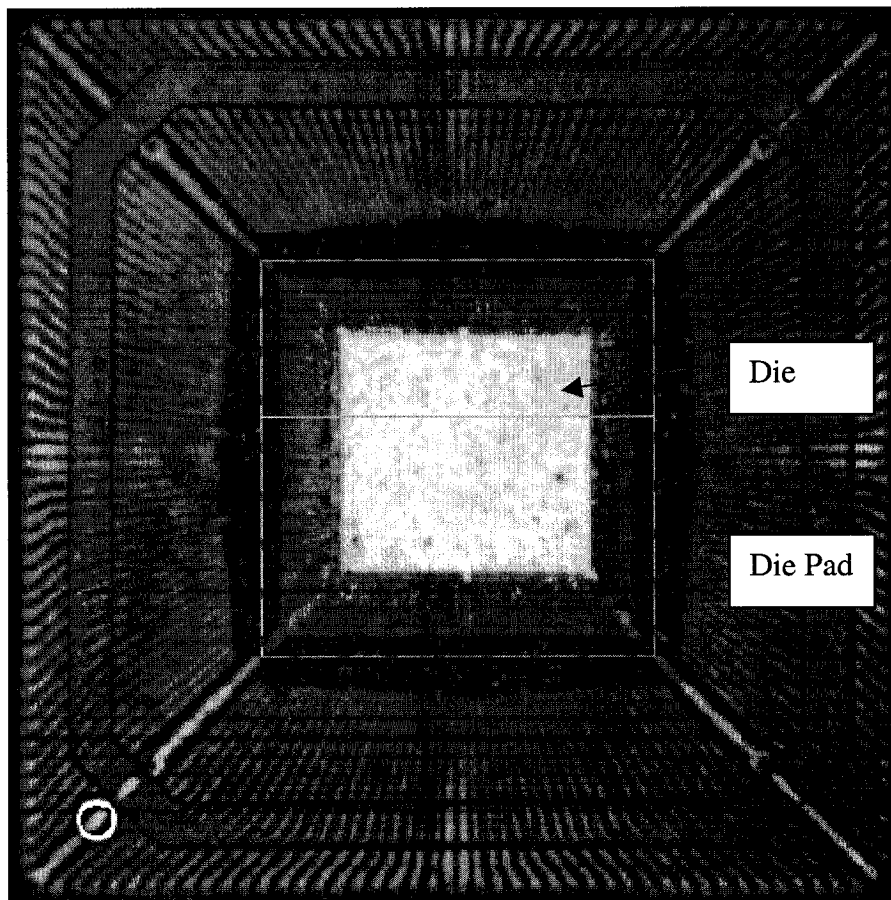


Figure 6.10 Ultrasonic image giving a top view of the internal structure of a plastic encapsulated IC package. The blue box indicates the region where the ultrasonic waveforms were collected.

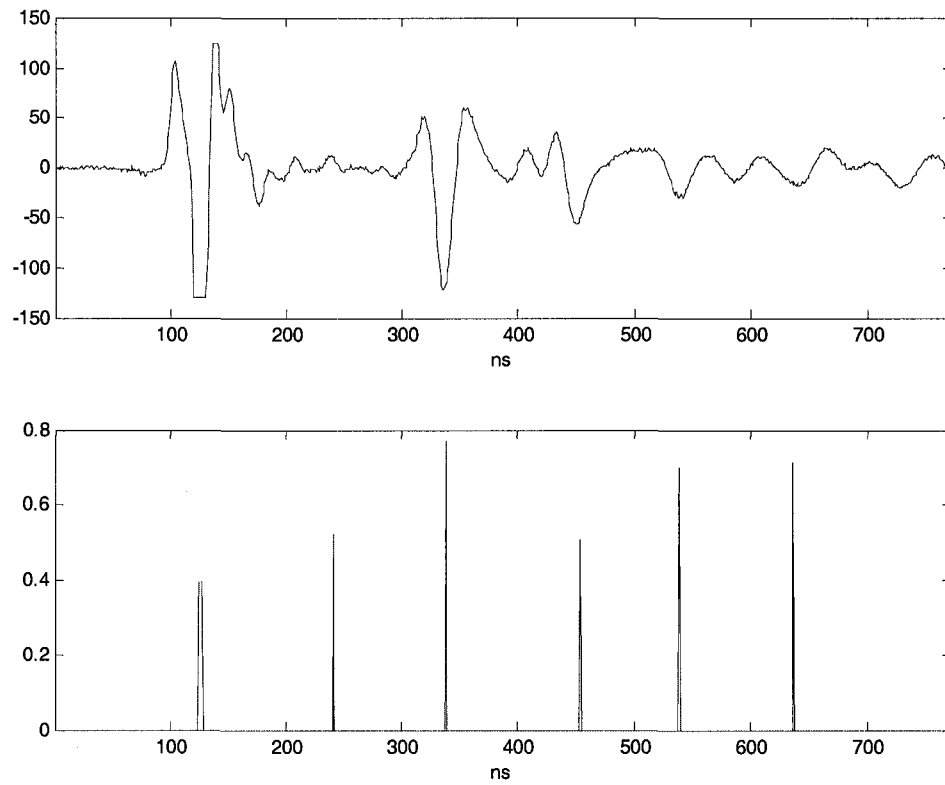


Figure 6.11 (a) A ultrasonic waveform collected on the plastic encapsulated IC package. (b) The circularity curve of the same waveform. The significant peaks indicate the locations of suspect discontinuities.

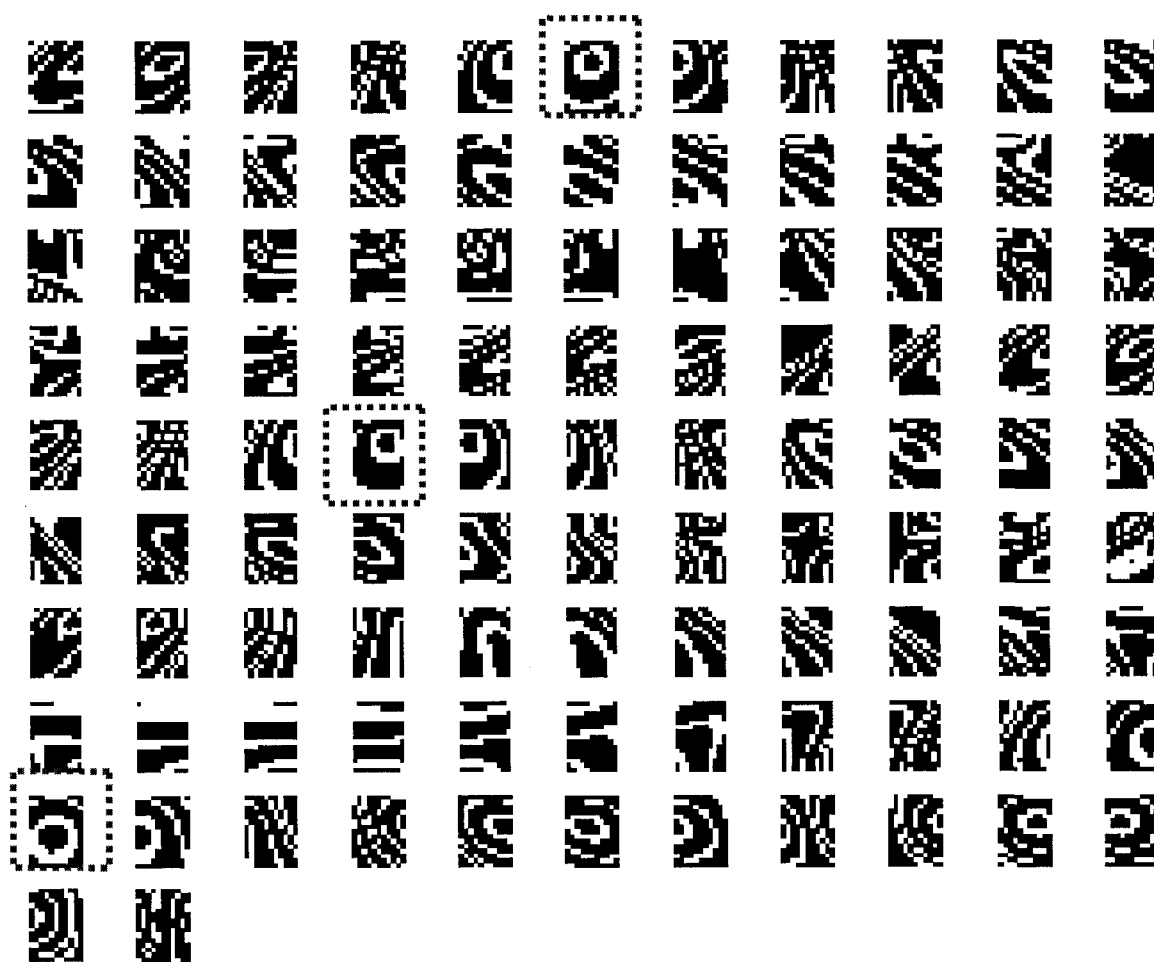


Figure 6.12 The DWFP sequence of the waveform in Figure 6.11(a). Note some patterns have well developed circle inside. The wavelet used: Mexican hat. Scale range: 6:20.

the corresponding circularity curve was calculated and is shown in Figure 6.11(b). The sharp peaks clearly indicate the locations of suspected discontinuities. Applying the same procedure to a series of waveforms along a straight line, a B-Scan cross-sectional “interface image” can be generated as shown in Figure 6.13(a). Suspected interfaces such as the die top and the die attach are clearly highlighted as white lines in the image. Also can be seen is obvious die tilt. For comparison, a standard B-Scan image generated with a commercial scanning acoustic microscope is shown in Figure 6.13(b).

6.7 Conclusions

This chapter presents a new approach for the detection of multiple ultrasonic echoes in the thin multilayer structures and the estimation of their locations. The basic idea is to make use of the two-dimensional property of the time scale (frequency) representation and develop a knowledge-based signal processing technique. A dynamic wavelet fingerprint is generated at each sample point to characterize the local time-frequency structure. A distinctive DWFP pattern with a well-developed circle inside was used to automatically detect multiple echoes under different simulation conditions.

The performance of the algorithm was evaluated with simulated ultrasonic signals. It shows that the proposed algorithm has advantages of high precision, low ambiguity, robustness and that it can be used to detect partially overlapped echoes.

Further evaluation was carried out by applying the proposed algorithm on ultrasonic waveforms obtained from a plastic encapsulated IC package. Similar DWFP

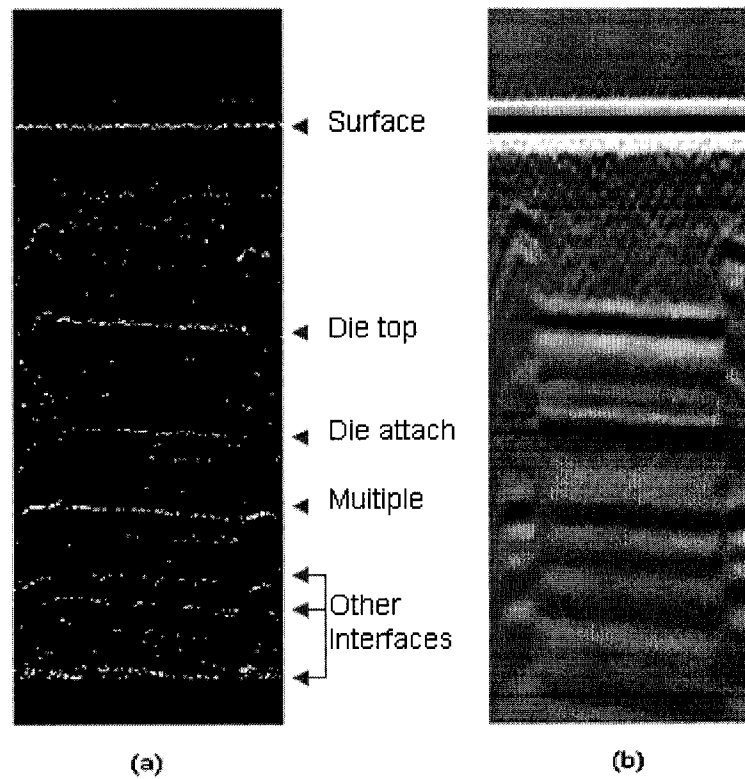


Figure 6.13 (a) The B-Scan image generated with the proposed echo detection algorithm. Suspected interfaces can be seen as white lines in the image. (b) The standard B-Scan image generated with a commercial scanning acoustic microscope.

patterns were found for these practical waveforms. Multiple interfaces were detected as white lines in a B-Scan image.

The feature used in this chapter to characterize the distinctive DWFP is the circularity. Although simple to use, it may not be robust enough to totally remove noise. Additional features may be added in further research to improve the detection performance.

CHAPTER VII

CONCLUSIONS AND FUTURE WORK

Transient signal detection and characterization remains a critical topic in many ultrasonic inspection and imaging applications. The ultimate goal is to answer two basic questions: *when* does a transient occur in the ultrasonic waveforms and *what* does it represent?

Traditionally these two questions are answered separately: we make a decision based on some threshold values if a transient signal is present and estimate its location, then we analyze its property for identification and classification purposes. On the other hand, traditional detection and estimation techniques are generally based on physical or statistic models. However, in practical applications the distribution and property of the defects or abnormalities inside the object under test is usually unknown, which makes the model-based approach problematic.

A pattern-based approach was proposed and presented in this dissertation to address the detection and characterization issues in a coupled way. The basic idea is to generate dynamic wavelet fingerprints to differentiate actual transient signals from noise so that actual transients can be detected; at the same time, the dynamic wavelet fingerprints can be used naturally as a characterization/recognition tool.

The procedure to generate the dynamic wavelet fingerprint was described in Chapter III. It consists of pulse detection plus slice projection of the continuous wavelet

transform coefficients in the neighborhood of each pulse. It was found that the dynamic wavelet fingerprint is intuitive and self explanatory which directly highlights the differences between different signals.

The choice of wavelet greatly influences the dynamic wavelet fingerprint which is generated. For the same group of signals, some wavelets generate more differentiable patterns that lead to better classification performance. So far, the choice of wavelet for different applications is based on a “trial and error” approach. How to choose or design an “optimum” wavelet for a specific application remains an interesting topic for future work.

Another important parameter to generate a dynamic wavelet fingerprint is the time window used to isolate the transient signal of interest. Although the full width at half maximum power (FWHM) is proposed in Chapter III, as shown in later examples, this window can be just large enough to incorporate significant information to fully characterize the transient signal of interest.

To extract features from dynamic wavelet fingerprints, the moment invariants developed in the computer vision field were proposed in Chapter III. Although distinctive to characterize different patterns, the computational load is too heavy to be used in many real-time applications. Moreover, the calculation of these invariants is a “black-box” operation. The outputs are abstract values which are hard to understand by humans, so an artificial neural network or other classifier is needed to handle these numbers. However, as its name implicates, the dynamic wavelet fingerprint does show some patterns like “arch”, “loop” and “whorl”. Therefore it is possible to use advanced fingerprint

recognition techniques to extract significant information from the dynamic wavelet fingerprints. Actually, as seen in the later chapters, different features (generally simple and straightforward) were selected and extracted based on direct observation of the dynamic wavelet fingerprints and the specific goal of the application.

As the first demonstration of the use of the dynamic wavelet fingerprint for ultrasonic signal recognition, an ultrasonic materials sorting system was developed to differentiate several plates by learning and recognizing the dynamic wavelet fingerprints of corresponding echoes from the plate surface. Excellent performance was achieved with 100% ratio of correct identification.

Other applications covering a broad spectrum in ultrasonic inspection and imaging fields were then tested. From a frequency point of view, the range is from 1 MHz, 15 MHz up to 75 MHz. It covers both pulse echo and through transmission modes, ultrasonic NDE and medical imaging, bulk waves and guided waves. The sequence of these studies is chronologically arranged in this dissertation. Consequently, the early studies may not use the most optimal technique.

The first application is ultrasonic periodontal probing. As a novel diagnostic tool, this system uses ultrasound to measure the depth of the periodontal pocket. Due to the complex anatomy of the periodontal tissue, the ultrasonic waveforms received are too complicated to be interpreted directly. A dynamic wavelet fingerprint based algorithm was developed to bring out the hidden trend of the variation of the waveform: the regular variation of the inclination of the dynamic wavelet fingerprints. A two-dimensional FFT based algorithm was developed to extract this inclination feature by calculating an

inclination index. Then the regular variation of the inclination can be seen as regular peaks and valleys in the inclination index curve. Based on observations of the results from a simplified phantom, which is a steel block with holes, the regular variations of the dynamic wavelet fingerprints were mapped into three reflection regions: the first significant peak clearly arises from the probe tip, the second significant peak may be caused by the tooth surface, and the third significant peak may correspond to the bottom of the periodontal pocket.

Full-mouth ultrasonic probing data from 14 patients in two visits were then processed automatically with the proposed algorithm. Taking the manual probing results as the “gold standard”, a 40% agreement ratio was found in site by site comparison. Statistically, however, lack of agreement between ultrasonic and manual probing was found in terms of the “limits of agreement” proposed by Bland and Altman. This may arise from the simplified model used in the algorithm. Hence more detailed clinical experiments are required in the future to understand the physics behind the intuitive variation of the dynamic wavelet fingerprints. One suggestion is to generate a two-dimension contour of the periodontal pocket since the point-by-point comparison is strongly affected by random factors such as the force used and the angle with which the probing is carried out, etc. Another suggestion is to improve the stability of the probing hardware. The variation of the water flow during the probing process may cause significant variations in the waveform collected.

The next ultrasonic application demonstrated here is multi-mode Lamb wave tomography. Lamb waves are guided waves that can propagate long distances in thin-wall structures and are sensitive to different defects present in their path. Lamb wave

tomography has been proven as a reliable and efficient non-destructive evaluation technique for large structures such as plates and tubes. Taking advantage of the dispersion characteristics inherent in Lamb wave propagation, Lamb wave tomography maps thickness variations (corrosion, delamination, etc.) into arrival time variations. The sensitivity and precision of the generated tomography is directly related to the accuracy of the arrival times measured experimentally. Another property of Lamb wave is that multi-modes propagate simultaneously in the media. Since different modes are sensitive to different types of defects, it is reasonable to generate tomographic reconstructions for each mode. However, due to the dispersion and multi-mode characteristics, it is challenging to extract the arrival times of each mode, especially with additional requirements of automation and real time extraction.

Based on the assumption that the arrival order of different modes is unchanged, the dynamic wavelet fingerprint based algorithm developed in this dissertation first detects potential modes and then removes false signals by recognizing dynamic wavelet fingerprints for the true modes. Specifically, it was found that the area of the white region of the dynamic wavelet fingerprint can be used as a feature to differentiate actual modes from noise and interference. An experimentally determined threshold was used in the algorithm to implement the classification.

The performance of the proposed algorithm was evaluated by computing mean square errors between 10000-point sequences of experimental and theoretical arrival times, which gave an MS-error of 0.43, 4.23 and 6.29 for the A1, A0 and S0 modes respectively. Tomographic images of four plates were also generated for each mode from the corresponding estimated arrival times. The spatial resolution of all reconstructed

images was good enough to ensure visual detection of all the defects studied, even without post processing of the images.

To optimize the performance of the suggested algorithm, it is necessary to choose carefully the experimental parameters, such as frequency and duration of the wave packet, so that multiple modes are more separated in time or more differentiable in terms of their dynamic wavelet fingerprints. One suggestion is to generate every single mode in a defect free plate and experimentally watch its own dynamic wavelet fingerprint. In this way, better understanding of the variation of the dynamic wavelet fingerprints may be obtained and it may help to design a more robust algorithm.

The last application discussed in this dissertation is ultrasonic inspection of thin multilayer structures. In general, the ultrasonic waveforms received from these structures have multiple echoes which may be partially overlapped. This invalidates most traditional detection techniques, especially for non-destructive evaluation cases where the number and property of the defects are unknown before the test. On the other hand, the slight mismatch of acoustic impedance and attenuation in many multilayers may lead to low signal to noise ratio, which adds another difficulty to detecting and estimating corresponding echoes.

In this application, dynamic wavelet fingerprints were generated at each sample point to achieve maximum resolution capability. By watching the experimental results of simulated ultrasonic signals, it was found that the dynamic wavelet fingerprint with a well-developed circle inside can be used as a distinctive pattern to recognize echoes in the signal. To extract this distinctive feature, the eccentricity of the center white region of

the dynamic wavelet fingerprint was calculated and used to generate a circularity curve. Then the significant peaks in the circularity curve which dominate their neighborhood are picked out as true echoes.

It was found that the proposed algorithm has advantages of high precision, low ambiguity, robustness and that it can be used to detect partially overlapped echoes. Further evaluation was carried out by applying the proposed algorithm on the ultrasonic waveforms obtained from a plastic encapsulated IC package. Similar dynamic wavelet fingerprint patterns were found in these practical waveforms. Multiple interfaces were detected as white lines in the B-Scan image.

It was noted that a few false peaks may still exist in the circularity curves. To remove these false peaks, additional features beside circularity may be required. A database may be built to accumulate experience from known cases so that a knowledge-based system can be developed to achieve robustness and flexibility.

In summary, this dissertation presents a knowledge-based ultrasonic signal processing technique based on the dynamic wavelet fingerprint. Because of its intuitive and self-explanatory characteristics, it is possible to customize an efficient algorithm to highlight the hidden features in a class of signals and achieve satisfactory detection and characterization results.

Finally, the author would like to end this work by citing an old saying: "Seeing is believing."

APPENDIX A

SOURCE CODE OF ULTRASONIC PERIODONTAL PROBING

```

clear
IsShow= 0;
fid=fopen('ERRlog.txt', 'a+');
chan = ddeinit('excel', 'Sheet1');
sum_data =zeros(2048,1);
dirname = 'd:\';

site= {'BD' 'Bmi' 'BMe' 'LD' 'Lmi' 'LMe'};
patient={'RI' 'RC' 'BS' 'SM' 'SMA' 'PAB' 'JW' 'NK' 'KE' 'SL' 'GH' 'DK' 'JJ'};
%patient={'test1-3\P1' 'test1-3\P2' 'test1-3\P3' 'test4-6\P4' 'test4-6\P5' 'test4-6\P6' 'test\P7'
'test\P8' 'test\P9' 'test\P10' 'test\P11' 'test\P12' 'test\P13' 'test\P14'};

for whichP = 6:6
    Ucount = 1;
    UData=zeros(6*32, 1);
    for whichT = 31:31
        MisRead=0;
        for whichS = 1:6
            whichtooth = [patient{whichP} '_' num2str(whichT) char(site(whichS)) '1.txt'];
            filename =[dirname whichtooth];

            try
                ddd= load(filename);
            catch
                ERRmsg = [num2str(whichP) '-' num2str(whichT) ' : ' 'Cannot Load data. Tooth
missing.\n /n'];
                fprintf(fid, ERRmsg);
                if(MisRead ~= 0)
                    Ucount = Ucount - MisRead;
                    for mis=1: MisRead
                        UData(Ucount + mis - 1) = 0;
                    end
                end
                Ucount = Ucount + 6;
                break;
            end
            MisRead=MisRead+1;
            ddd=ddd';
            [m n]=size(ddd);
            if(m ~= 2500)

```

```

        ERRmsg = [num2str(whichP) '-' num2str(whichT) '-' num2str(whichS) ' : ' 'Data
format is wrong.\n'];
        fprintf(fid, ERRmsg);
        exit;
    end
    if(n == 62)
        ERRmsg = [num2str(whichP) '-' num2str(whichT) '-' num2str(whichS) ' : ' 'Data
doubled.\n'];
        fprintf(fid, ERRmsg);
        ddd=ddd(:, 32:62);
    end
    dtemp= ddd(1:2048,:);
    sum_data = dtemp';
    sum_data = mean(sum_data);
    clear dtemp;
    clear ddd
    amp = max(abs(sum_data));
    sum_data=sum_data/amp;

    ns=64;
    if( lsShow==1)
        subplot(6,1,1);
        plot(sum_data, 'k');
        xlim([1 2048]);
    end
    [swa,swd] = swt(sum_data, 5, 'coif3');
    swd(1,:)=0;
    pH = iswt(swa,swd,'coif3');
    if( lsShow==1)
        subplot(6,1,2);
        plot(pH, 'k');
        xlim([1 2048]);
    end
    cf = cwt(pH, 1:ns, 'morl');
    Ecf= mean(cf.^2) ;
    SER = medfilt1(Ecf, 24);
    if( lsShow==1)
        subplot(6,1,3);
        plot(Ecf, 'k');
        hold on
        plot(SER, 'k', 'MarkerSize', 1.5);
        hold on
        xlim([1 2048]);
        hold off
    end
    x_1=diff(SER);
    yR_1 =[0 x_1];
    yL_1 =[x_1 0];
    big_1 = (yL_1>=0);
    yL_1( big_1 )= 5;
    small_1 = (yL_1<0);
    yL_1( small_1 )= 1;
    big_1 = (yR_1>=0);
    yR_1( big_1 )=1;
    small_1 = (yR_1<0);
    yR_1( small_1 )= -5;

```

```

feng = find(yR_1 == yL_1);
if( lsShow==1)
    subplot(6,1,4);
    plot(SER, 'k');
    xlim([1 2048]);
    hold on
    plot(feng, SER(feng), 'ko', 'MarkerSize',1.5)
end

fwidth =24;
s_step=0.25;
s_h=0.05;
swd(:,:)=0;
bak = iswt(swa,swd,'coif3');
cfX = cwt(bak, 1:ns, 'morl');
if( lsShow==1)
    figure(2);
    for dw =1:9*9
        subplot(9,9, dw);
        if feng(dw) > fwidth
            neighbor= cfX(:, feng(dw)- fwidth:feng(dw)+ fwidth);
            neighbor= abs(neighbor);
            top= max(max(neighbor));
            neighbor= neighbor/top;
            tem=neighbor;
            tem(:,:)=0;
            for h=0.1:s_step:1.0
                x= find( (neighbor>=h -s_h) & (neighbor<=h +s_h) );
                tem(x)=1;
            end
            imshow(tem);
        end
    end
end

target= 250;
Pwindow= 8;
FirstPeak=0;
SecondPeak=0;
psize=size(feng);
PeaksNumber= psize(2);
for Pindex =1:PeaksNumber
    if feng( Pindex ) > fwidth & feng( Pindex ) <= (2048- fwidth)
        interface= feng( Pindex);
        neighbor= cfX(:, interface- fwidth:interface+ fwidth);
        neighbor= abs(neighbor);
        top= max(max(neighbor));
        neighbor= neighbor/top;
        tem=neighbor;
        tem(:,:)=0;
        for h=0.1:s_step:1.0
            x= find( (neighbor>=h -s_h) & (neighbor<=h +s_h) );
            tem(x)=1;
        end
        tem= 1- tem;
        tem= abs( fft2(tem) );
    end
end

```

```

t= tem;
tem(:, :)=1;
tem(t< mean (mean(t) ) )=0;
A1= tem(1:32,1:24);
A2= tem(1:32, 26:49);
A3= tem(33:64, 1:24);
A4= tem(33:64, 26:49);
PeakFeature(Pindex) =( sum( sum ( A1 )) + sum( sum ( A4 )) )/( sum( sum ( A2 ))
+ sum( sum ( A3 )) );
else
PeakFeature(Pindex) = NaN;
end
end
xa= find(PeakFeature>0);
PeakFeatureOK= PeakFeature(xa);
mFF= mean(PeakFeatureOK);
stdFF= std(PeakFeatureOK);
FeatureThreshold = 1.0 ;
Pindex=1;

while Pindex <= PeaksNumber
if feng(Pindex)>100 & Pindex >Pwindow & Pindex < ( PeaksNumber - Pwindow)
if(PeakFeature(Pindex)>= FeatureThreshold )
tMax= max( PeakFeature(Pindex-Pwindow: Pindex+Pwindow ) );
if PeakFeature(Pindex) == tMax
if FirstPeak==0
if feng(Pindex)>150 & feng(Pindex)<300
FirstPeak=1;
Pwindow= 8;
else
target=250;
Pindex = PeaksNumber + 1;
end
else
if SecondPeak==0
if feng(Pindex)>=300
SecondPeak=1;
Pwindow= 8;
end
else
target = feng(Pindex);
Ptarget= Pindex;
Pindex = PeaksNumber + 1;
end
end
end
end
end
end
Pindex= Pindex +1;
end
if( IsShow==1)
figure(3);
subplot(6, 1, 1);
plot(feng, PeakFeature, 'k');hold on;
xlim([0,2048]);
ylim([0,2.5]);

```

```

        hold on
    end
    dis= (target -250)* 0.0075;
    UData(Ucount) = dis;
    Ucount = Ucount + 1;
end

clear      Ecf
clear      FeatureThreshold
clear      FirstPeak
clear      MisRead
clear      PeakFeature
clear      PeakFeatureOK
clear      PeaksNumber
clear      Pindex
clear      Ptarget
clear      Pwindow
clear      SER
clear      SecondPeak
clear      amp
clear      ans
clear      bak
clear      cf
clear      cfX
clear      fwidth
clear      interface
clear      m
clear      mFF
clear      n
clear      neighbor
clear      ns
clear      pH
clear      feng
clear      psize
clear      stdFF
clear      sum_data
clear      swa
clear      swd
clear      tMax
clear      target
clear      whichtooth
clear      xa

end
range= ['r' num2str(1) 'c' num2str(whichP) ':r' num2str(192) 'c' num2str(whichP)];
rc = ddepoke(chan, range, UData);
end

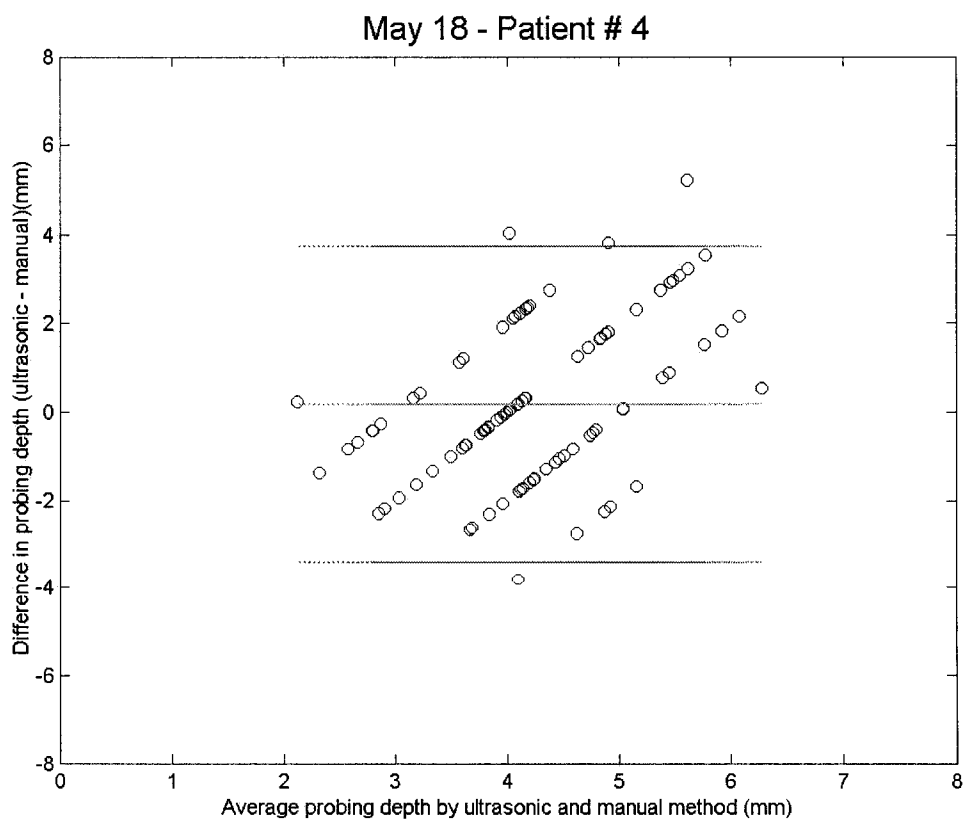
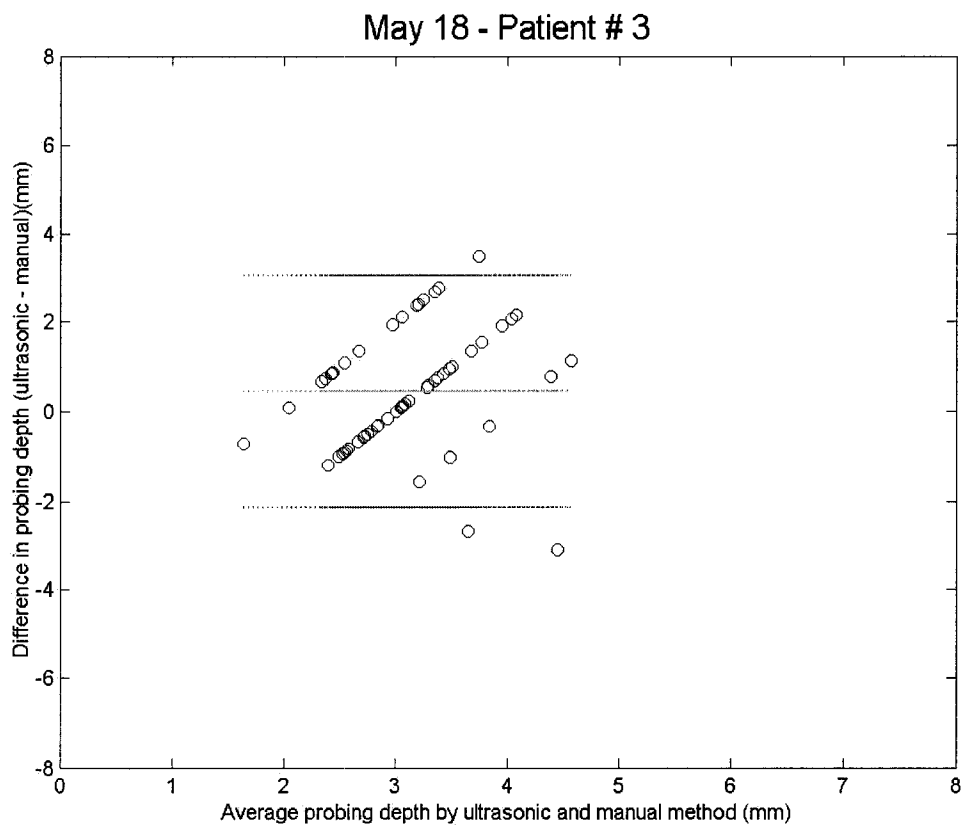
rc = ddeterm(chan);
fclose(fid);
disp('End Processing!!');

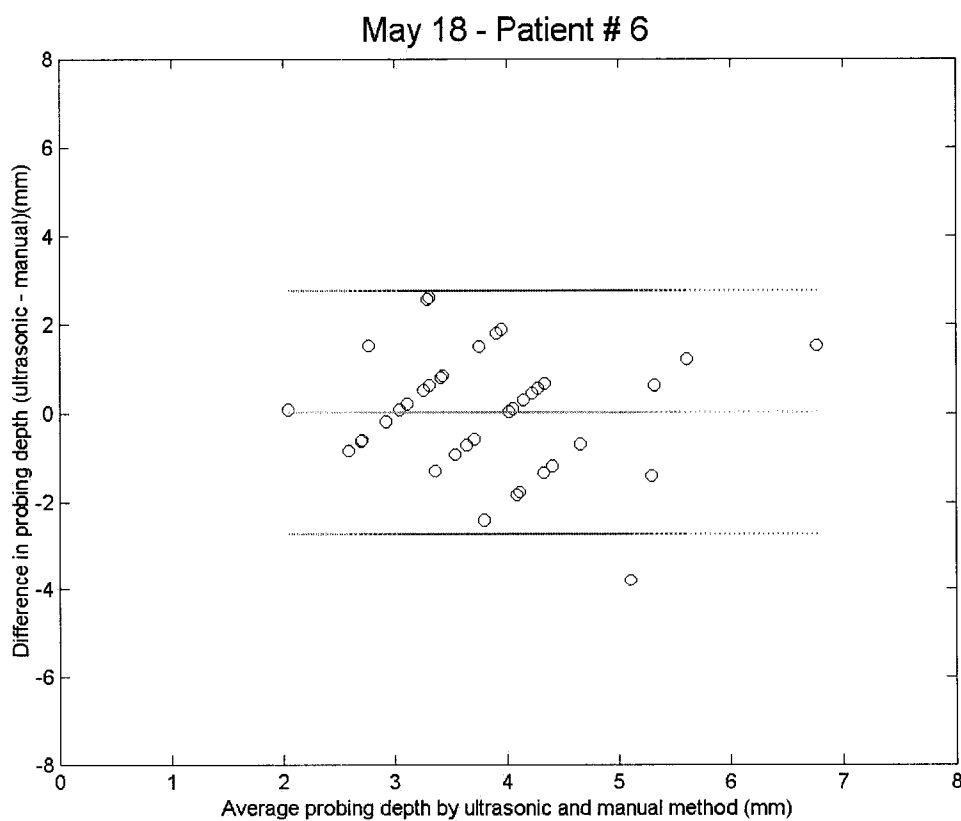
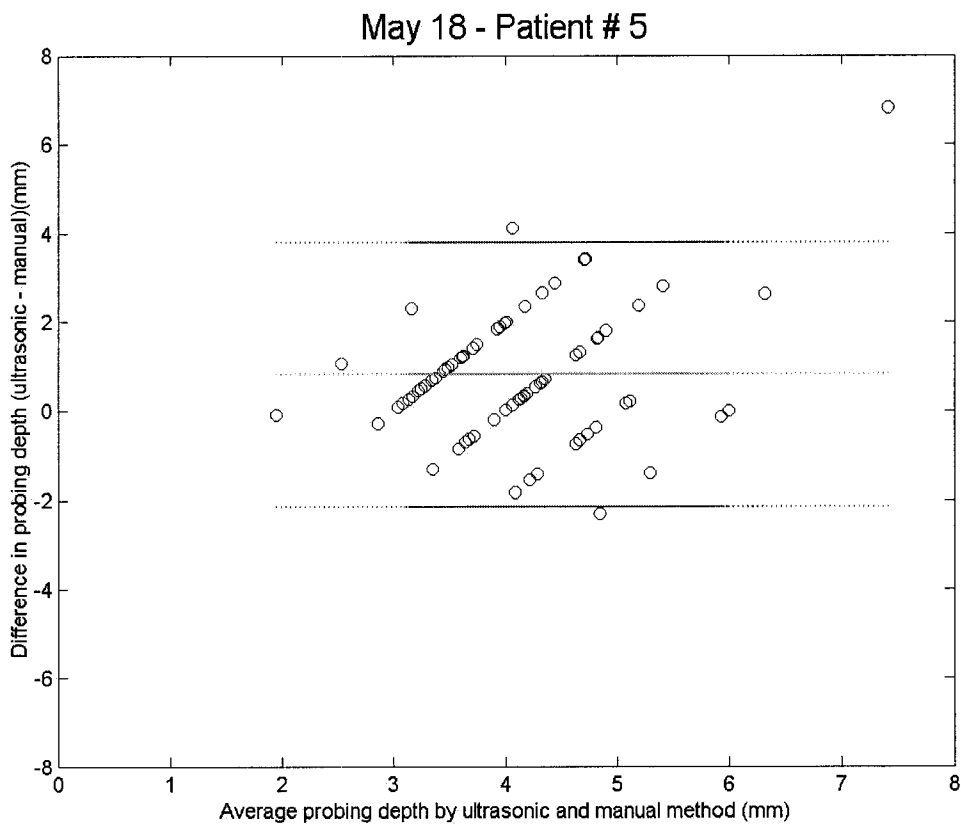
```

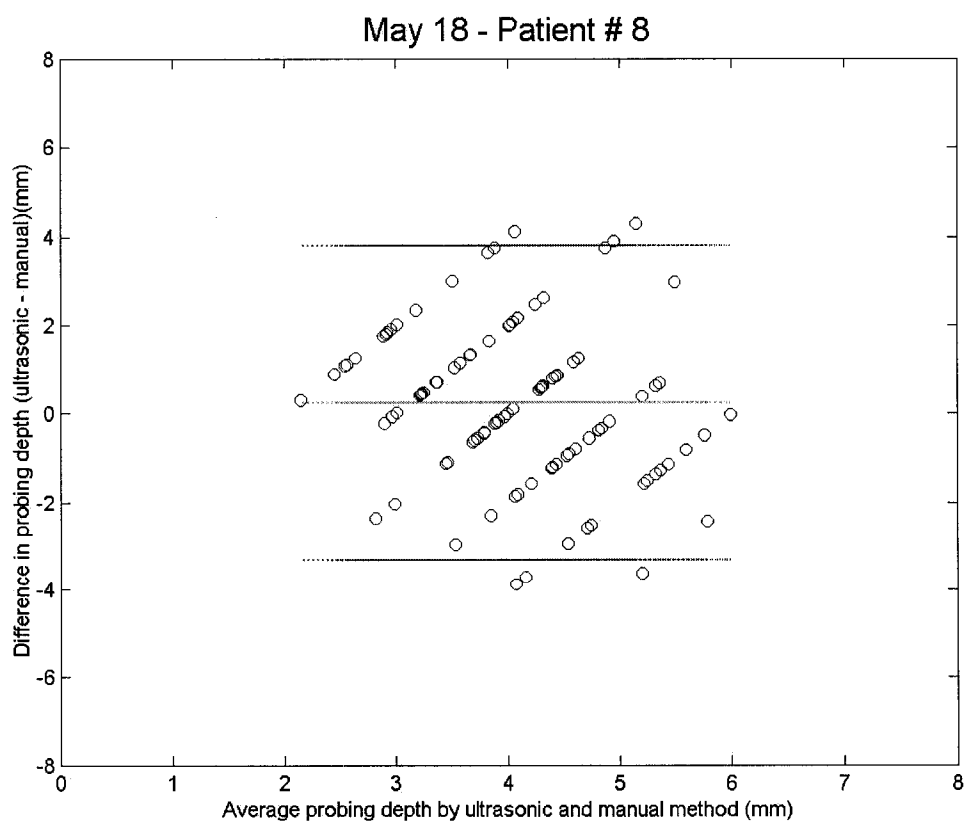
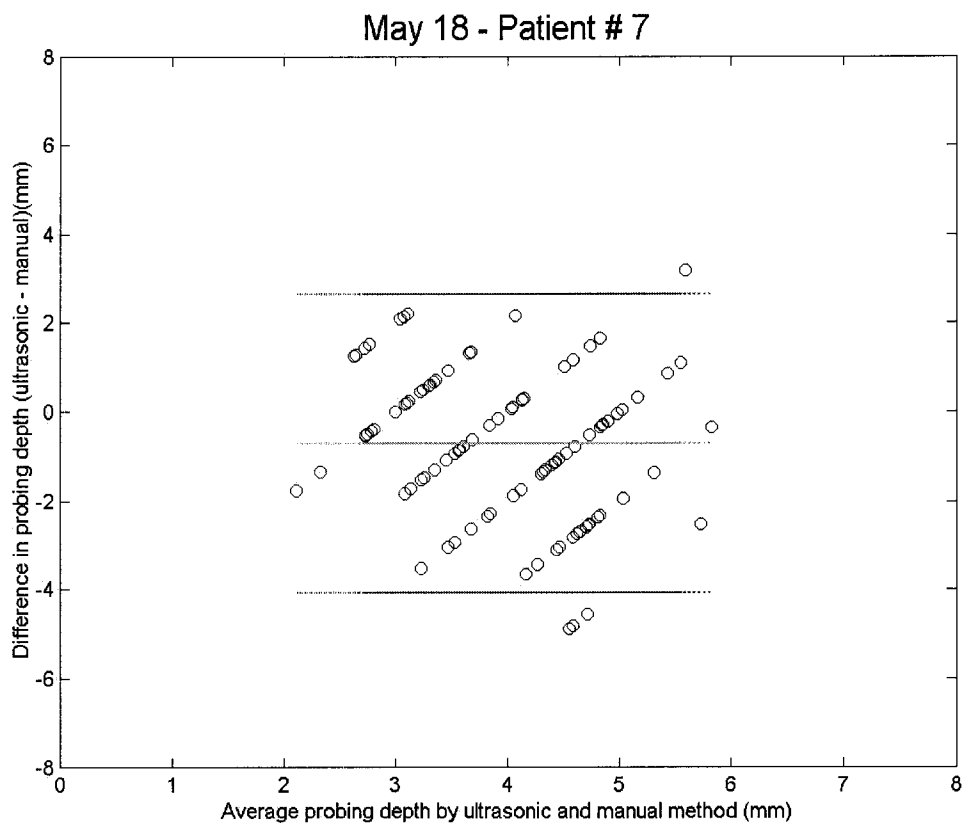
APPENDIX B

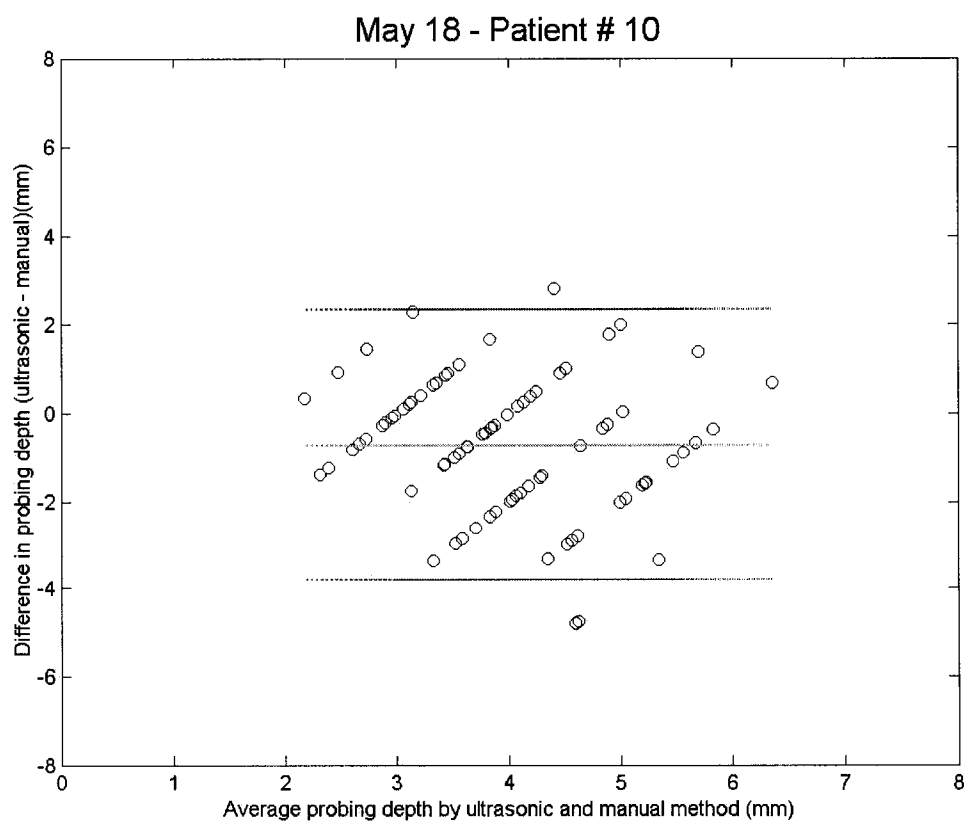
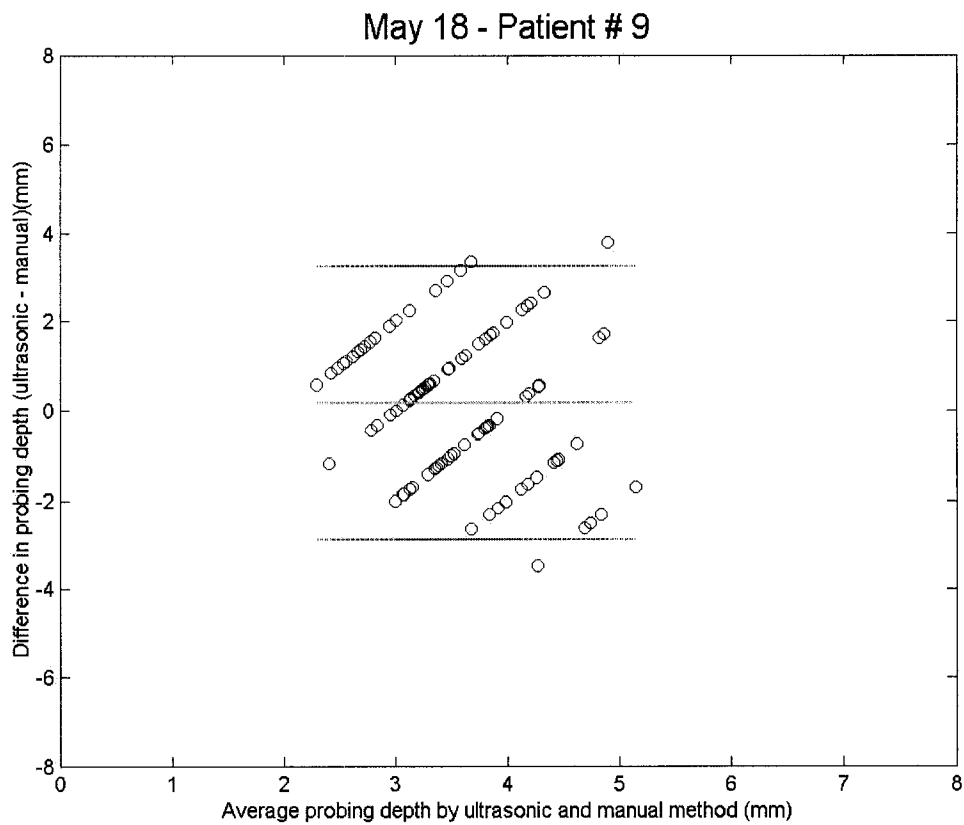
STATISTICAL EVALUATION OF THE AGREEMENT BETWEEN ULTRASONIC PROBING AND MANUAL PROBING METHOD

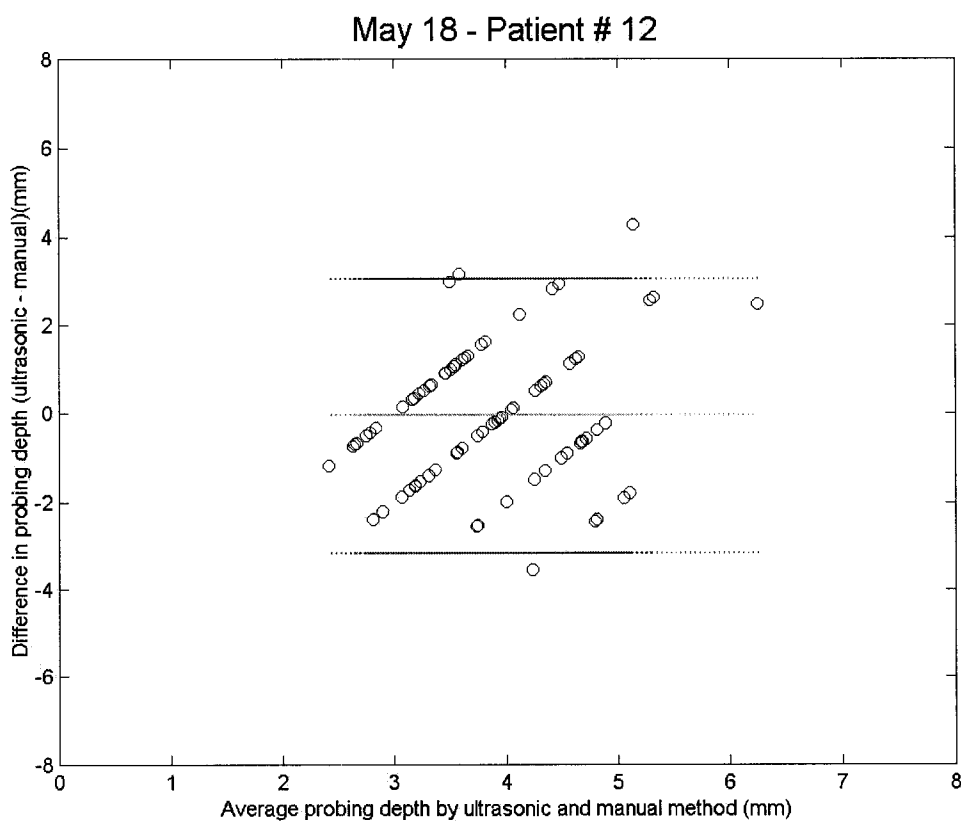
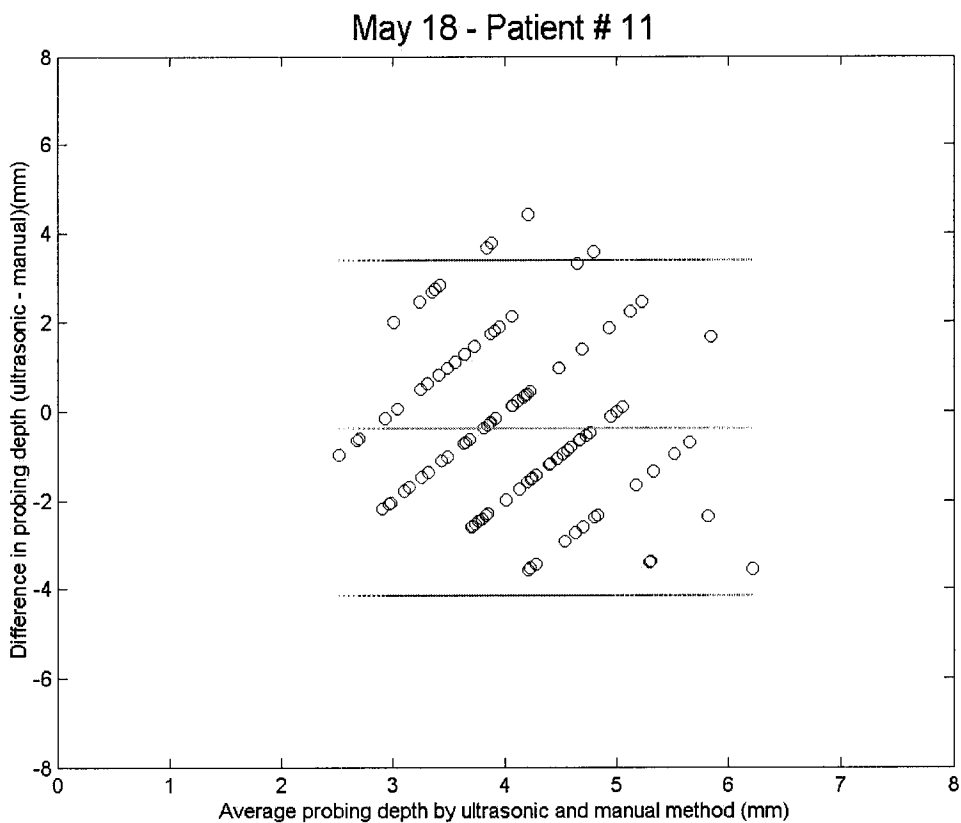
In this appendix, additional evaluation results by the Bland-Altman method are presented for the ultrasonic and manual probing measurements obtained on May 18, 2001 and August 17, 2001.



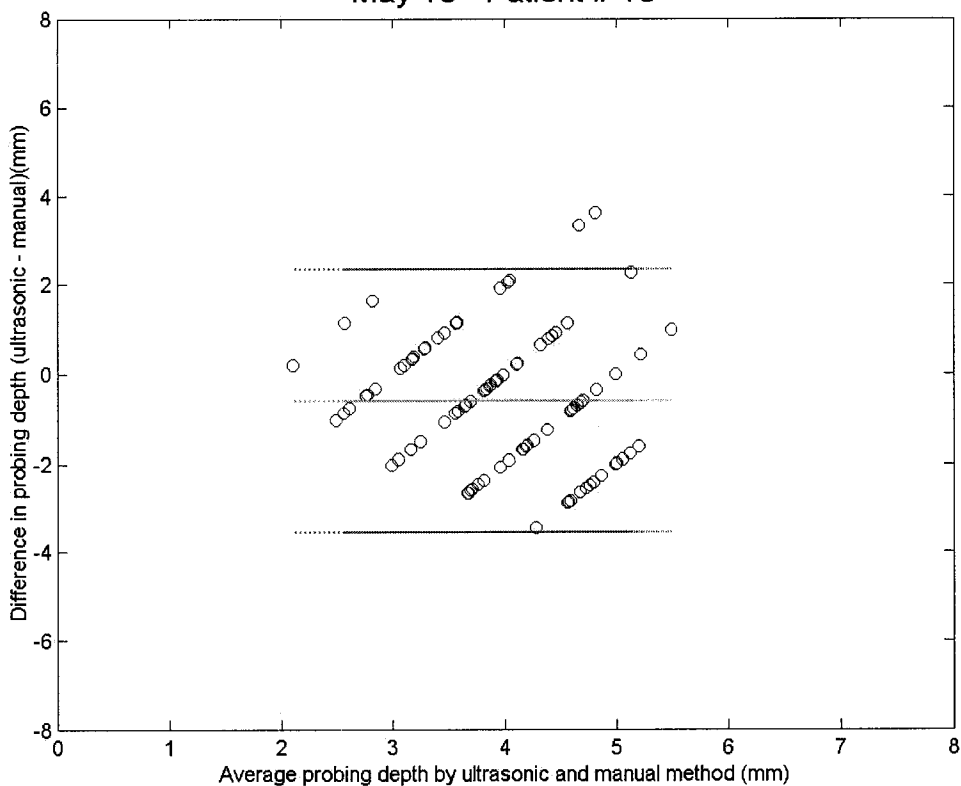




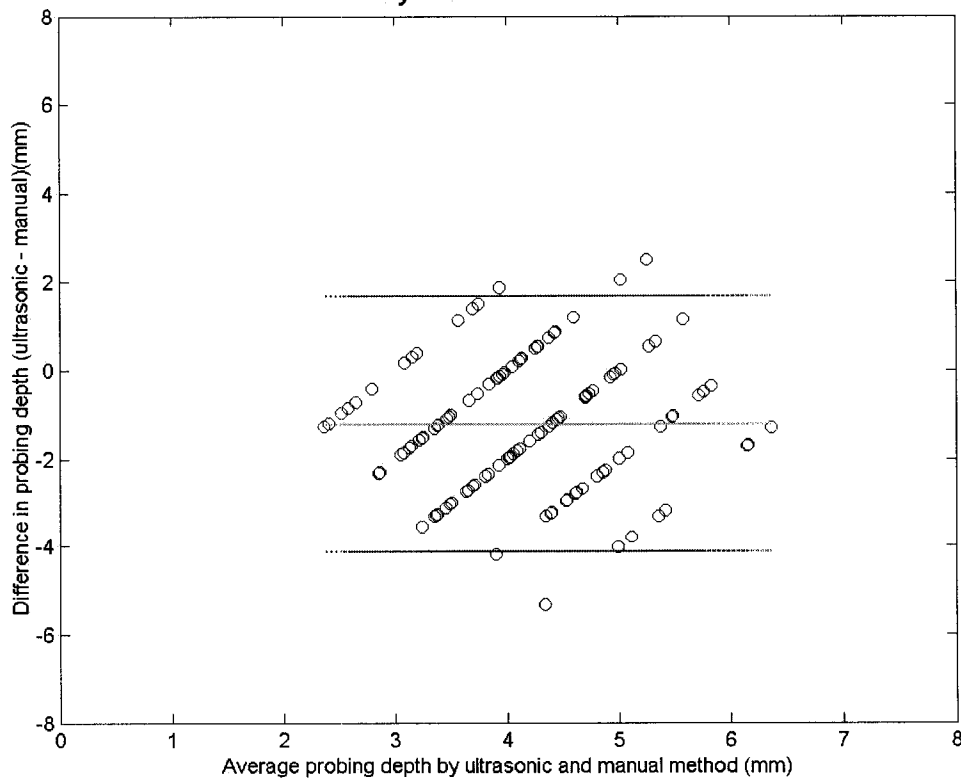


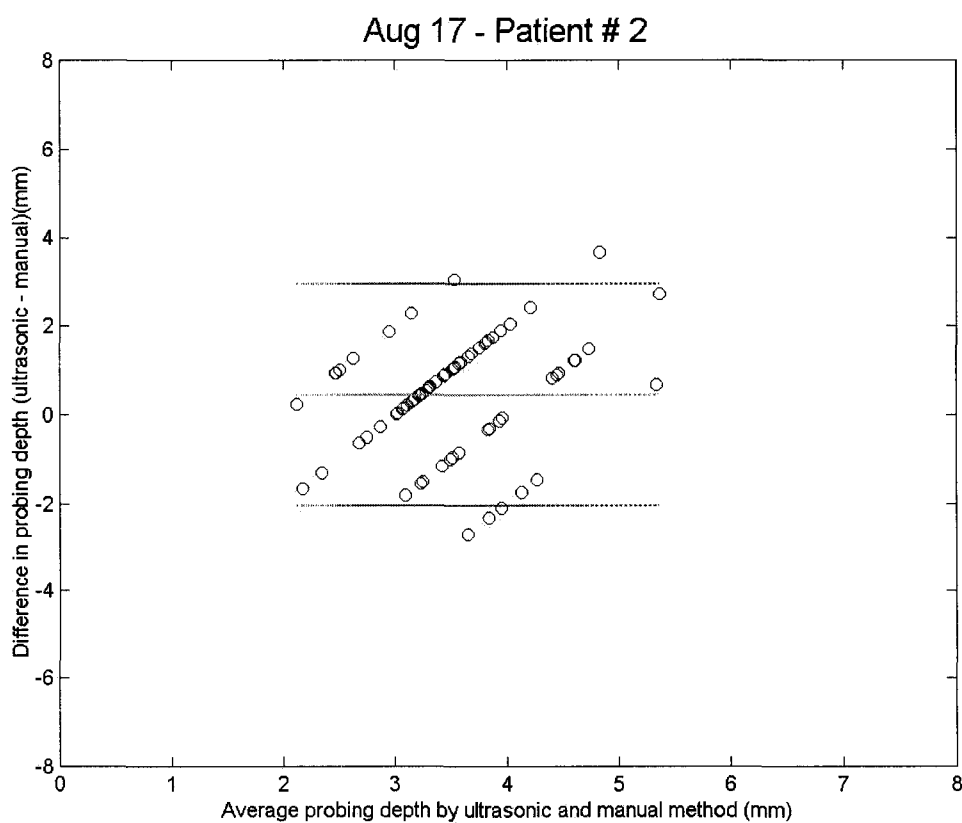
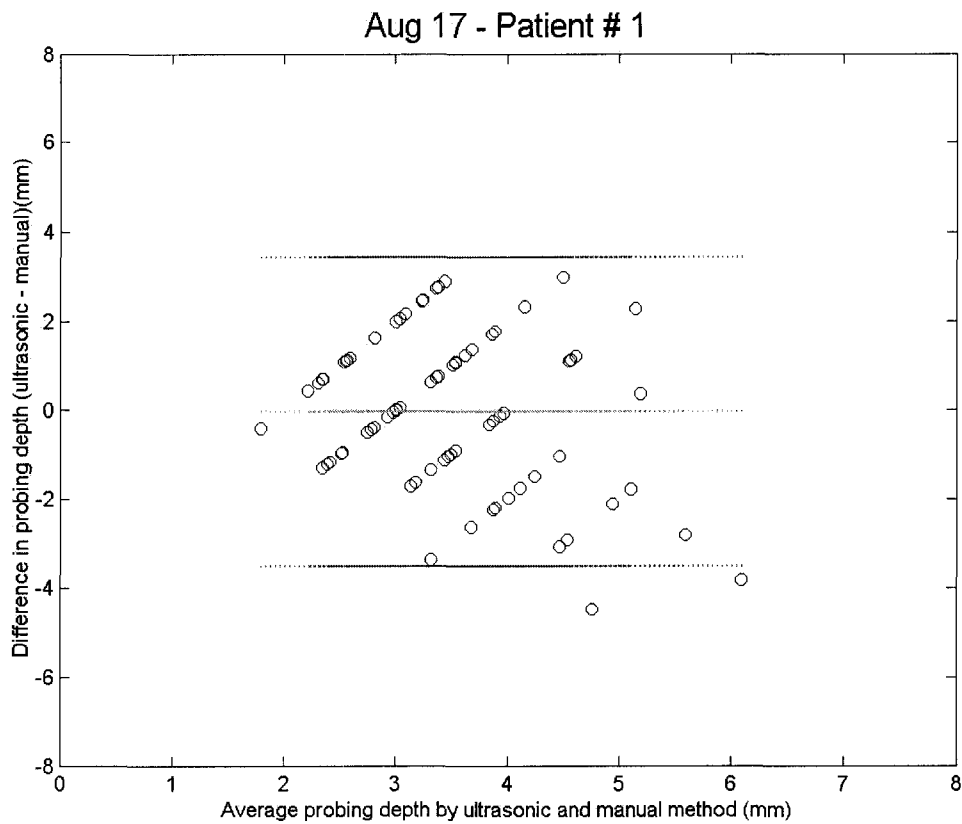


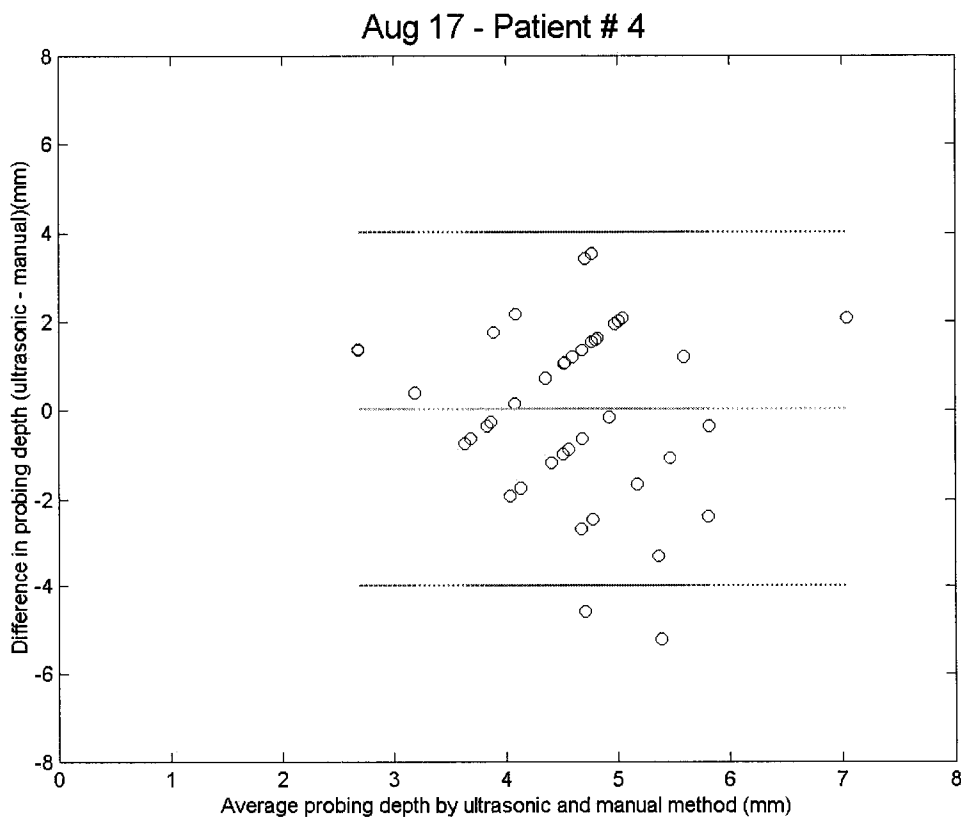
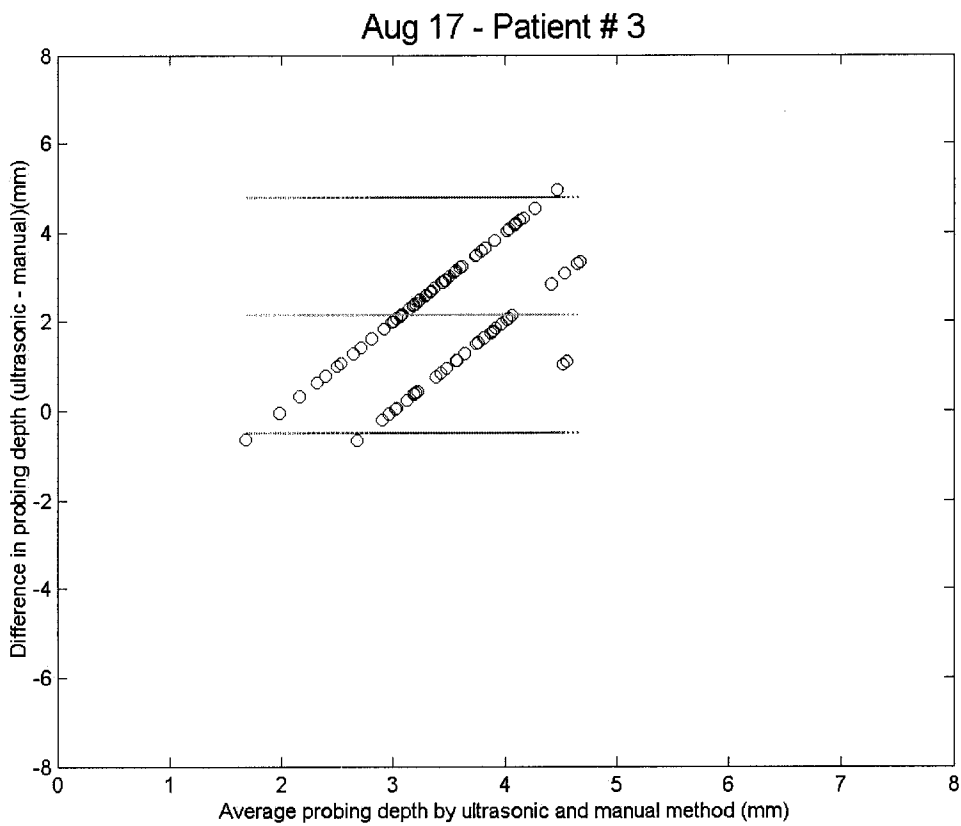
May 18 - Patient # 13

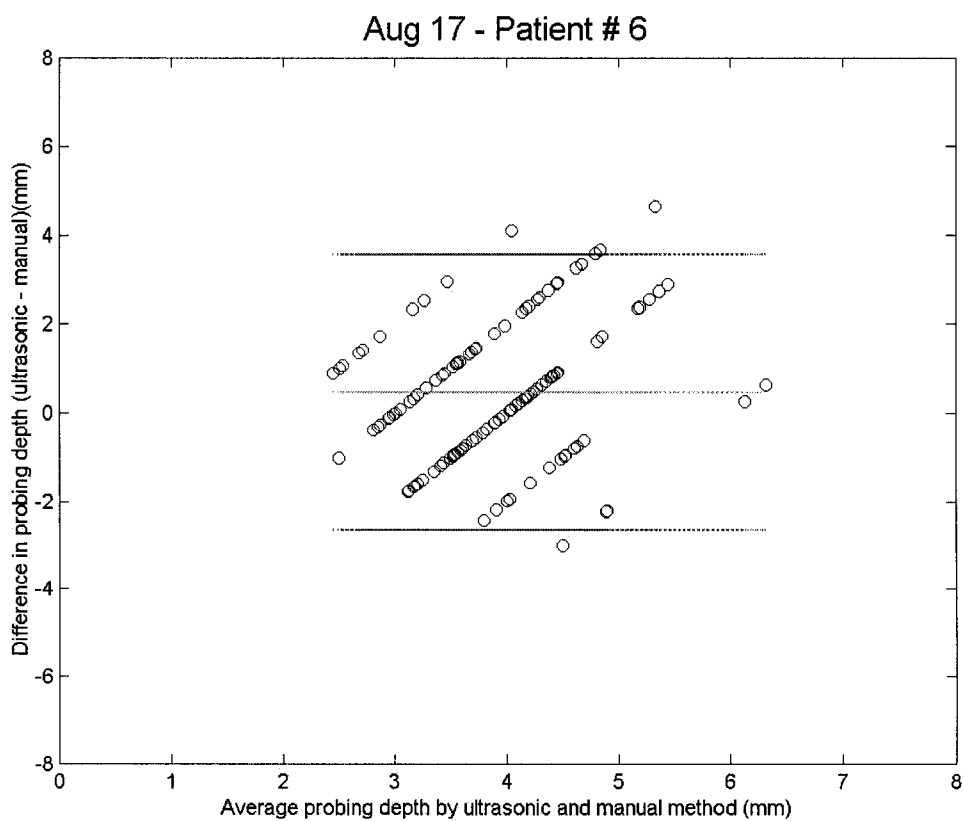
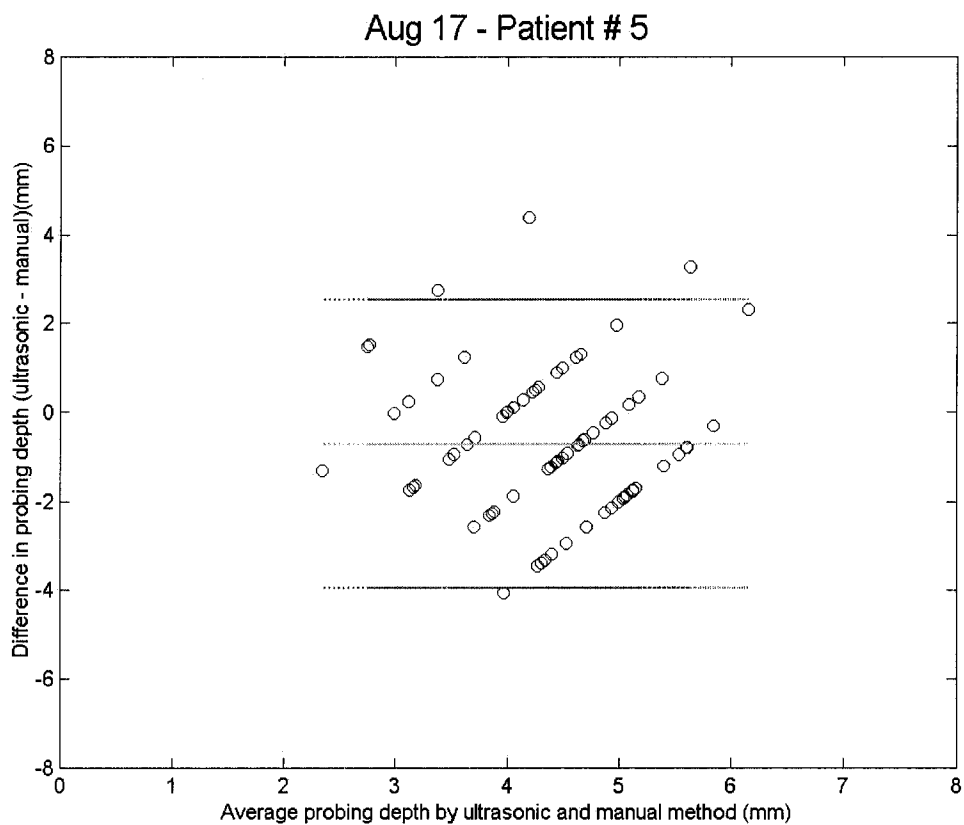


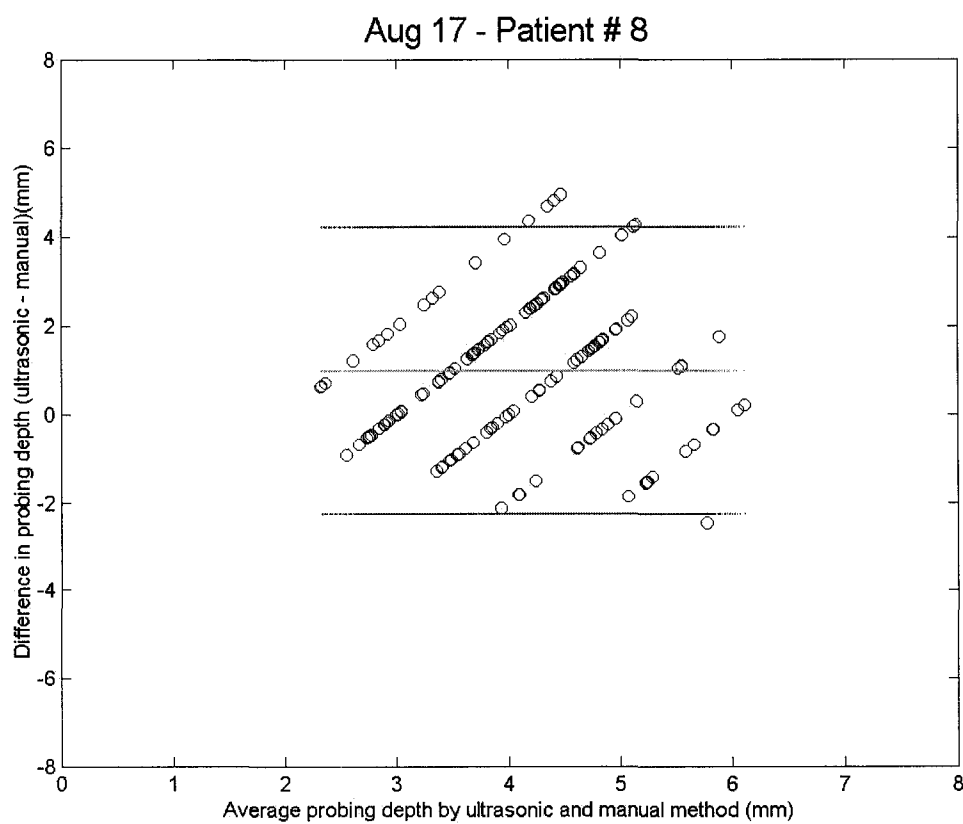
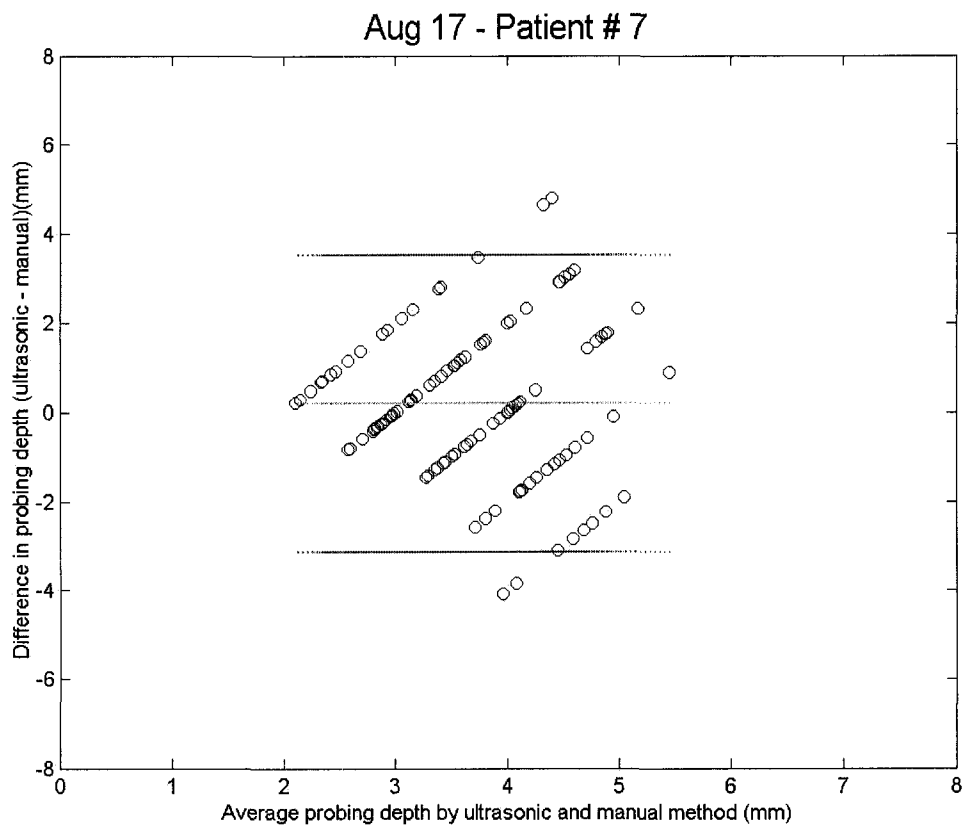
May 18 - Patient # 14

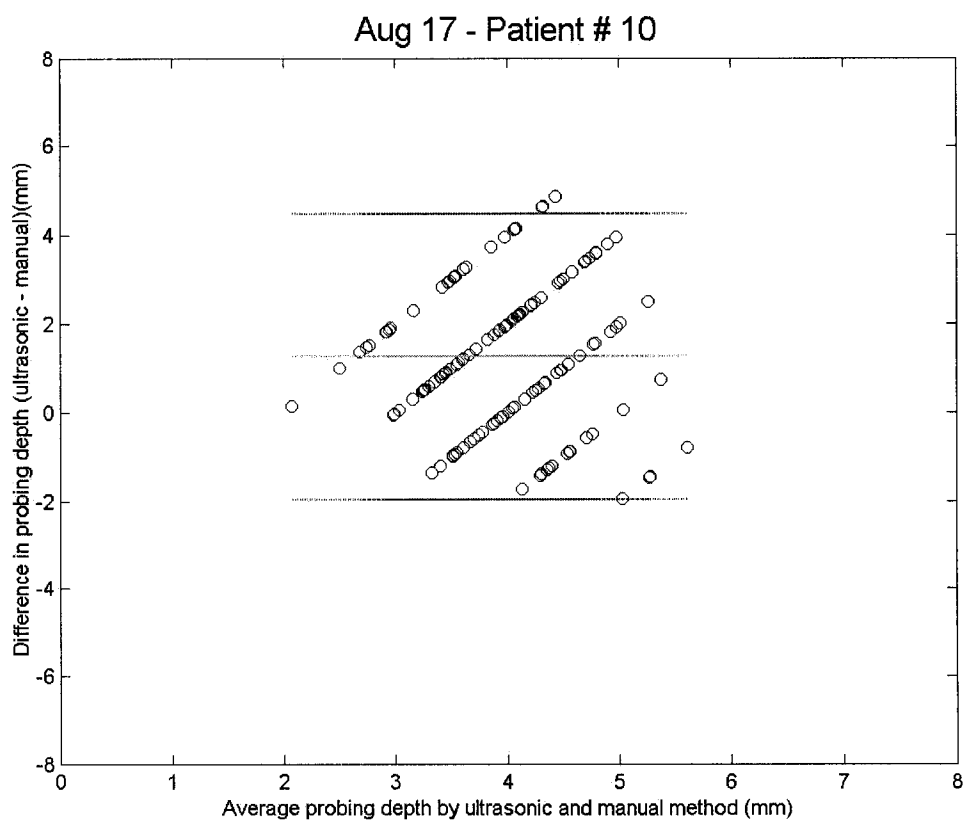
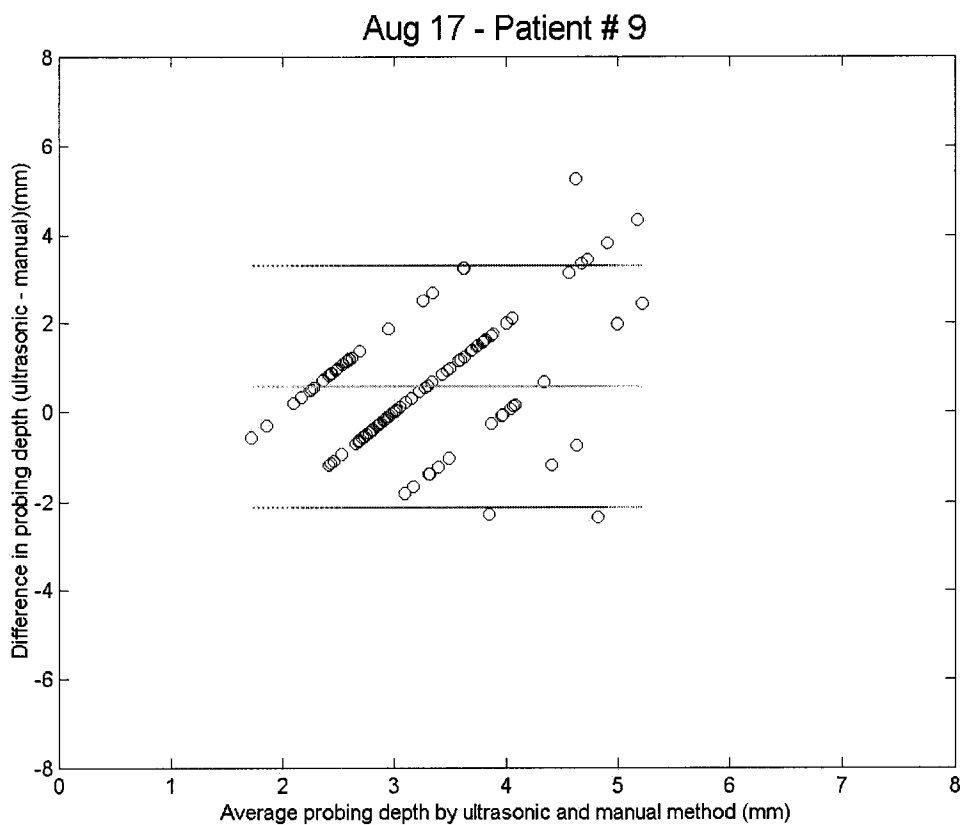


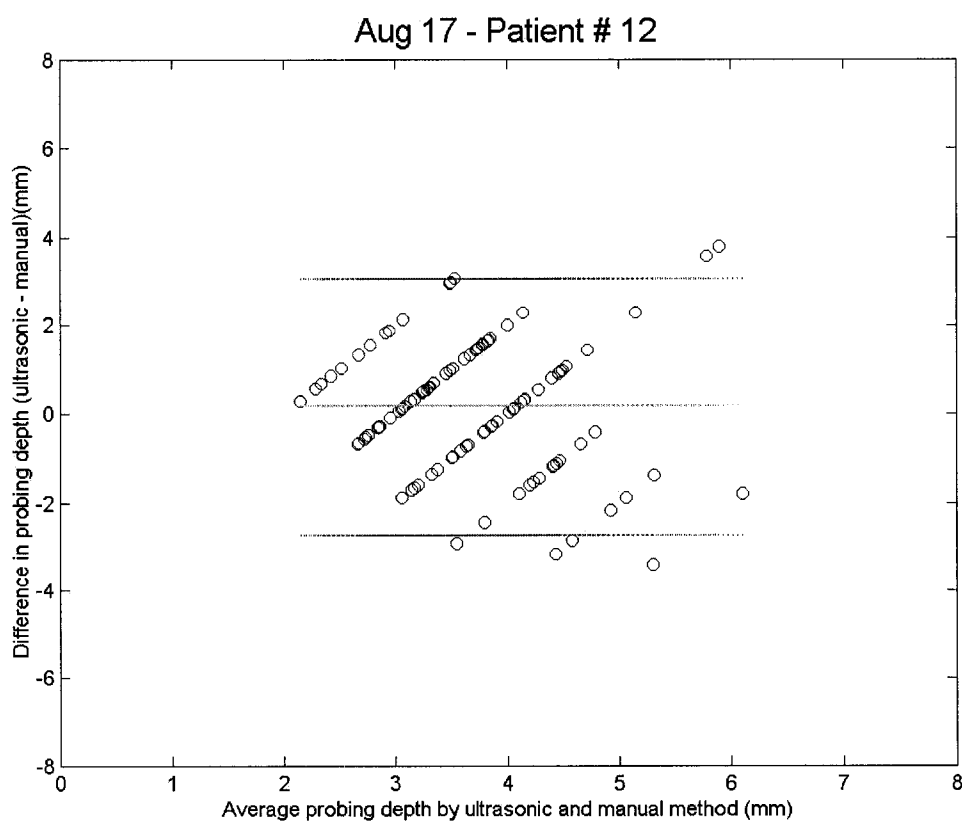
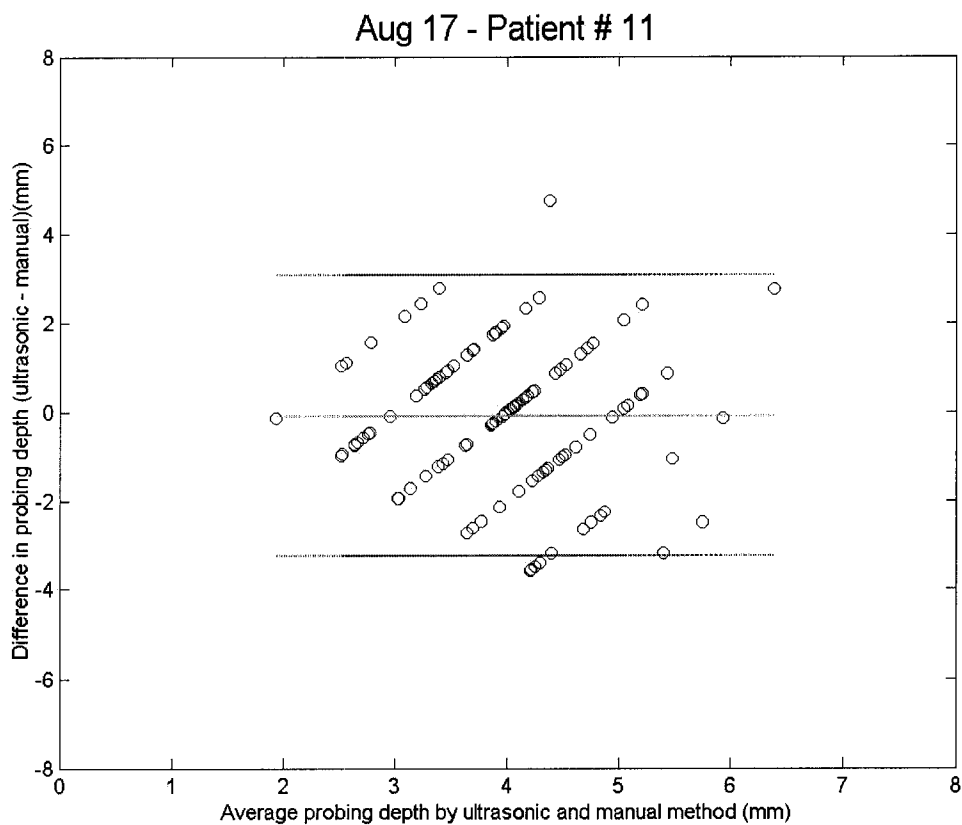


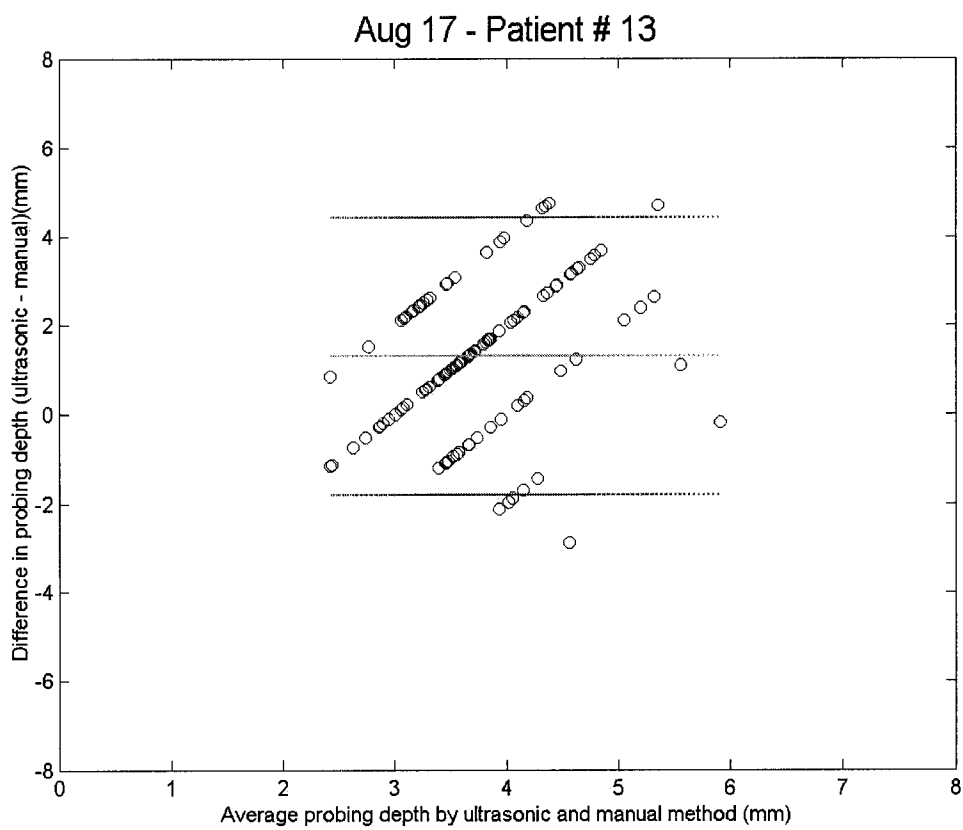












APPENDIX C

SOURCE CODE OF TOFS EXTRACTION OF MULTI LAMB MODES

```

clear
disp(' ');
disp(' ');
info= 'Welcome!';
disp(info);
disp(' ');
info= 'This program is developed to analyse Lamb waveforms and extract the TOFs of the first
three modes.';
disp(info);
disp(' ');

fna = input('Please enter data file name: ','s');
fname = ['d:\' fna];
disp('In Processing. Please wait... ');
disp(' ');

try,
    lsShow= 1;
    r = zeros(10000, 3);
    fid = fopen(fname, 'r');
    TOFs = zeros(1,20);
    %signal = fread(fid, 6500*15, 'int16');
    for m=1:1
        signal = fread(fid, 6500*1, 'int16');
        signal= signal- mean(signal);
        signal= [signal' zeros(1, 4000) ];
        signal= signal( 301: (2048+300) );

        if lsShow==1
            subplot(5,1,1);
            plot(signal);
            hold on
            xlim([1 length(signal) ]);
            xlabel('a','FontSize',14);
        end
        cfX = cwt(signal, 1:64, 'morl');
        cf2= mean(cfX.^2);
        [swa,swd] = swt(signal, 4, 'coif3');
        swd(1:3,:)=0;
        swa(:,:)=0;
        sx = iswt(swa,swd,'coif3');
        cfY = cwt(sx, 8:0.1:15, 'cgau2');
        [swa,swd] = swt(cf2, 6, 'coif3');
        swd(1:5,:)=0;

```

```

SER = iswt(swa,swd,'coif3');
if lsShow==1
    subplot(5,1,3);
    plot(cf2);
    xlim([1 length(cf2) ]);
    xlabel('(b)', 'FontSize',14);
end
if lsShow==1
    subplot(5,1,5);
    hold on
    plot(SER);
    xlim([1 length(SER) ]);
    xlabel('(c)', 'FontSize',14);
end
x_1=diff(SER);
yR_1 =[0 x_1];
yL_1 =[x_1 0];
big_1 = (yL_1>=0);
yL_1( big_1)= 5;
small_1 = (yL_1<0);
yL_1( small_1 )= 1;
big_1 = (yR_1>=0);
yR_1( big_1 )=1;
small_1 = (yR_1<0);
yR_1( small_1)=-5;
feng= find(yR_1 == yL_1);
feng= feng( feng>100 );
if lsShow==1
    plot(feng, SER(feng), 'ro');
end
thres_peak= 0.1* mean(SER);
feng = feng( SER(feng)> thres_peak );
fwidth = 10*2*2;
PeaksNumber= length(feng);
real_feng = feng;
for p=1:5
    local_region= cf2( feng(p) -fwidth: feng(p)+ fwidth);
    ppp= find( local_region == max( local_region) );
    real_feng(p) = feng(p)-fwidth + ppp - 1;
end
PeakFeature= zeros(PeaksNumber, 2);
if lsShow==1
    figure(2);
end
for dw =1:5
    if lsShow==1
        subplot(1,5, dw);
        end
        interface= real_feng(dw);
        if ( interface >fwidth )
            neighbor= cfY(:, interface- fwidth:interface+ fwidth);
            neighbor= abs(neighbor);
            top= max(max(neighbor) );
            if(top~=0)
                neighbor= neighbor/top;
            end
        end
    end
end

```

```

        tem=neighbor;
        tem(:,:)=0;
        x= find( neighbor>=0.9);
        tem(x)=1;
        dwfp=tem;
        PeakFeature(dw, 1) = sum(sum(dwfp));
        PeakFeature(dw, 2) = PeakFeature(dw, 1);
        if IsShow==1
            imshow(dwfp);
            title( [ num2str( PeakFeature(dw, 1) ) ] );
        end
    end
end
excel_data= [PeakFeature feng'];
GoodOnes= find(excel_data(:,1)>500);
if( length(GoodOnes) >= 3 )
    GoodModes= excel_data( GoodOnes, : );
    TOFs = GoodModes(:,3);
    clear GoodModes;
end
clear GoodOnes;

r(m, 1)= TOFs (1);
r(m, 2)= TOFs (2);
r(m, 3)= TOFs (3);
clear excel_data;

end

start_point= 1500;
sample_size= 6500;
sample_rate= 25;
delay_line= 12.1;
null_area =0;
r = (r + start_point+ null_area )/sample_rate - delay_line;
OUTname = [fna '.txt'];
save(OUTname, 'r','-ASCII')

fclose(fid);
disp('TOFs were saved in:');
disp(OUTname);
disp('Done!');

catch,
    estr = lasterr;
    disp(estr);
    disp('An error has occurred. Program ended');
    disp(' ');
end

```

APPENDIX D

ILLUSTRATIONS OF THE DWFP BASED ALGORITHM TO MEASURE THE ARRIVAL TIMES OF THE MULTIPLE LAMB WAVE MODES

In this appendix, additional processing results of the four aluminum plates in Chapter V are presented.

Plate # 15- 0.99 MHz -Projection 1

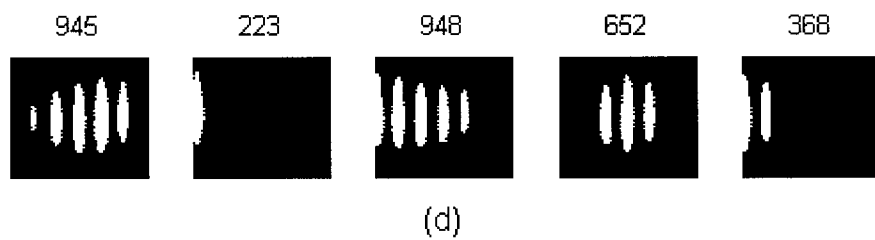
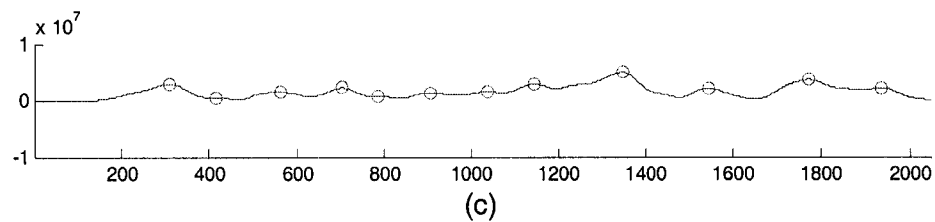
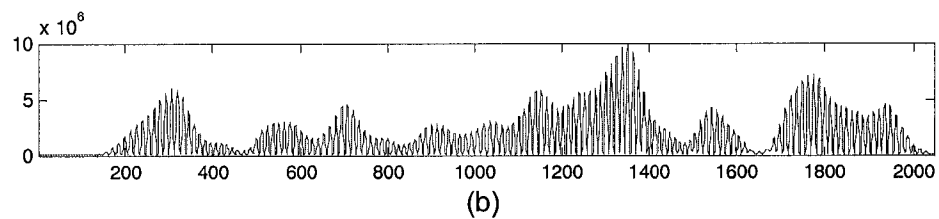
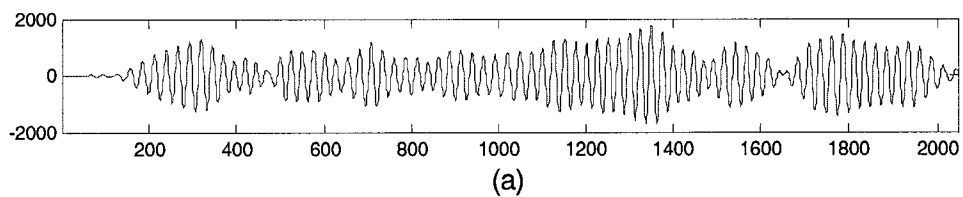


Plate # 15- 0.99 MHz -Projection 1

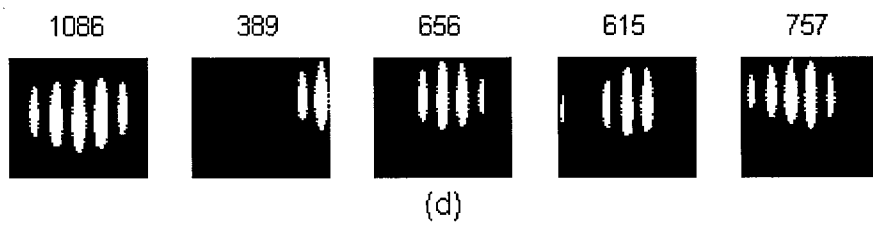
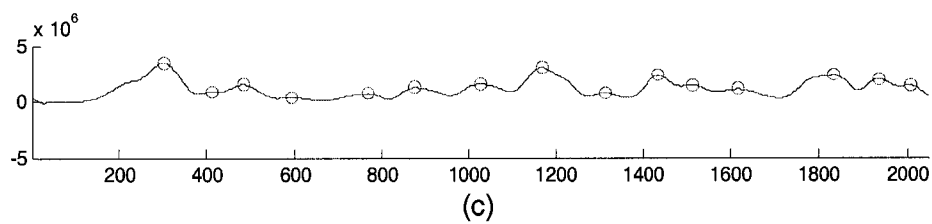
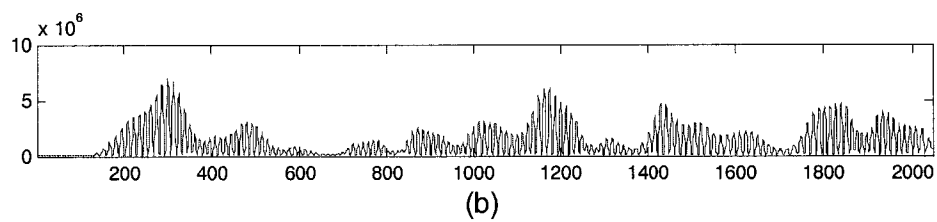
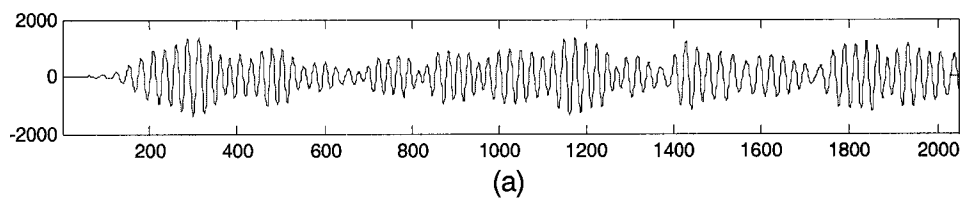


Plate # 1- 0.99 MHz -Projection 1

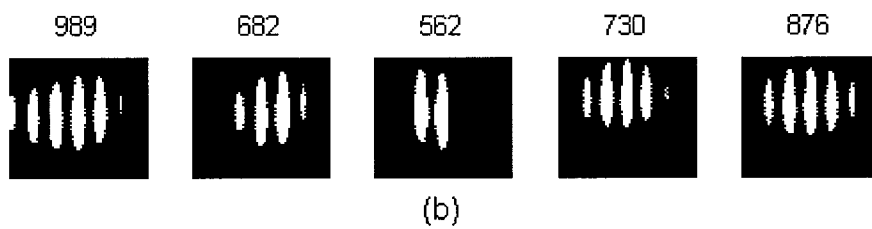
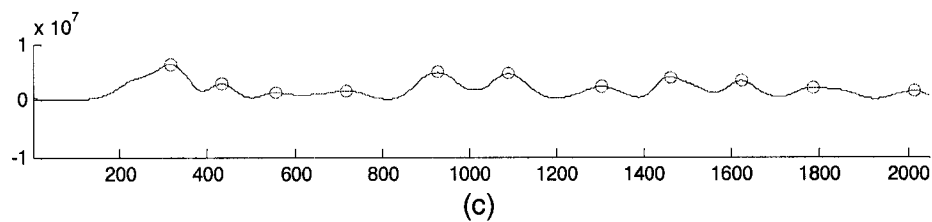
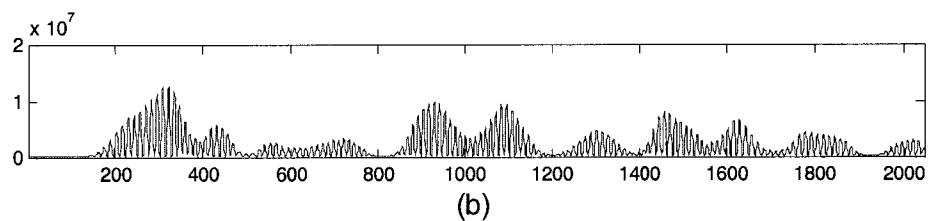
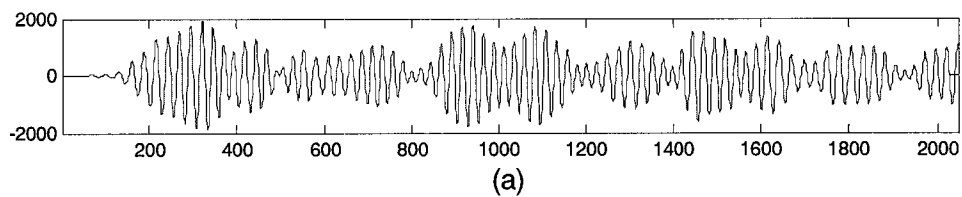


Plate # 1- 0.99 MHz -Projection 2

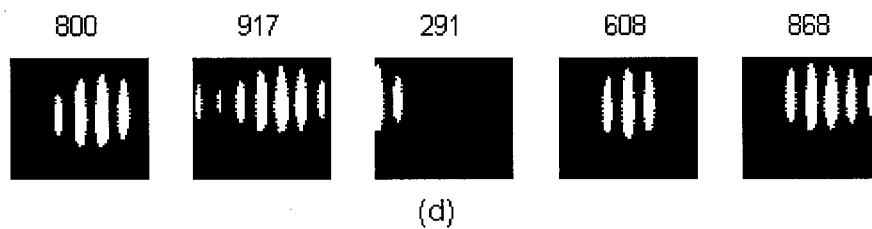
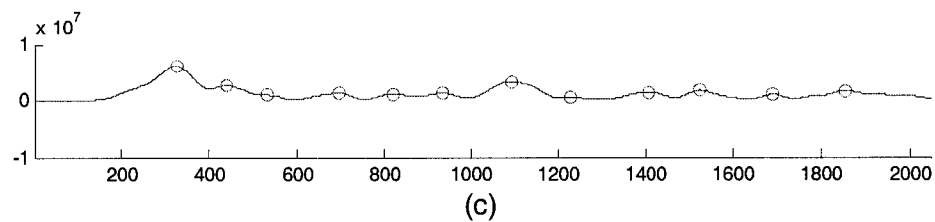
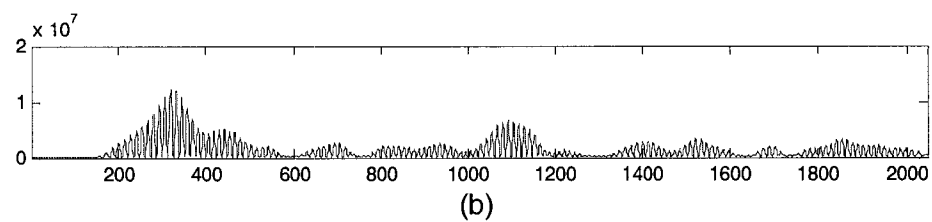
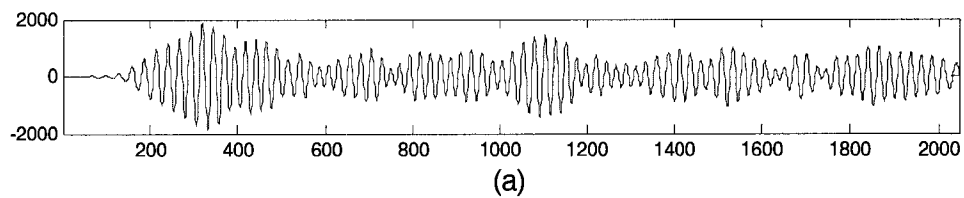


Plate # 5- 0.99 MHz -Projection 1

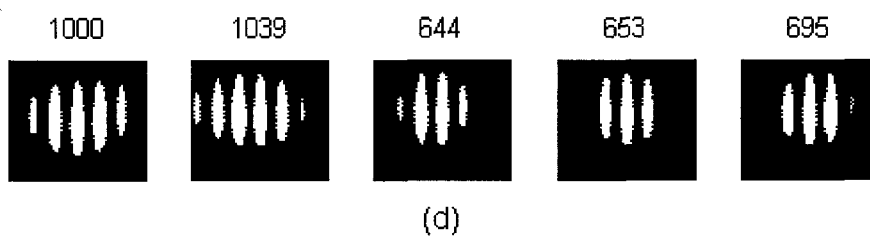
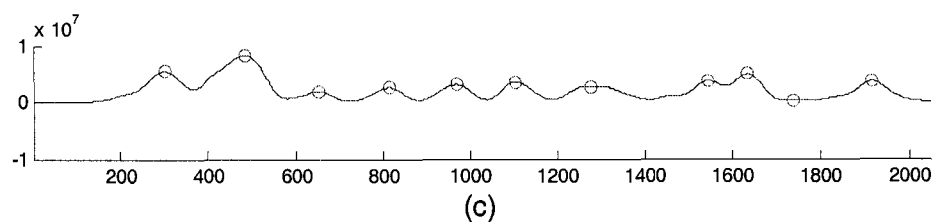
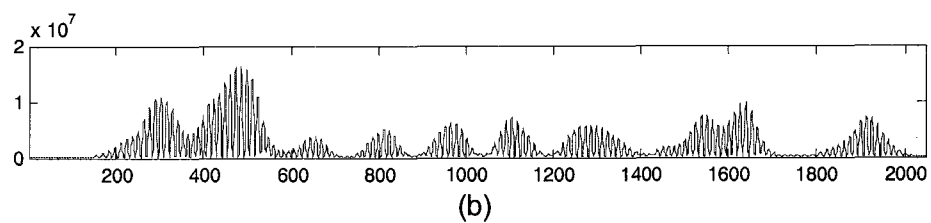
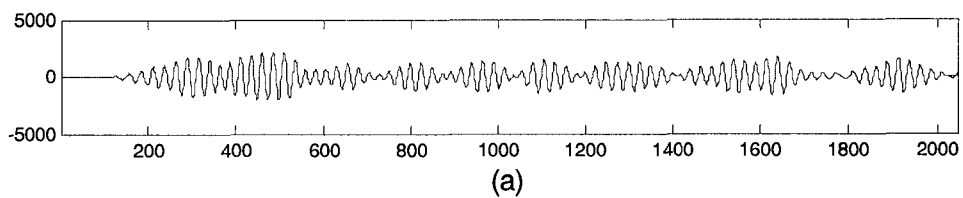


Plate # 5- 0.99 MHz -Projection 2

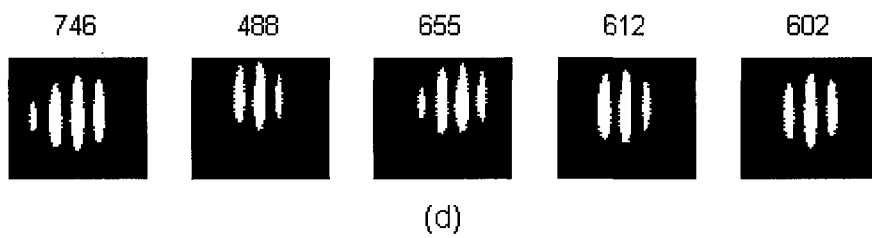
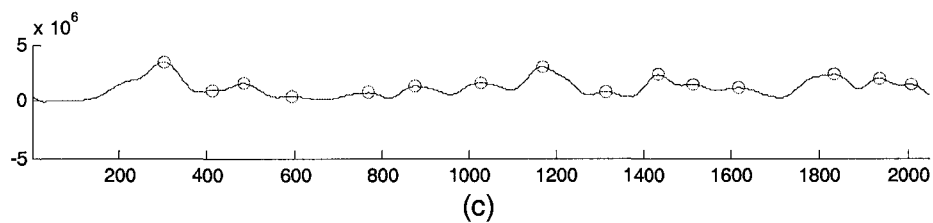
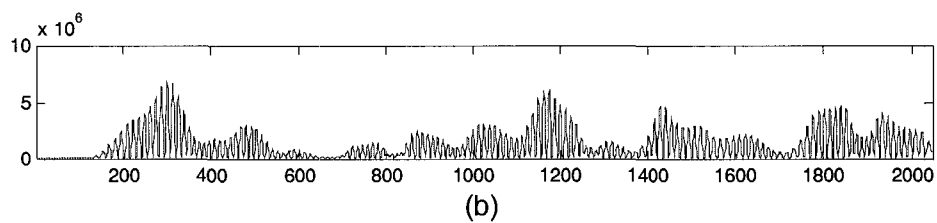
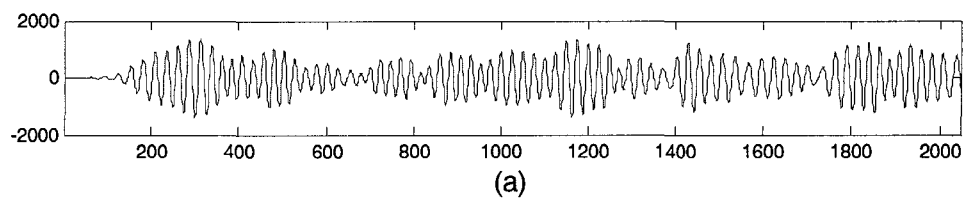


Plate # 6- 0.99 MHz -Projection 1

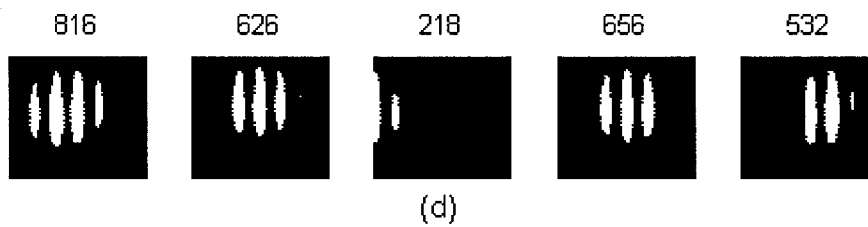
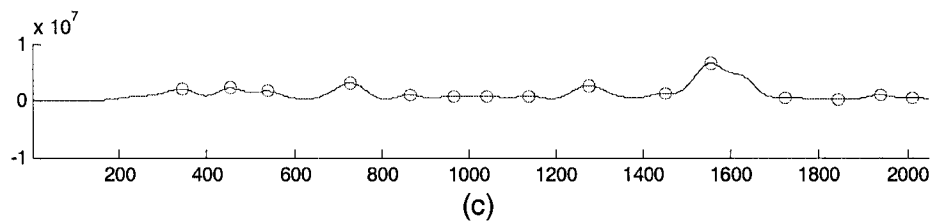
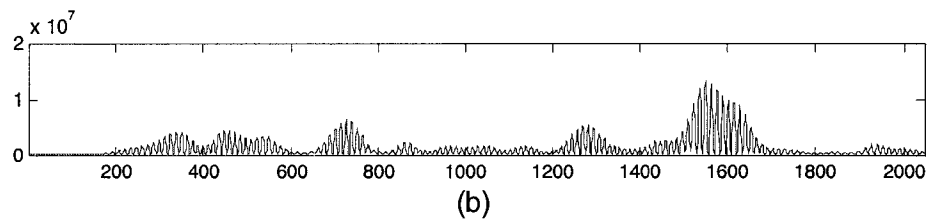
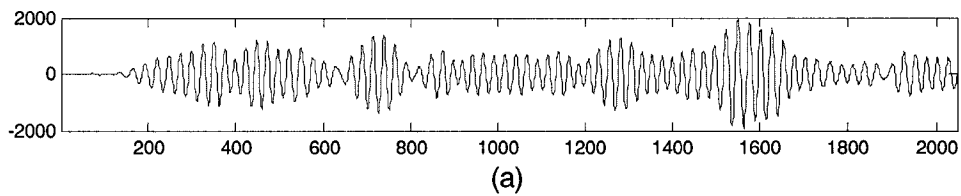
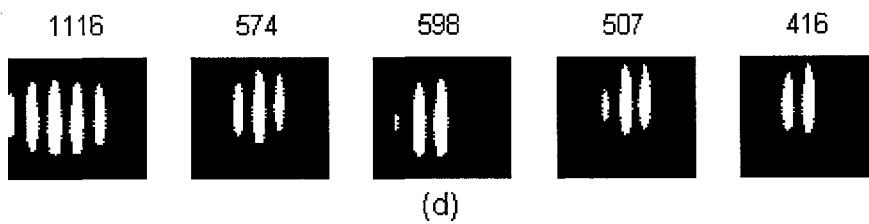
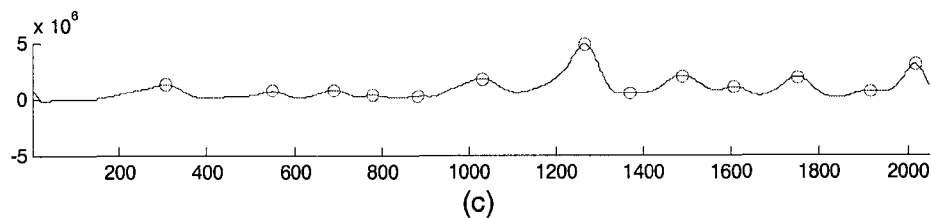
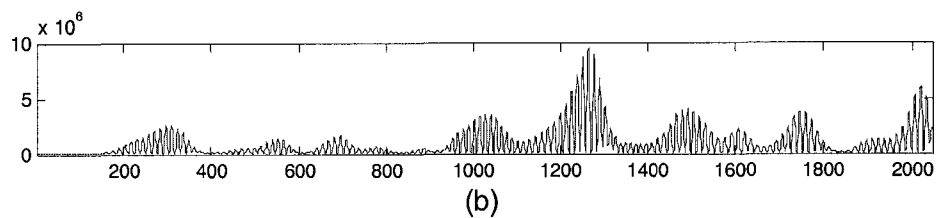
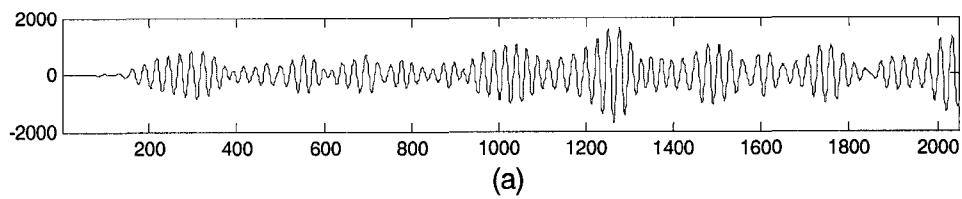


Plate # 6- 0.99 MHz -Projection 2



BIBLIOGRAPHY

- [1] G. Strang and T. Nguyen. *Wavelets and Filter Banks*. Wellesley-Cambridge Press, 1996.
- [2] A.A. Moenssens. *Fingerprint Technique*. Chilton Book Company, 1971.
- [3] *The Identification Division of the FBI*. Federal Bureau of Investigation. U.S. Department of Justice.
- [4] S.A. Cole. *Suspect Identities: A History of Fingerprinting and Criminal*. Harvard University Press, New York, 2001.
- [5] I. Daubechies. *Ten Lectures on Wavelets*. Society for Industrial and Applied Mathematics, Philadelphia, 1992.
- [6] D.R.Hull, H.E.Kautz and A. Vary. Measurement of ultrasonic velocity using phase-slope and cross-correlation methods. *Materials Evaluations*, 43:1455-1460, 1985.
- [7] L. Adler, A. Jungman, P. Nagy and J. Rose. Waveform and data analysis techniques, *Ultrasonic Testing, Nondestructive Testing Handbook*, 2nd edition. The American Society for Nondestructive Testing, 7:132-185, 1991.
- [8] P. Daponte, G. Fazio and A. Molinaro. Detection of echoes using time-frequency analysis techniques. *IEEE Transactions on Instrumentation and Measurement*, 45(1):30-39, 1996.
- [9] J.U. Quistgaard. Signal acquisition and processing in medical diagnostic ultrasound. *IEEE Signal Processing Magazine*, January, 67-74,1997.
- [10] R.E. Learned and A.S. Willsky. A wavelet packet approach to transient signal classification. *Applied and Computational Harmonic Analysis*, 2:265-278, 1995.
- [11] A. Abbate, J. Koay, J. Frankel, S.C. Schroeder and P. Das. Signal detection and noise suppression using a wavelet transform signal processor: application to ultrasonic flaw detection. *IEEE Transaction on Ultrasonics, Ferroelectrics, and Frequency Control* 44:14-26, 1997.
- [12] J.C. Goswami, A.K. Chan. *Fundamentals of Wavelets: Theory, Algorithms and Applications*. John Wiley & Sons, Inc., New York, 1999.

- [13] O. Rioul and Martin Vetterli. Wavelets and signal processing. *IEEE Signal Processing Magazine*, Oct., 14-38, 1991.
- [14] P. Abry, Ondelettes et turbulence. *Multirésolutions, algorithmes de décomposition, invariance d'échelles*, Diderot Editeur, Paris, 1997.
- [15] M. Misiti, Y. Misiti, G. Oppenheim, J. Poggi. *Wavelet Toolbox User's Guide*, version 2. The MathWorks, Inc., 2000.
- [16] A. Aldroubi, M. Unser. *Wavelets in Medicine and Biology*. CRC Press, Boca Raton, 1996.
- [17] Y. T. Chan. *Wavelet Basics*. Kluwer Academic Publishers, 1995.
- [18] G. Kaiser. *A Friendly Guide to Wavelets*. Birkhauser, Boston, 1994.
- [19] J. M. Speiser. Wide-band ambiguity functions. *IEEE Transactions on Information Theory*, 122-123, 1967.
- [20] L. Auslander and I. Gertner, Wide-band ambiguity function and $a.x+b$ group, *Signal Processing, Part I: Signal Processing Theory*, L.Auslander, T. Kailath, S.Mitter Eds. Institute for Mathematics and Its Applications, Spring Verlag, New York. 22:1-12, 1990.
- [21] X. Xu, A.H. Tewfik and J. Greenleaf. Time delay estimation using wavelet transform for pulse-wave ultrasound. *Annals of Biomedical Engineering*, 23:612-621, 1995.
- [22] S.E. Moubarik, D. Vadder and P. Benoist. Wavelets and non-destructive evaluation. *Review of Progress in Quantitative Nondestructive Evaluation*, D.O. Thompson and D. E. Chimenti, Eds. Plenum, New York, 1993.
- [23] D. L. Donoho. De-noising by soft thresholding. *IEEE Transactions on Information Theory*, 41(3):613-627, 1995.
- [24] R. Kronland-Martinet, J. Morlet and A. Grossman. Analysis of sound patterns through wavelet transforms. *Intl. J. Pattern Recognition and Artificial Intelligence*, 1(2): 273-302, 1987.
- [25] P. Ramuhalli, L. Udpa, S.S. Udpa. A signal classification network that computes its own reliability. *Review of Progress in Quantitative Nondestructive Evaluation*, D.O. Thompson and D.E. Chimenti, Eds. Plenum, New York.18: 857-864. 1999.
- [26] S. Legendre, D. Massicotte, J. Goyette, and T.K. Bose. Neural classification of lamb wave ultrasonic weld testing signals using wavelet coefficients. *IEEE Transactions on Instrumentation and Measurement*, 50: 672-678, 2001.
- [27] M. Kermit, and A. J. Eide. Audio signal identification via pattern capture and template matching. *Pattern Recognition Letters*, 21: 269-275, 2000,

- [28] M. Szczuka, P. Wojdylo. Neuro-wavelet classifiers for EEG signals based on rough set methods. *Neurocomputing*, 36: 103-122, 2001.
- [29] Z. Dokur and T. Olmez. ECG beat classification by a novel hybrid neural network. *Computer Methods and Programs in Biomedicine*, 66(2-3): 167-181, 2001.
- [30] V.P. Lunin and V.A. Barat. Crack angle and depth estimation using wavelet preprocessed neural network. *Review of Progress in Quantitative Nondestructive Evaluation*, D.O. Thompson and D.E. Chimenti, Eds. 18: 821-828, 1999.
- [31] V.P. Lunin, V.A. Barat, D. Podobedov. Neural network-based crack parameterization using wavelet preprocessing MFL signal. *Review of Progress in Quantitative Nondestructive Evaluation*, D.O. Thompson and D.E. Chimenti, Eds. 20:641-648, 2001.
- [32] R.R. Coifman and D.L. Donoho. Translation invariant de-noising. *Lecture Notes in Statistics*, 103:125-150, 1995.
- [33] G. Georgiou, and F.S. Cohen. Tissue characterization using the continuous wavelet transform. Part I: decomposition method. *IEEE Transactions on Ultrasonics, Ferroelectrics, and Frequency Control*, 48: 355-373, 2001.
- [34] M. Hu. Visual pattern recognition by moment invariants. *IRE Transactions on Information Theory*, IT-8: 179-187, 1962.
- [35] G.X. Ritter and J.N. Wilson. *Handbook of Computer Vision Algorithms in Image Algebra*, 2nd edition. CRC Press, Boca Raton, 2001.
- [36] E. Henneke, D. Chimenti and E. Papadakis. Fundamental principles of ultrasonic wave propagation. *Nondestructive Testing Handbook*, 2nd edition, American Society for Nondestructive Testing, Columbus, OH, 1991.
- [37] C.A. Evans, D.V. Leinman, W.R. Maas, et al. *Oral Health in America: A Report to the Surgeon General*. National Institute of Dental and Craniofacial Research. Bethesda, Maryland, 2000. (NIH publication No. 00-4713).
- [38] E.P. Barrington and M. Nevins. Diagnosing periodontal diseases. *J. Am. Dental Assoc.*, 121:460-464, 1990.
- [39] G.C. Armitage, et al. Diagnosis of Periodontal Diseases, Academy Report Position Paper. *J. Periodontol.* 74: 1237-1247, 2003.
- [40] E.B. Fowler. Periodontal disease and its association with systemic disease. *Military Medicine*, 166: 85-89, 2001.
- [41] D.W. Paquette. The periodontal infection-systemic disease link: a review of the truth or myth. *J. Int. Acad. of Periodontology*, 4: 101-109, 2002.

- [42] J. Slots. Update on general health risk of periodontal disease. *International Dental Journal*, 53: 200-207, 2003.
- [43] A.D. Haffajee, et al. Clinical parameters as predictors of destructive periodontal disease activity. *J. Clinical Periodontology*, 10:257, 1982.
- [44] J.F. Tessier, et al. Probing velocity: novel approach for assessment of inflamed periodontal attachment. *J. Periodontology*, 65: 103-108, 1994.
- [45] P.S. Hull, V. Clerehugh and A. Ghassemi-Aval. An assessment of the validity of a constant force electronic probe in measuring probing depths. *J. Periodontology*, 66: 848-851, 1995.
- [46] T.E. Rams and J. Slots. Comparison of two pressure-sensitive periodontal probes and a manual probe in shallow and deep pockets. *Int. J. of Periodontics & Restorative Dentistry*, 13: 521-529, 1993.
- [47] N.P. Lang and E.F. Corbet. Diagnostic procedures in daily practice. *Int. Dental J.* 45: 5-15, 1995.
- [48] G. Greenstein and I. Lamster. Understanding diagnostic testing for periodontal diseases. *J. Periodontology* 66:659-666, 1995.
- [49] M.A. Listgarten. Periodontal probing: What does it mean? *J. Clin Periodontology*. 7:165, 1980.
- [50] J.P. Trovato. The role of the general dentist in periodontal care. *General Dentistry*, 176-181, March-April, 2003.
- [51] L. Tupta-Veselicky, P. Famili, F.J. Ceravolo and T. Zullo. A clinical study of an electronic constant force periodontal probe. *J. Periodontology*, 65: 616-622, 1994.
- [52] M.E. Palou, M.J. McQuade and J.A. Rossman. The use of ultrasound for the determination of periodontal bone morphology. *J. Periodontology*, 58: 262-265, 1987.
- [53] F. Hunter. Periodontal probes and probing. *Int. Dental J.* 44:557-583, 1994.
- [54] L. Mayfield, G. Bratthall and R. Attstrom. Periodontal probe precision using 4 different periodontal probes. *J. Clin. Periodontology*, 23: 76-82, 1996.
- [55] M.K. Jeffcoat. Machines in periodontics. *Scientific*, 84: 18-22, 1991.
- [56] M. Quiryen, A. Callens, D.V. Steenberghe and M. Nys. Clinical evaluation of a constant force electronic probe. *J. Periodontology*, 64: 35-39, 1993.
- [57] M. Cattabriga, Future diagnostic possibilities in periodontology. *Int. Dental J.* 43: 109-115, 1993.

- [58] S.G. Grossl, R.G. Dunford, H.A. Koch, E.E. Machtei, R.J. Genco. Sources of error in periodontal probing measurements. *J. Periodontal Research*, 31: 330-336, 1996.
- [59] D.S. Barendregt, U. van der Velden, J. Relker and B.G. Loos. Clinical evaluation of tine shape of 3 periodontal probes using 2 probing forces. *J. Clin. Periodontology*, 23: 397-402, 1996.
- [60] J.J. Garnick and L. Silverstein. Periodontal probing: probe tip diameter. *J. Periodontology*, 71: 96-103, 2000.
- [61] S.F. Wang, et al. Reproducibility of periodontal probing using a conventional manual and an automated force-controlled electronic probe. *J. Periodontology*, 66: 38-46, 1995.
- [62] J.F. Tessier, et al. Relationship between periodontal probing velocity and gingival inflammation in human subjects. *J. Clin. Periodontology*, 20: 41-48, 1993.
- [63] L. Tupta-Veselicky, et al. A clinical study of an electronic constant force periodontal probe. *J. Periodontology*, 65: 616-622, 1994.
- [64] M. Cattabriga. Future diagnostic possibilities in periodontology. *Int. Dental J.* 43: 109-115, 1993.
- [65] M.C.K. Yang, et al. Reproducibility of an electronic probe in relative attachment level measurements. *J. Clin. Periodontology*, 19: 306-311, 1992.
- [66] N. Ahmed, T.L.P. Watts and R.F. Wilson. An investigation of the validity of attachment level measurements with an automated periodontal probe. *J. Clin. Periodontology*, 23: 452-455, 1996.
- [67] A. Agüero, et al. Histological location of a standardized periodontal probe in man. *J. Periodontology*, 66: 184-190, 1995.
- [68] J.G. Keagle, et al. Effect of gingival wall on resistance to probing forces. *J. Clin. Periodontology*, 22: 953-957, 1995.
- [69] H. Fukukita, et al. Development and application of an ultrasonic imaging system for dental diagnosis. *J. Clin. Ultrasound*, 13: 597-600, 1985.
- [70] C. Lost, K.M. Irion and W. Nussle. Periodontal ultrasonic diagnosis: experiments on thin bony platelets and on a simulated periodontal ligament space. *J. Periodontal Res.* 23: 347-351, 1988.
- [71] S.K. Ng, A. Songra, N. Ali and J.L.B. Carter. Ultrasound features of osteosarcoma of the mandible—a first report. *Oral Surgery Oral Medicine Pathology*, 92(5): 582-586 2001.

- [72] N. Hamano, K. Hanaoka, K. Ebihara, M. Toyada and T. Teranaka. Evaluation of adhesive defects using an ultrasonic pulse-reflection technique. *Dental Materials Journal*, 22 (1): 66-79, 2003.
- [73] S.R. Ghorayeb and T.Valle. Experimental evaluation of human teeth using noninvasive ultrasound: echodentography. *IEEE Transactions on Ultrasonics, Ferroelectrics, and Frequency Control*, 49: 1437-1443, 2002.
- [74] F.I. Tsiolis, I.G. Needleman and G.S. Griffiths. Periodontal ultrasonography. *J. Clinical Periodontology*, 30: 849-854, 2003.
- [75] A.C. Lassal and P.A. Payne, Scanning and imaging using lamb waves. *Acoustical Imaging*, 23: 355-361, 1997.
- [76] J.A. Companion, Differential measurement periodontal structures mapping system, US Patent #5,755,571, 1998.
- [77] D.R. Loker and K. Hagenbuch. Ultrasonic periodontal diagnostic instrumentation system with clinical results. *Measurement*, 23: 125-129, 1998.
- [78] M.K. Hinders and J. Companion. Ultrasonic periodontal probe, *Review of Progress in Quantitative Nondestructive Evaluation*, D.E. Chimenti and D.O. Thompson, Eds, Kluwer Academic/Plenum Publishers, 18: 1609-1615, 1999.
- [79] J.E Lynch. Development and clinical testing of an ultrasonographic periodontal probe. Dissertation. College of William and Mary, Williamsburg, Virginia, 2001.
- [80] M.K Hinders, J.E. Lynch and G. McCombs. Periodontal Disease Diagnosis using an Ultrasonic Probe. *Review of Progress in Quantitative Nondestructive Evaluation*, D.O. Thompson and D.E. Chimenti, Eds, American Institute of Physics, 21: 1880-1887, 2002.
- [81] J.E. Lynch and M.K. Hinders. Ultrasonic device for measuring periodontal attachment levels. *Review of Scientific Instruments*, 73(7): 2686-2693, 2002.
- [82] J. Rosiene and H. Sholl. Application of wavelets to ultrasonic evaluation of thickness. *SPIE Wavelet Applications*, 2242: 488-498, 1994.
- [83] A. Abbate, J. Koay, J. Frankel, S.C. Schroeder and P. Das. Application of wavelet transform signal processor to ultrasound. *IEEE Ultrasonic Symposium Proceedings*, 1147-1152, 1994.
- [84] R.N. Strickland and H. Hahn. Wavelet transforms for detecting microcalcifications in mammograms. *IEEE Transactions on Medical Imaging*, 15: 218-229, 1996.
- [85] X.L. Xu and J. F. Greenleaf. Wavelet transform for cross correlation processing in PW ultrasound. *Proceedings of the 16th Annual International Conference of the IEEE Engineering in Medicine and Biology Society*, 1224-1225, 1994.

- [86] M. Lemistre and D. Balageas. Structural health monitoring system based on diffracted Lamb wave analysis by multi-resolution procession. *Smart Materials and Structures*, 10: 504-511, 2001.
- [87] J. D. Hou and M.K. Hinders. Dynamic wavelet fingerprint identification of ultrasound signals. *Materials Evaluation*, 60: 1089-1093, 2002.
- [88] J.M. Bland and D.G. Altman. Statistical methods for assessing agreement between two methods of clinical measurement. *Lancet*, 8476:307-310, 1986.
- [89] K. R. Leonard, E. V. Malyarenko and M.K. Hinders. Ultrasonic Lamb wave tomography. *Inverse Problems*, 18: 1975-1808, 2002.
- [90] F.E. Ernst and G. C. Herman. Tomography of dispersive media. *Journal of Acoust. Soc. Am.*, 108(1), 2000.
- [91] J.C.P. McKeon. Tomography applied to Lamb wave contact scanning. Doctoral Dissertation, College of William and Mary, 1998.
- [92] M.K. Hinders, E.V. Malyarenko and J.C.P. McKeon. Contact scanning Lamb wave tomography. *J. Acoust. Soc. Am.*, 104 1790(A), 1998.
- [93] J.C.P. McKeon and M. K. Hinders. Parallel projection and crosshole contact scanning Lamb wave tomography. *J. Acoust. Soc. Am.*, 106:2568-2577, 1999.
- [94] E.V. Malyarenko and M.K. Hinders. Ultrasonic Lamb wave diffraction tomography. *Ultrasonics*, 39: 269-281, 2001.
- [95] E.V. Malyarenko. Lamb wave diffraction tomography. Doctoral Dissertation. College of William and Mary, 2000.
- [96] J. D. Achenbach. *Wave Propagation in Elastic Solids*, North-Holland, Netherlands, 1984.
- [97] B. A. Auld. *Acoustic Fields and Waves in Solids*. Kreiger, Malabar, FL, 1990.
- [98] A.C. Kak and M. Slaney. *Principles of Computerized Tomographic Imaging*. IEEE Inc. New York, 1988.
- [99] K.R. Leonard, Neural Network Technology and Lamb Wave Tomography. BS Thesis. College of William and Mary, 1999.
- [100] P. Wilcox, M. Lowe and P. Cawley. The effect of dispersion on long-range inspection using ultrasonic guided waves. *NDT&E International*, 34: 1-9, 2001.
- [101] J. L. Rose. *Ultrasonic Waves in Solid Media*. Cambridge University Press, Cambridge, UK, 1999.

- [102] M.K. Hinders, K.R. Leonard and E.V. Malyarenko. Blind test of Lamb wave diffraction tomography, *Review of Quantitative Nondestructive Evaluation*, D.O. Thompson and D.E.Chimenti, Eds. 21: 278-283, 2002.
- [103] N. Nulman, G. Mozarkewich, B. Khaykin. Ultrasonic thickness gauge for multi-layer plastic fuel tanks. *Proceedings of ANTEC'99*, 1017-1019, 1999.
- [104] T. Adams. Inspect plastic IC packages with ultrasound. *Semiconductor Int.*, 13(9): 88-91, 1990.
- [105] G. De Liso, M. Muschitiello, M. Stucchi. Failure analysis of encapsulated electronic devices by means of scanning ultrasonic microscopy technique. *Scanning* 15(4): 236-242, 1993.
- [106] T. Moore. The role of acoustic microscopy in the development of surface mount IC packaging. *Proceedings of ISTFA-96*, Los Angeles, 1996.
- [107] A. Abbate, N. Nguyen, S. LaBreck, T. Nelligan. Ultrasonic signal processing algorithms for the characterization of thin multilayers. *NDT.net*, 7(10), October 2002.
- [108] G. Betta and P. Daponte. Detection of echoes in noisy environments for multilayer structure characterization. *IEEE Trans. on Instrument and Measurement*. 42(4): 834-841, 1993.
- [109] L. Bechou, L. Angrisani, Y. Ousten, et al. Localization of defects in die-attach assembly by continuous wavelet transform using scanning acoustic microscopy. *Microelectronics Reliability*, 39:1095-1101, 1999.
- [110] L. Angrisani, L. Bechou, D. Dallet, et al. Detection and location of defects in electronic devices by means of scanning ultrasonic microscopy and the wavelet transform, *Measurement*, 31:77-91, 2002.
- [111] R. Croce, P. Calmon and L. Paradis. Modeling of propagation and echo formation in a multilayered structure. *Ultrasonics*, 38:537-541, 2000.
- [112] L.W. Schmerr, Jr. *Fundamentals of Ultrasonic Nondestructive Evaluation. A Modeling Approach*. Plenum Press, NY, 1998.
- [113] R. Demirli and J. Saniie. Model based time-frequency estimation of ultrasonic echoes for NDE applications, *2000 IEEE Ultrasonics Symposium*, 785-788, 2000.
- [114] R. Demirli and J. Saniie. Model based estimation of ultrasonic echoes. Part I: Analysis and algorithms. *IEEE Trans. Ultras. Ferroel. Freq. Control*, 48(3):787-811, 2001.
- [115] J.A. Fessler and A.O. Hero. Space alternating generalized expectation maximization algorithm. *IEEE Transactions on Signal Processing*, 42:2664-2667, 1994.

[116] C.G. Guetbi, D. Kouame, A. Ouahabi, and J.P. Chemla. Methods based on wavelets for time delay estimation of ultrasound signals. *IEEE International Conference on Electronics, Circuits and Systems*, Lisboa, Portugal, 3:113-116, 1998.

VITA

Jidong Hou

Jidong (James) Hou was born in ZhengZhou, China, on January 8, 1970. He received a B.S. degree in mechanical engineering from the Institute of Armored Vehicle Engineering, Beijing, China, in 1991, a M.S. degree in materials engineering/applied chemistry from the National University of Defense Technology, Changsha, China, in 1994. In September 1999, he entered the College of William and Mary to be a graduate assistant in the Department of Applied Science. He then received a M.S. degree in non-destructive evaluation from the College of William and Mary in 2002. While pursuing his doctoral degree, he has been working as an applications engineer at Sonix, Inc., Virginia since September 2002. His research interest include ultrasonic signal processing and imaging. Currently he lives in Fairfax, Virginia, with his wife Shu Lan and his son William.